

COMPUTER SIMULATIONS OF COMPLEX FLUIDS IN TWO DIMENSIONS

vorgelegt von

Diplomphysiker
Heiko Schmidle
Memmingen

Von der Fakultät II - Mathematik und Naturwissenschaften
der Technischen Universität Berlin
zur Erlangung des akademischen Grades
Doktor der Naturwissenschaften
Dr. rer. nat.

genehmigte Dissertation

Promotionsausschuss:

Vorsitzende: Prof. Dr. Janina Maultzsch
Berichterin: Prof. Dr. Sabine H. L. Klapp
Berichterin: Prof. Carol K. Hall, PhD

Tag der wissenschaftlichen Aussprache: 17.04.2012

Berlin, 2012
D83

ABSTRACT

In this work we use computer simulations to study the phase behavior of various colloidal systems with dipolar interactions confined to two dimensions. First, we study condensation phase transitions of two-dimensional Stockmayer fluids under additional external fields using two state-of-the-art techniques based on Grand-canonical Monte-Carlo simulations, namely Wang-Landau and Successive Umbrella sampling. Considering systems in zero field, we demonstrate that the two techniques yield consistent results, but display pronounced differences in terms of efficiency. In the presence of homogeneous external fields the Successive Umbrella method becomes plagued by pronounced sampling difficulties, yielding the calculation of coexistence lines essentially impossible. Employing the Wang Landau scheme we find phase coexistence even for strongly field-aligned systems. The corresponding critical temperatures are significantly shifted relative to the zero-field case. In addition, we determine the condensation phase transition of dipolar Soft-Spheres exposed to a rotating external field.

Following, we investigate a phase diagram of two-dimensional particles with dipole-like short-ranged interactions based on Discontinuous Molecular Dynamics simulations. Similar to systems with true dipolar interactions the present system undergoes a transition from an isotropic fluid phase into a polymer-like fluid. Further decrease of the temperature leads to a percolated system which, moreover, displays dynamical properties reminiscent of a gel. Specifically, we find a plateau in the mean-squared displacement and a non-gaussian behavior of the self-part of the van-Hove correlation function. In the high density region we observe crystallization from the isotropic fluid into a solid phase with hexagonal order. Surprisingly, the crystallization is accompanied by a global parallel ordering of the dipole moments, i. e., a ferroelectric phase.

Finally, we investigate the aggregation patterns and dynamics of model colloidal mixtures consisting of particles with either one or two, oppositely oriented, induced dipole moments, based mainly on Monte-Carlo simulations. Our model is inspired by recent optical-microscopy experiments involving polystyrene particles with (and without) gold patches. For a broad range of parameters, we find the model systems to self-assemble via a two-step scenario involving first percolation along the field, followed by a percolation transition in the parallel direction. The resulting two-dimensional networks are characterized by strongly hindered translational dynamics.

ZUSAMMENFASSUNG

In dieser Arbeit benutzen wir Computersimulationen, um das Phasenverhalten von verschiedenen zweidimensionalen Kolloidsystemen mit Dipolwechselwirkung zu untersuchen. Wir beginnen damit Kondensationsphasenübergänge von Stockmayer Teilchen unter dem Einfluß von zusätzlichen äußeren Feldern zu untersuchen. Wir nutzen zwei "state-of-the-art" Methoden, die auf Großkanonischen Monte-Carlo Simulationen basieren, Wang-Landau und Successive Umbrella Sampling. Wir zeigen in Systemen ohne Feld, dass beide Methoden zu konsistenten Resultaten führen, jedoch deutliche Unterschiede in der Effizienz aufzeigen. In Anwesenheit eines homogenen äußeren Feldes zeigt Successive Umbrella Sampling deutliche Schwierigkeiten die Kondensation zu bestimmen. Mit Wang-Landau Sampling dagegen, sind wir in der Lage die Koexistenz zu bestimmen, sogar für Systeme, die stark von dem Feld beeinflusst werden. Die kritischen Temperaturen werden im Vergleich zum System ohne Feld deutlich verschoben. Zusätzlich bestimmen wir die Kondensation eines Systems aus dipolaren weichen Kugeln, die einem rotierenden Feld ausgesetzt werden.

Darüberhinaus erkunden wir das Phasendiagramm von zweidimensionalen Teilchen, die ein kurzreichweitiges Potential, ähnlich dem Dipolepotential, besitzen. Das System vollzieht einen Übergang von einer isotropen in eine polymerisierte Flüssigkeit. Weiteres Absenken der Temperatur führt zu einer perkolierten Phase, die außerdem dynamische Eigenschaften eines Gels aufzeigt. Im Einzelnen finden wir ein Plateau im Mean-Square-Displacement und eine Abweichung vom gaussischen Verhalten des Selbstanteils der van-Hove Funktion. Im Bereich hoher Dichten beobachten wir die Kristallisation von einer isotropen Flüssigkeit in eine geordnete feste Phase mit hexagonaler Ordnung. Überraschenderweise ist die Kristallisation von einer globalen parallelen Ordnung der Dipole begleitet, d.h. wir finden eine ferroelektrische Phase.

Zuletzt untersuchen wir die Dynamik und Strukturen der Aggregation einer Mischung eines kolloiden Modellsystems, bestehend aus Teilchen mit einem oder zwei entgegengesetzt ausgerichteten induzierten Dipolmomenten, hauptsächlich auf Monte-Carlo Simulationen basierend. Unser Modell ist von aktuellen Experimenten mit Polystyren-Teilchen mit und ohne Gold-Patch inspiriert. In einem großen Parameterbereich assembliert das Modellsystem in zwei Schritten. Zuerst perkoliert es in Feld Richtung, um dann einen Perkoliationsübergang parallel zum Feld zu vollziehen. Die resultierenden zweidimensionalen Netzwerke zeigen Charakteristiken einer stark gedämpften Dynamik.

PUBLICATIONS

The main ideas and figures of this work have appeared previously in the following publications:

The following are publications with principal contribution:

- “Phase transitions of two-dimensional dipolar fluids in external fields”, Heiko Schmidle and Sabine H. L. Klapp, *J. Chem. Phys.* 134, 114903 (2011).
- “Phase diagram of two-dimensional systems of dipole-like colloids”, Heiko Schmidle , Carol K. Hall , Orlin D. Velev, and Sabine H. L. Klapp, *Soft Matter*, 8, 1521-1531 (2012).
- “Two-dimensional colloidal networks induced by a uni-axial external field”, Heiko Schmidle, Sebastian Jäger, Carol K. Hall, Orlin D. Velev, and Sabine H. L. Klapp, submitted to *Phys. Rev. Lett.*, (2012).

The following is a publication with a partly contribution:

- “Non-equilibrium condensation and coarsening of field-driven dipolar colloids”, Sebastian Jäger, Heiko Schmidle, and Sabine H. L. Klapp, submitted to *Euro. Phys. Lett.*, (2012).

*This work is dedicated to my loving family,
as their endless support made it possible for me
to pursue my scientific curiosity.*

ACKNOWLEDGMENTS

I am deeply indebted to my supervisor Prof. Sabine H. L. Klapp, who introduced me to the fascinating field of complex fluids, dipolar systems and computer simulations. Her great mentoring during the past three years enabled me to complete this thesis successfully. I am very grateful to Prof. Carol K. Hall, who accommodated me very hearty in her group during my stay at the NCSU. She opened to me the extremely interesting field of Discontinuous Molecular Dynamics simulations.

I am very thankful to all the members of Prof. Sabine H. L. Klapp's and Prof. Carol K. Hall's group that assisted me with fruitful discussions and helpful explanations in preparing this thesis.

Finally, I acknowledge financial support from the Deutsche Forschungsgemeinschaft through the International Research Training Group 1524 "Self-Assembled Soft Matter Nano-Structures at Interfaces" (project C 3.1).

CONTENTS

1	INTRODUCTION	1
2	STATISTICAL MECHANICS AND COMPUTER SIMULATIONS	11
2.1	Particle models	11
2.1.1	Continuous model of quasi two-dimensional dipoles	11
2.1.2	Discontinuous model of two-dimensional dipoles	12
2.2	Ensembles	15
2.2.1	Canonical ensemble	15
2.2.2	Grand-canonical ensemble	16
2.2.3	Configurational integral	16
2.2.4	Ergodicity	17
2.3	Phase transitions	18
2.3.1	First-order phase transition	19
2.3.2	Continuous phase transition	20
2.3.3	Percolation	20
2.4	Computer simulations	23
2.4.1	Monte-Carlo simulations	23
2.4.2	Grand-canonical Monte-Carlo sampling	25
2.4.3	Chemical potential	26
2.4.4	Advanced Monte-Carlo techniques	27
2.4.5	Discontinuous Molecular Dynamics simulations	34
2.4.6	Further simulation techniques	38
2.4.7	Long-range interactions	39
2.5	Static properties of fluids	46
2.5.1	Fluctuations	46
2.5.2	Correlation functions	47
2.5.3	Structural properties	48
2.5.4	Clusters	50
2.6	Dynamic properties of fluids	50
2.6.1	Mean-Square-Displacement	50
2.6.2	Van-Hove function	52
3	PHASE TRANSITIONS OF TWO-DIMENSIONAL DIPOLAR FLUIDS AND INFLUENCE OF EXTERNAL FIELDS	53
3.1	System without external field	53
3.1.1	Weakly coupled systems	54
3.1.2	Binder cumulant	57
3.2	External field perpendicular to plane	62
3.3	External field in the plane	66
3.4	Rotating external field	68
3.5	Summary	70

4	PHASE DIAGRAM OF TWO-DIMENSIONAL SYSTEMS OF DIPOLE-LIKE COLLOIDS. A MOLECULAR DYNAMICS STUDY.	73
4.1	Fluid phases	73
4.1.1	Polymerization	73
4.1.2	Percolation and related dynamics	76
4.2	Ordered phases	81
4.2.1	Low densities	82
4.2.2	High densities	83
4.3	Summary	86
5	NETWORK FORMATION IN SYSTEM OF INDUCED DIPOLES IN TWO DIMENSIONS	91
5.1	Background	91
5.1.1	Experimental background	91
5.1.2	Model	94
5.2	One-component system	96
5.3	Mixtures of DID and ID	97
5.3.1	Percolation	98
5.3.2	Dynamics of the networks	101
5.4	Summary	104
6	CONCLUSION AND OUTLOOK	105
	BIBLIOGRAPHY	111

LIST OF FIGURES

Figure 1	Snapshots of experimental system with permanent magnetic dipoles	2
Figure 2	Snapshots of experimental system with permanent electric dipoles	3
Figure 3	Snapshots of experimental system with induced electric dipoles	4
Figure 4	Schematic representation of the model used in DMD	13
Figure 5	Comparison of interaction between true dipoles and the DMD model for various configurations	14
Figure 6	Gibbs Free Energy and the order parameter at a first-order and second order phase transition	19
Figure 7	Particle density and histogram during a GCMC simulation	28
Figure 8	Successive-Umbrella weight function for one example systems	30
Figure 9	Wang-Landau weight function for three iteration steps	32
Figure 10	Pair correlation function of a Lennard-Jones fluid	49
Figure 11	Vapor-liquid coexistence curve at $\sqrt{\mu^*} = 1$ obtained with SU and WL sampling compared to literature results	54
Figure 12	Vapor-liquid coexistence curve at $\mu^* = \sqrt{3}$ obtained with SU and WL sampling compared to literature results	55
Figure 13	Snapshot of the quasi two-dimensional Stockmayer fluid at $\mu^* = \sqrt{3}$ and $\mu^* = \sqrt{6}$	56
Figure 14	Snapshots of the weakly coupled system in the vapor, metastable, and liquid phase	57
Figure 15	The Binder cumulant for one system with $\mu^* = \sqrt{1}$	58
Figure 16	WL weight-function for different dipole couplings	61
Figure 17	Average dipole moment as function of an external field	63
Figure 18	Pair potential of Stockmayer particles aligned perpendicular to the plane	63
Figure 19	Phase diagram with an external field perpendicular to the plane	64
Figure 20	WL weight-functions after several iterations and various external fields	64

Figure 21	Snapshots of the weakly coupled Stockmayer particles exposed to a field perpendicular to the plane	65
Figure 22	In plane correlation function for different densities	66
Figure 23	Snapshots of various systems with external field in plane	67
Figure 24	Phase diagram at $\mu^* = \sqrt{3}$ and $B_{\parallel}^* = 5$	68
Figure 25	Snapshots of the medium coupled Stockmayer particles exposed to a field parallel to the plane	68
Figure 26	Phase diagram of dipolar Soft-Spheres at $\mu^* = \sqrt{9}$ and a rotating external field	70
Figure 27	Degree of polymerization at low and medium densities	74
Figure 28	Specific heat and cluster size distribution at low and medium densities	74
Figure 29	Phase diagram of DMD model at low and medium densities	76
Figure 30	Snapshot of the DMD model close to the percolation	77
Figure 31	Percolation probability at two different system sizes	77
Figure 32	MSD at different densities and temperatures	78
Figure 33	Self-part of the van Hove function and non-gaussian parameter	79
Figure 34	Snapshot in the percolated phase at low temperature	82
Figure 35	Snapshots illustrating the melting transition	84
Figure 36	Ψ_6 at different densities	84
Figure 37	Transition from isotropic fluid to ordered phase at $\rho^* = 0.9$	85
Figure 38	Two particle correlation function of the dipole orientation	87
Figure 39	Phase diagram of 2D dipole-like colloids	88
Figure 40	Sketch of the Clausius-Mossotti realtion	92
Figure 41	Interaction potential between two DID and between one ID and DID	93
Figure 42	Ground-state structures of 2-5 DID and one DID with 2-4 ID	94
Figure 43	Simulation snapshots of one-component system of ID and DID	96
Figure 44	Experimental snapshots compared to snapshots of our simulations	97
Figure 45	Percolation probability parallel and perpendicular to the external field	98

Figure 46	Pair correlation function parallel and perpendicular to the field	99
Figure 47	Snapshots of DID and ID mixtures at two different concentrations and densities	100
Figure 48	Percolation probability parallel and perpendicular to the field	101
Figure 49	MSD parallel and perpendicular to the field at two densities	102
Figure 50	Two-particle bond life time correlation	102

LIST OF TABLES

Table 1	Definition of reduced units for quasi two-dimensional Stockmayer particles	12
Table 2	Critical temperatures and critical densities at two dipole couplings and different system sizes without external field	58
Table 3	Coexisting vapor and liquid phase at $\mu^* = \sqrt{6}$.	59
Table 4	Critical parameters at $\mu^* = \sqrt{6}$.	60
Table 5	Estimated simulation times for different dipole couplings and system sizes.	61

ACRONYMS

MC	Monte-Carlo
MD	Molecular Dynamics
DMD	Discontinuous Molecular Dynamics
GC	Grand-canonical
GE	Gibbs Ensemble
DOS	Density of States
SU	Successive Umbrella
WL	Wang-Landau
HR	Histogram Reweighting

SS	Soft-Sphere
LJ	Lennard-Jones
HS	Hard-Sphere
MSD	Mean-Square-Displacement
DHS	Dipolar Hard-Spheres
DSS	Dipolar Soft-Spheres
SM	Stockmayer
BD	Brownian Dynamics

INTRODUCTION

Fluids containing polarizable or permanently dipolar particles on the nano- or micron scale play an important role in the synthesis of new advanced materials [112, 53] and related applications, such as electrical circuits, sensors [174], and molecular miniature devices. There is an increasingly strong interest in designing targeted micron- and nano-structures with tunable physical and mechanical properties [120]. In order to create, e. g., sophisticated optical, electronic and biosensing devices the bottom-up approach through the self-assembly of micron- or nano-size particles is of crucial importance [174]. The self-assembly and phase behavior of colloidal particles with such anisotropic interactions that emerge, e. g., from permanent or induced dipolar interactions is a rapidly expanding research field of high relevance [129, 53].

Also more complex anisotropic particles are applicable to produce sophisticated structures [201]. Examples are particles that possess quadrupolar interactions and assemble into two-dimensional sheets and three-dimensional tubes [172] or patchy particles that form networks and chains [159]. The shape of the particles plays also a crucial role in creating, e. g., branched networks from H-shaped particles [128]. In this work, however, we focus on particles with dipolar or dipole-like interactions. Indeed, materials of particles with induced or permanent dipole-dipole interactions offer several advantages such as tunable (directional) interactions and controllability of the structural, dynamical and phase behavior via an external, electric or magnetic field. One such controllable quantity is percolation, which is an important ingredient in controlling the physical and mechanical properties of nano-structures [107]. Recent experiments showed that e.g. the thermal conductivity [131] as well as the electrical conductivity [157] can be controlled via the directed assembly. Additional effects that can be controlled through external fields are, e. g., induced phase transitions in 3D dipolar systems [198, 72], enhancement of the layer formation in confined system of dipoles [86] or manipulation and separation of bioparticles [141]. Understanding the complex, self-assembled structures formed by such anisotropic particles [31] and the manipulation of these structures by external fields (and other factors such as chemical composition and thermodynamic parameters) is important e. g.,

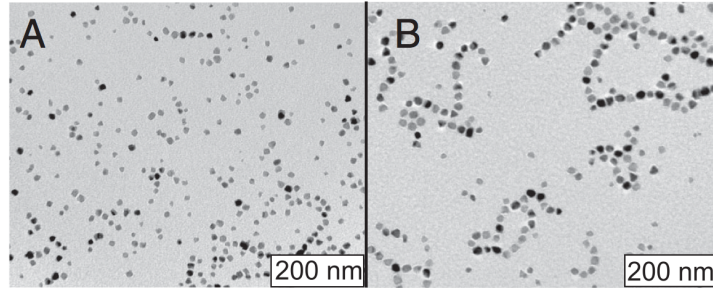


Figure 1: Experimental snapshot recorded with TEM and different dipolar couplings. In A the coupling is $\lambda \approx 4k_B T$ and in B the coupling is $\lambda \approx 9k_B T$. The surface fraction of both systems is 0.14. [Image taken from [93]]

for the development of new, "smart" or "stimuli-responsive", materials [53], and also for the advancement of devices such as sensors and nano-robots [112, 19, 15].

"Classical" realizations of such systems are (para- or ferro)magnetic nano-particles with and without magnetic fields, as well as polarizable colloids in electric fields. Examples of nano-particles with permanent magnetic dipole moment are magnetite (Fe_3O_4) [93] and maghemite ($\gamma\text{-Fe}_2\text{O}_3$) [110]. Magnetite particles are of the size of $r \approx 20 - 25\text{nm}$ and interact with a dipolar coupling strength of $\lambda \approx 4 - 9k_B T$, where λ describes the dipolar interaction compared to the thermal energy at a given temperature. To illustrate their self-assembly we show an experimental snapshot of such a two-dimensional system in Figure 1, where in (A) the dipolar coupling is $\lambda \approx 4k_B T$ and in (B) the coupling is $\lambda \approx 9k_B T$ (the surface fraction of both systems is 0.14) [93]. The nano-particles show the typical behavior of chain and ring formation in two dimensions emerging from the favored head-to-tail configuration. Maghemite nano-particles are smaller, $r \approx 5.5\text{nm}$, and have a weaker coupling strength, $\lambda \approx 1.4k_B T$, compared to magnetite. However, both systems, magnetite and maghemite, display a pronounced response when they are exposed to external magnetic fields. Long chains and columns of zipped chains are observed that have a strong impact on the dynamic properties of the system [110]. Permanent electric dipoles are, e. g., poly(vinylidene fluoride-trifluoroethylene)(P(VDF-TrFE)) copolymer particles that were already studied experimentally in two dimensions. These particles are of nanometer size and possess a permanent dipole moment. The dipolar interaction is of the strength $\lambda \approx 1k_B T$. A phase transition from a ferroelectric phase to a paraelectric phase is known for these particles. Recent investigations showed a further order-disorder phase transition, illustrated in Figure 2. At a high temperature of 30°C no order is found, indicated by the black areas in the Brewster angle microscopy image, see Figure 2(b). Whereas at 15°C large domains of high order, indicated by the white areas in Figure 2(a), are present. Beside particles that possess a permanent

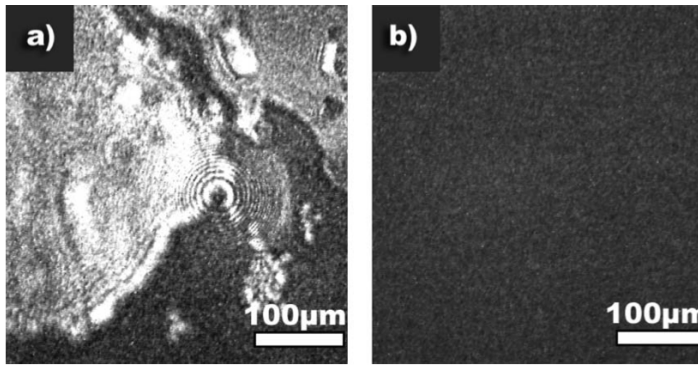


Figure 2: Brewster Angle Microscopy images of P(VDF-TrFE) at a) 15° and b) 30°. [Image taken from [126]]

dipole moment, systems comprised of induced dipoles are also of crucial importance in the design of new materials. The directed assembly can be achieved by applying an external field to, e. g., micron sized colloids, where SiO_2 with a size of $r = 2.2\mu\text{m}$ is a typical realization. In [87] the field is applied with a high frequency ($f = 1\text{MHz}$) to disable movement of the particles due to a field gradient. The resulting induced dipoles interact with a strength up to $\lambda \approx 15k_B T$ and build dipolar chains and hexagonal packed structures, see the experimental snapshots in Figure 3. Increasing the field strength leads to stronger dipolar interactions and thus to strong pattern formation.

Further examples of real systems that are object to intense experimental research focusing on directed (electric field-induced) self-assembly of polarizable colloids are dielectrophoresis experiments with latex particles of micron size [19, 173, 112], supra-molecular aggregates with dipole moments [199], and magnetic field-induced pattern formation of superparamagnetic colloids [125, 135].

In the above mentioned cases, the dominant interactions are dipolar in character. Another example of anisotropic particles is the broad class of so-called "patchy" colloids consisting of nano-particles with adhesive functional molecular groups [169, 201], which yield short-ranged directional interactions (such as, e. g., proteins [136]). Moreover, within the last few years there has been significant progress in the synthesis of "Janus"-like particles consisting of two hemispheres with different physical or chemical properties [180, 90, 130].

From the theoretical perspective, computer simulations are used since the 1970's to study polar and polarizable fluids [191, 3]. The long-range character of the dipole-dipole interaction gave rise to difficulties in computing, e. g., dielectric properties of polar fluids. One attempt is to truncate the interaction at a cut-off radius and to treat the effect of particles outside the cut-off in an average way, the so-called Reaction Field method [191]. A further approach is the use of perturbation theory to include the influence of particles beyond the cut-off radius [175]. The effect of taking the long tail of the interac-

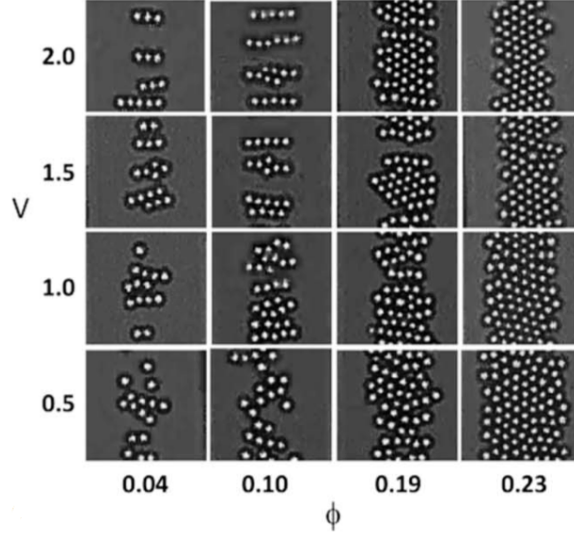


Figure 3: Video microscopy images of induced dipoles as function of the surface fraction Φ and field amplitude V . [Image taken from [87]]

tion into account turned out to have a strong impact on the physical properties of model systems with dipolar interactions [12] and lead to the development of more accurate techniques to deal with the long-range interactions. The Ewald summation technique has proved itself to compute the true dipolar interaction correctly and efficiently compared to other techniques [1, 34, 117] and established itself as the “standard” technique to treat dipolar interactions. In these early studies Dipolar Hard-Spheres (DHS) are used as the particle model that allows to focus on the dipolar interaction, where a point dipole is embedded into a simple Hard-Sphere. In order to take a possible van-der-Waals interaction into account the Stockmayer (SM) particle model, a combination of a point dipole and a Lennard-Jones potential, has also been extensively used. The Dipolar Soft-Spheres (DSS) particle model is somehow between the DHS and the SM model, and is established as the third “standard” model to investigate dipolar particles.

With increasing computational power more effort was made to understand the phase behavior and self-assembly of systems comprised of dipolar particles via computer simulations in the 1990’s. Early analytical and simulation works revealed a phase diagram of dipolar particles similar to the van-der-Waals fluid, including a vapor-liquid phase separation [162]. Extensive Monte-Carlo (MC) simulations with DHS and the Ewald summation technique showed that no condensation transition takes place, contrary to earlier findings. The condensation is suppressed by chain formation in strongly coupled systems, leading to a string fluid rather than a gaseous phase [188, 32]. These results turned out to be true also for two-dimensional dipolar systems, where chains and pronounced ring formation was found and no gas-liquid

phase separation seems to be present [101]. A full understanding even of simple dipolar model fluids is still lacking [71]. This is reflected by the ongoing debate on the existence and nature of a vapor-liquid transition in systems with additional attractive interactions [70, 78]. This is confirmed by recent simulation studies (see, e.g., [29, 49, 56, 138]), theoretical approaches [77, 164, 91, 104], and by experiments [153]. On the other hand, supplementing the particle interactions by spherically symmetric, attractive (e.g., van-der-Waals like) contributions, as in the SM fluid, yields stable vapor and liquid phases up to large values of the effective dipolar coupling constant (measuring dipolar versus dispersive forces) [70, 78, 50]. Still, computer simulations of strongly coupled dipolar fluids remain to be challenging due to very long equilibration times and sampling problems.

Beside the still open question of the vapor-liquid transition, the equilibrium self-assembly of (possibly anisotropic) high-density phases is a further point of interest. Molecular Dynamics (MD) simulation studies discovered the existence of a continuous or weak first-order phase transition into a ferroelectric liquid phase of DSS [185, 189]. This was confirmed by analytical approaches [162], however, it is still not clear if this phase is stable or metastable with respect to the solid phase [91, 62]. Three dimensional dipolar systems build a ferroelectric solid phase, which was found for DHS [189] and SM particles [62]. In systems confined to two dimensions the picture is completely different. When the density approaches crystallization, simulations discover frustrated vortex structures but no long-range ordering [101, 186, 104]. Mermim and Wagner showed the absence of a ferromagnetic or anti-ferromagnetic phase for a Heisenberg model in two dimensions, due to the lack of a long-range order at non-zero temperature in two-dimensional systems [109]. MC simulations showed however, that at zero-temperature two-dimensional dipoles build a ferroelectric phase if placed on a hexagonal lattice and an anti-ferroelectric phase if placed on a square lattice [139]. A full understanding of this question is still lacking.

In addition the equilibrium self-assembly phenomena such as the (reversible) formation of strings, rings, and percolated networks is of high interest. Particular effort has been recently devoted to dynamic phenomena such as gelation and structural arrest [200]. The field of gel formation is, compared to the above mentioned questions concerning the gas-liquid phase transition and the high density phases of dipolar systems, less investigated. During the last years increasing effort has been made to illuminate the dynamic properties of different systems that show a gel-phase by using computer simulations. While most particle models exhibit large and even percolated clusters at sufficiently low densities and sufficient strengths of anisotropic interactions, anomalous dynamic behavior characteristic of gelation only occurs in specific systems [200]. Polymer chains are used as a

typical model systems that reveal unusual dynamics at low densities due to gelation [97]. Experimental works showed the existence of a gel phase in, e. g., colloidal systems with an additional short-ranged attractive interaction, emerging from depletion effects [148]. Another important example that has recently been subject to intense research is the class of patchy particles. These particles are complex colloids whose features are an anisotropy in their inter-particle interaction and their limited valence in bonding. These systems have been studied in three [108, 140] and two dimensions [37] and reveal a pronounced gel-phase even at low densities. The picture of gelation in dipolar systems is even less clear. An example of a dipolar system exhibiting (reversible) gelation is a fluid of dumbbells which consists of a positively and negatively charged sphere [24]. On the other hand, to our knowledge, no gel-like dynamics has so far been reported for systems of dipolar DHS and DSS.

The major questions we investigate in the present work are illuminating the above mentioned fields of highly active research of dipolar systems. In particular, one major interest of the present work is to elucidate the questions of the vapor-liquid transition of dipolar fluids. We focus on the two-dimensional case due to the current experimental progress on such systems. We investigate by MC computer simulations the vapor-liquid transition of quasi-2D Stockmayer fluids, where the particles are confined to a plane but possess three-dimensional (3D) dipole moments. We consider both systems in zero field and systems in the presence of homogeneous external fields directed either perpendicular to the surface or along an in-plane direction. In addition, recent works have shown that an interesting self-organization process takes place when such particles are exposed to time-dependent rotating fields. The external field induces the formation of clustered structures of particles with an induced dipole moment [38, 152] or particles carrying a permanent dipole moment as recently shown [184, 195]. This part is a contribution to a project carried out by Sebastian Jäger in the framework of his PhD thesis. Besides locating coexistence curves for these systems, our aim is to explore the performance of two state-of-the-art MC techniques, i. e., Successive Umbrella (SU) sampling [176] and Wang-Landau (WL) sampling [181], which have already been successfully applied to 3D systems [49]. Moreover, we address the influence of the system size by simulating systems of different sizes.

The zero-field situation has earlier been considered by Gao *et al.* [51] who performed Gibbs Ensemble (GE) MC simulations for several, yet relatively small values of the dipolar coupling parameter. Just very recently, Ouyang *et al.* [127] reported MD results on the condensation transition in zero field for a larger range of coupling parameters, focussing, however, on one particular (quite small) system size. In this work we provide MC results for larger coupling strengths and different system sizes. The influence of external fields on the condensation

transition has, so far, only been studied for 3D Stockmayer fluids [155, 25, 106] and for confined Stockmayer fluids in slit-pore geometries [135, 86]. Clearly, for confined and 2D dipolar systems the direction of the field is crucial. In particular, in-plane fields support attractive head-to-tail configurations and thus generally favor the condensation transition. On the other hand, sufficiently strong perpendicular fields generate long-range, repulsive interactions due to the out-of-plane alignment of the dipoles. For not too small van-der-Waals attraction, one thus obtains a 2D system with competing interactions. Systems of this type were recently shown to have a rich phase behavior involving several fluid phases [75, 11]. A rotating field can induce a layer formation in dipolar system in three dimensions [79]. By applying such a field to our quasi two-dimensional case we obtain an effective interaction between the dipoles which also leads to a condensation transition.

Beside the vapor-liquid phase separation we also explore by means of computer simulations the self-assembly and phase behavior of a two-dimensional system of colloidal particles with modified dipolar interactions. Specifically, in this work we consider a model which has recently been proposed in [56] to simulate dipole-like systems via the so-called Discontinuous Molecular Dynamics (DMD) method [5, 64, 56], a special form of (event-driven) MD. In this context, the true, continuous, long-range dipolar potential is approximated by a discontinuous, three-step potential which (roughly) preserves the directional dependence of the original interaction, particularly the preference of head-tail-arrangements, but restricts its range to a short range interaction. The resulting model may be seen as some sort of screened dipolar system; in fact, in systems of polarizable colloids such a screening induced by charges in the solvent is certainly realistic. Experimental examples of such systems are reported in [102] and [48]. In these studies induced dipolar particles are generated via applying an AC electric field to dielectric particles. The particles are suspended in water, yielding a pronounced screening which can be adjusted through the pH of the solvent. More generally, our model may be considered as simple representative of a networking-forming system. The big advantage is that it is computationally much less costly than corresponding models with true electrostatic interactions. Indeed, investigating this model in a three-dimensional set-up for a wide range of parameters [56], a variety of complex (aggregated or positionally ordered) states can be observed, and an even broader variety is found in corresponding two-component systems [57].

Here we investigate the (one-component) model of [56] in 2D, focussing on both, static and dynamic phenomena. Our motivation to explore in more detail the 2D situation is driven, on the one hand, by the fact that many experiments involving self-assembling colloids are actually done at surfaces and/or in thin films [19, 125, 87, 174]. Moreover, from a conceptual point of view, research on true dipolar

systems has revealed that the spatial dimension of the system strongly affects the (equilibrium) behavior; examples being the absence of spontaneous, global polarization at high densities in 2D [104, 92, 8], the preference of rings (relative to chains) at low densities [161], and the confinement-induced shift of the vapor-liquid coexistence curves in dipolar systems with additional van-der-Waals interactions [143]. We investigate the model system through a number of order parameters. Based on these quantitative measures, we are able to map out a sketch of a phase diagram involving an isotropic fluid, a polymerized fluid, a percolated gel, and a hexagonal crystal. Most notably, we show that the dynamics in percolated phase has gel-like features. Moreover, the crystalline phase is not only translationally ordered, but also of ferroelectric orientation, which was not found for true dipolar interactions [8].

Another focus of this work is the self-assembly of particles with induced dipole moments. Recent works are focusing on the assembly and manipulation of colloidal particles by external control through applying electric or magnetic fields [173, 87]. The directed assembly of colloidal particles can be used to obtain desired structures, e. g., dipolar chains [113, 41]. Nematic colloidal crystals show similarities to such systems of dielectric particles exposed to an external field. One can obtain dipole-like and/or quadrupole-like interactions that lead to self-organized structures into and perpendicular to the nematic order in two dimensions [116, 122].

The assembly into chains has been observed in experiments with induced dipoles [19] as well as with ferrofluids [193]. The dynamics of the clustering of ferrofluids due to the response to an external field has also been investigated [69]. The occurrence of dipolar superstructures where dipolar chains build zipped bundles of several chains are reported in [93, 68]. On a theoretical level such aggregation as response to an external field has been studied by computer simulations where columnar structures with hexagonal ordering were found [74]. The assembly into chains and columns has also a strong impact on the dynamics of such a system, as displayed by, e. g., anomalous diffusion [85].

Inspired by current work in designing complex colloidal particles that assemble into two dimensions on a thin film by applying an external field into one fixed direction [48], we propose and study a completely new theoretic model. This particle model shows the rare phenomenon to assemble parallel and perpendicular to the external field. Previous works have shown that the assembly of particles across the direction of an external field can be achieved by using, e.g., binary mixtures of particles with different dielectric properties [60, 52]. These works can explain chaining of dielectric particles perpendicular to an external field as an effect of a different permittivity. However, the transverse chaining is considerably weaker compared to our system

and no networks were observed or systematically investigated. In this work we study the static and dynamic properties of colloidal networks by applying various simulation techniques, namely MC, MD and non-overdamped Brownian Dynamics (BD). Further we show how the physical properties of the network structures can be tuned by macroscopic parameters.

To summarize, the main objectives of this work are to study the phase behavior and self-assembly of systems with dipolar and dipole-like interactions confined to two dimensions by computer simulations. Starting with three-dimensional SM particles restricted to a plane, we are investigating condensation phase transitions of particles with different coupling strength and exposed to various external field. Further, we compare the performance of two state-of-the-art simulation techniques to locate the condensation phase transition. Furthermore, we use the DMD simulation technique and a different particle model that mimics locally the dipolar interaction. The long-range character of the dipole-dipole interactions is not taken into account. We study a broad range of densities and temperatures and we are able to draw a sketch of the phase diagram of such dipole-like colloids. We use several order parameters and system sizes to locate the transition lines. Finally, we are focusing on induced dipoles, where our particle model consists of a mixture. One sort are simple induced dipoles, whereas the second sort is comprised of particles containing two induced dipoles, one pointing into the field direction, and one opposed to it. The model system assembles parallel and perpendicular to the external field and we are studying the percolation transition in both directions as well as the dynamic properties of the percolated phases. Moreover, we are investigating the influence of the composition and density on the percolation transition.

The rest of this work is organized as follows. In Chapter 2 we introduce the necessary background from statistical mechanics needed in this work. The different particle models that are used and a short overview of phase transitions is given in this chapter as well. Further, we introduce the phenomenon of percolation. The background is completed by a brief introduction to computer simulations, namely the Monte-Carlo (and more advanced alternatives) and the Discontinuous Molecular Dynamics simulation technique. We also discuss relevant parameters that can be studied by computer simulations and are important in our investigations. We then present our results of using advanced MC techniques to determine the phase separation of a quasi two-dimensional Stockmayer fluid in Chapter 3. We first investigate a weakly, medium, and strongly coupled system without an external field and compare the results of the different techniques with each other and with results from literature. We also analyze the capability of different MC approaches in terms of computational effort and finite-size effects. Subsequent to that, we apply an external field

perpendicular and parallel to the plane and study the influence on the phase separation. Finally, we locate the phase separation of a similar system when exposed to a rotating external field. The following Chapter 4 contains numerical results obtained by the DMD simulation technique of two-dimensional dipoles. We first study the low density phases where we focus on the static and the dynamic properties. This is followed by an investigation of the ordering phenomena observed at high densities. We then summarize the sketch of the phase diagram. In Chapter 5 we present our results of a system containing particles with one and two induced dipoles in two dimensions. After briefly discussing the behavior of each particle model itself, we focus on mixtures of such particles and investigate the percolation transition parallel and perpendicular to the field. The corresponding dynamic properties are also subject of investigation in this chapter. This work is then concluded by Chapter 6, where we summarize the results and discuss possible future work.

2

STATISTICAL MECHANICS AND COMPUTER SIMULATIONS

In this chapter we introduce the theoretical background needed in this work. We start by introducing the model system used in the employed computer simulations. We then introduce the canonical and grand-canonical ensemble from the point of view of statistical mechanics and how to compute averages in these ensembles using computer simulations.

2.1 PARTICLE MODELS

2.1.1 *Continuous model of quasi two-dimensional dipoles*

In this work we are interested in the behavior of dipolar particles that are confined to a plane, but possess a three-dimensional dipole moment. Such a model is realistic by having in mind permanent electric or magnetic dipoles on a thin film [93, 126]. The total interaction of the particles is modeled via a combination of two potentials. The Lennard-Jones (LJ) potential, defined by

$$U_{\text{LJ}}(r_{ij}) = 4\epsilon \left[\left(\frac{\sigma}{r_{ij}} \right)^{12} - \left(\frac{\sigma}{r_{ij}} \right)^6 \right] \quad (2.1)$$

where ϵ describes the maximum of the attractive interaction and σ is the particle diameter and the regular dipole-dipole (DD) potential

$$U_{\text{DD}}(i, j) = \frac{1}{r_{ij}^3} \left[\boldsymbol{\mu}_i \cdot \boldsymbol{\mu}_j - \frac{3}{r_{ij}^2} (\boldsymbol{\mu}_i \cdot \mathbf{r}_{ij})(\boldsymbol{\mu}_j \cdot \mathbf{r}_{ij}) \right]. \quad (2.2)$$

In the above equations $r_{ij} = |\mathbf{r}_{ij}| = |\mathbf{r}_i - \mathbf{r}_j|$ is the distance between particles i and j . In Equation 2.2 $\boldsymbol{\mu}_i$ represents the vector of the dipole moment (with $|\boldsymbol{\mu}_i| = \mu \forall i = 1, \dots, N$). The resulting total interaction defines the so-called Stockmayer [156] model. Using the Stockmayer model to study the condensation transition has the advantage that the system displays a clear vapor-liquid transition [171, 170, 70]. In contrary, the DHS and DSS systems assemble strongly at low-densities

Table 1: Definition of reduced units for quasi two-dimensional Stockmayer particles

Dipole moment	μ^*	=	$\sqrt{\mu^2/\epsilon\sigma^3}$
Temperature	T^*	=	$k_B T/\epsilon$
Density	ρ^*	=	$N\sigma^2/A$
Chemical potential	$\tilde{\mu}^*$	=	$\tilde{\mu}/\epsilon$
External field	B_{ext}^*	=	$B_{\text{ext}}\epsilon\sigma^3$

and these phases are nowadays rather termed as isotropic fluid phases [164, 29].

In addition, we are aiming to study the influence of an external field on the phase behavior of the SM particle model. If such a field, \mathbf{B}_{ext} , is applied, an additional term in the Hamiltonian arises from the interaction of dipole i with the field, that is,

$$U_{\text{ext}}(i) = -\boldsymbol{\mu}_i \cdot \mathbf{B}_{\text{ext}}. \quad (2.3)$$

For practical reasons one uses reduced units in computer simulations. By reducing the quantities used in a actual simulation we can bring the quantities into the same order of magnitude and can reduce numerical errors. We define the reduced units used in this work for quasi two-dimensional SM particles in Table 1.

2.1.2 Discontinuous model of two-dimensional dipoles

Beside MC simulations we employ in the present work also a further technique, namely DMD simulations [5, 64, 56], introduced in Section 2.4.5. The reason is that this method is a fast alternative to traditional MD simulations. In order to use DMD simulations we introduce a particle model that takes the need of discontinuous potentials into account. Such a model is necessary for the use of DMD simulations. The particle model does not represent the true dipolar interaction, as will become clear in the present paragraph. We thus introduce the term dipole-like colloid instead of dipolar colloids. We model each dipole-like colloid by two oppositely “charged” particles embedded in a Hard-Sphere (HS). In Figure 4(a) we show a schematic representation of our model.

Like charges repel one another by a three-step square-shoulder potential (U_{SS}), and unlike charges interact via an attractive three-step square-well potential (U_{SW}). The HS potential is defined as

$$U_{\text{HS}}(r_1) = \begin{cases} \infty, & \text{if } r_1 \leq \sigma \\ 0, & \text{if } r_1 > \sigma, \end{cases} \quad (2.4)$$

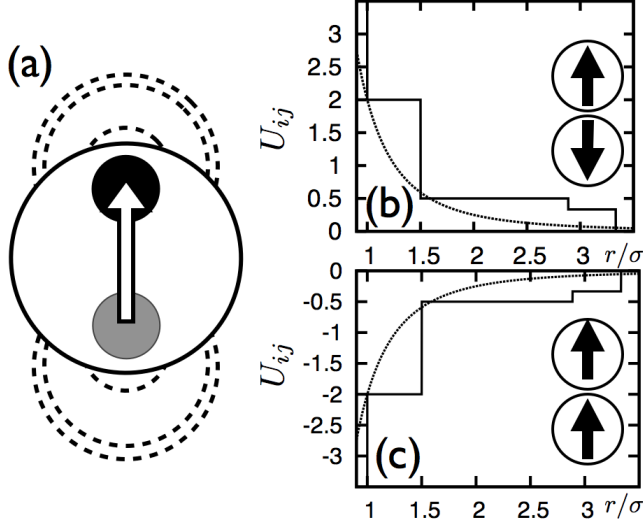


Figure 4: Schematic representation of our model. The dipole-like colloids are represented by two oppositely charged spheres (shown by black and grey) embedded into a hard sphere. The dashed lines indicate the potential steps. In (b) and (c) we plot the total interaction potential (U_{ij} in units of μ^2/σ^3) on the y-axis and the distance (r/σ) on the x-axis, related to the most repulsive and attractive configurations of two particles [see cartoons in (b) and (c)]. The dashed lines indicate the corresponding potentials for true dipoles.

where r_1 is the distance between two HS and σ is the HS diameter. Further, the “charge-charge” interactions are defined by

$$U_{SS}(r_2) = \begin{cases} \infty, & \text{if } r_2 < \sigma_1 \\ \epsilon_1, & \text{if } \sigma_1 < r_2 < (1 + \lambda_1)\sigma_1 \\ \epsilon_2, & \text{if } (1 + \lambda_1)\sigma_1 < r_2 < (1 + \lambda_2)\sigma_1 \\ \epsilon_3, & \text{if } \sigma_2 < r_2 < (1 + \lambda_3)\sigma_1 \\ 0, & \text{if } r_2 > (1 + \lambda_3)\sigma_1 \end{cases} \quad (2.5)$$

and

$$U_{SW}(r_2) = \begin{cases} \infty, & \text{if } r_2 < \sigma_1 \\ -\epsilon_1, & \text{if } \sigma_1 < r_2 < (1 + \lambda_1)\sigma_1 \\ -\epsilon_2, & \text{if } (1 + \lambda_1)\sigma_1 < r_2 < (1 + \lambda_2)\sigma_1 \\ -\epsilon_3, & \text{if } \sigma_2 < r_2 < (1 + \lambda_3)\sigma_1 \\ 0, & \text{if } r_2 > (1 + \lambda_3)\sigma_1. \end{cases} \quad (2.6)$$

In Equation 2.5 and Equation 2.6, r_2 is the distance between two embedded charges of different HS particles. The charged particles have a diameter $\sigma_1 = 0.3\sigma$. The potential steps are defined by their magnitudes ϵ_1, ϵ_2 , and ϵ_3 , respectively, and the step widths are λ_1, λ_2 , and λ_3 . To define the actual values of these parameters we first need to introduce reduced units. We define a reference interaction strength

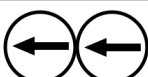
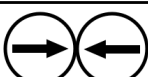
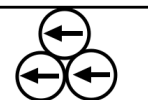
Configuration	U_{ij} True Dipoles	U_{ij} DMD Model
	$\frac{\mu^2}{\sigma^3}$	$0 < U_{ij} < \frac{2\mu^2}{3\sigma^3}$
	$-\frac{\mu^2}{\sigma^3}$	$-\frac{2\mu^2}{3\sigma^3} < U_{ij} < 0$
	$-2\frac{\mu^2}{\sigma^3}$	$-2\frac{\mu^2}{\sigma^3}$
	$2\frac{\mu^2}{\sigma^3}$	$2\frac{\mu^2}{\sigma^3}$
	$-\frac{3\mu^2}{2\sigma^3}$	$-\frac{8\mu^2}{3\sigma^3} < U_{ij} < -\frac{4\mu^2}{3\sigma^3}$

Figure 5: Interaction energies U_{ij} for various two-particle configurations, shown in the left column. The middle column gives the energy values according to the true dipole-dipole interaction, while the right column gives the values according to our model. Within the latter, the uncertainty of the energies appearing at the side-by-side configurations arises from the fluctuations of the embedded charges within the HS.

by $\epsilon^* = \mu^2/\sigma^3$, where μ is the target dipole moment we aim to model. Dimensionless potential steps are then defined by $\epsilon_\alpha = \epsilon_\alpha/\epsilon^*$, where $\alpha = 1, 2, 3$. Further, the reduced temperature is given by $T^* = k_B T/\epsilon^*$, where k_B is the Boltzmann constant and T is the temperature. We reduce the density in the standard way by $\rho^* = N\sigma^2/A$, where A is the area of the simulation box. The time in the simulations is also reduced by $t^* = t/\sqrt{\sigma^2(m/k_B T)}$, where m is the mass of the particles.

The parameters appearing in Equation 2.5 and Equation 2.6 are chosen in such a way that the resulting total potential matches, as far as possible, the full dipole-dipole interaction in Equation 2.2. Specifically, following an earlier DMD study on dipolar-like colloids in three dimensions [56], we choose $\lambda_1 = 0.500$, $\lambda_2 = 1.887$ and $\lambda_3 = 2.333$. The potential depths are $\epsilon_1^* = 2.000$, $\epsilon_2^* = 1.500$ and $\epsilon_3^* = 0.500$. The resulting total potential for two relevant configurations is plotted in Figure 4(b) and (c). The choice of these parameters is somehow substantial to our model. On the one hand we aim to match the true dipolar interaction locally but on the other hand we want to keep the model as simple and as short ranged as possible. We run test calculations with slightly different parameters which affected the behavior of the model only qualitatively and modest.

To locate the embedded charges within the hard spheres, we use the method proposed in and originally used for polymers [133]. Both charges within the particle are bound to the sphere but their distance

(in units of σ) is allowed to move between $(1 \pm \delta/2)$ [14]. By this choice it is guaranteed that the dipole vector always points through the center of the nano-particles while some fluctuations in its length are allowed. This effect can be seen as smearing out the sharp edges of the discontinuous potential. In our simulations we set $\delta = 0.04$. Clearly, our model does not account for the long-range character of the true dipole-dipole interactions; however, it mimics the dipole-dipole interaction locally. This is illustrated in Figure 5 where we show the pair energies for different configurations according to the true dipole-dipole interaction, on the one hand (middle column), and our model, on the other hand (right column). Within our model, the uncertainty of the energy of the side-by-side configurations results from fluctuations emerging from the parameter δ . From Figure 5 it becomes clear that the head-to-tail configuration is the energetically most favorable one, as it is the case for true dipoles. Side-by-side configurations with parallel (antiparallel) orientations are less unfavorable (favorable) than for the true interaction. A particularly important feature is that our model implies a lower energy for the three-particle configuration shown in the last row of Figure 5. In the best case, depending on the positions of the embedded charges, the energetic advantage compared to true dipoles is 1.78 times larger. This configuration points into the direction that this model reveals a different behavior from true dipoles at high densities where such configurations become dominant.

2.2 ENSEMBLES

2.2.1 Canonical ensemble

For dipolar systems the Hamiltonian is given by

$$\begin{aligned}
 H(\mathbf{r}_i, \mathbf{r}_j, \mathbf{p}_i, \mathbf{p}_j, \mathbf{u}_i, \mathbf{u}_j, \boldsymbol{\mu}_i, \boldsymbol{\mu}_j) = & \frac{1}{2} \sum_i^N \sum_j^N U_{LJ}(r_{ij}) \\
 & + \sum_i^N \sum_j^N U_{DD}(r_{ij}, \boldsymbol{\mu}_i, \boldsymbol{\mu}_j) + \sum_i^N \frac{\mathbf{p}_i^2}{2m} + \sum_i^N \frac{I\mathbf{u}_i}{2}, \quad (2.7)
 \end{aligned}$$

where in the above equation r_{ij} is the distance between particles i and j , U_{LJ} is defined in Equation 2.1 and U_{DD} in Equation 2.2. The momenta are given by \mathbf{p}_i , the moment of inertia of the spherical particles by I and \mathbf{u}_i represent the angular velocities. The mass of each particle is given by m .

In classical statistical mechanics a system of N particles is described by the density of states in the phase space Γ . The phase space is spanned by $5N$ coordinates for dipolar systems, with $3N$ coordinates emerging from the translational degrees of freedom and $2N$ coordi-

nates from the rotational ones. The canonical probability distribution for dipolar systems is thus given by

$$\rho_c = Z_c^{-1} \exp\left(\frac{-H(\Gamma)}{k_B T}\right), \quad (2.8)$$

where the partition function is given by

$$Z_c = \int d\Gamma \exp\left(\frac{-H(\Gamma)}{k_B T}\right). \quad (2.9)$$

We have introduced the notation

$$d\Gamma = \frac{1}{h^{5N} N!} dr dp d\mu du, \quad (2.10)$$

where $N!$ emerges from the indistinguishability of the particles and h is the Planck's constant describing the phase space volume.

2.2.2 Grand-canonical ensemble

Extending the canonical ensemble with particle exchange leads to the definition of the Grand-canonical (GC) ensemble. In this ensemble the chemical potential μ , the volume V , and the temperature T are kept constant, whereas the particle number N is allowed to fluctuate.

The grand-canonical probability distribution is given by

$$\rho_{gc} = Z_{gc}^{-1} \exp\left(\frac{-(H - \mu N)}{k_B T}\right), \quad (2.11)$$

with the grand canonical partition function

$$Z_{gc} = \sum_N \exp(\mu N / k_B T) \int d\Gamma \exp(-H / k_B T). \quad (2.12)$$

2.2.3 Configurational integral

We have introduced the canonical partition function in Equation 2.9, where the Hamiltonian for the dipolar system is given in Equation 2.7. In general, the Hamiltonian can be divided into a translation, rotation and a potential part ($H = K + R + U$). The translational kinetic part of the Hamiltonian is given by

$$K = \sum_i^N \frac{\mathbf{p}_i^2}{2m}, \quad (2.13)$$

the rotational kinetic part by

$$R = \sum_i^N \frac{I \mathbf{u}_i^2}{2}, \quad (2.14)$$

and the potential part by

$$U = U_{LJ}(r_{ij}) + U_{DD}(r_{ij}). \quad (2.15)$$

The partition function can be divided into three contributions, respectively,

$$Z_c = Z_K Z_R Z_U. \quad (2.16)$$

The integration over the momenta can be carried out, since this integral is independent of the orientations and positions and we obtain [146]

$$Z_K = \frac{V^N}{N! \Lambda^{3N}}. \quad (2.17)$$

The factorization into the kinetic and potential part is not simply applicable to the rotational kinetic part. It is shown in [58] that a transformation of the orientation and the angular momentum with the use of Euler angles and their conjugate momenta can be carried out. This transformation leads finally to a factorisation of the rotational kinetic degrees of freedom, similar to the translational kinetic part and we obtain

$$Z_R = \frac{1}{\Lambda^{2N}} \frac{I^N}{m^N}. \quad (2.18)$$

In MC simulations one uses only the configurational part, that depends on the positions and orientations of the particles. If we are interested in absolute values of, e. g., the chemical potential or the pressure, we add the ideal gas part. As shown, we do not need to take the translational and rotational kinetic part into account in computing the partition function since this adds simply a constant. Thus, from now on we will omit these parts in the rest of this work.

2.2.4 Ergodicity

The ergodic hypothesis states that each trajectory in phase-space will come in the long run arbitrarily close to every conceivable microstate. Thus, the result of a time average, \bar{A}_t is equal to the result of an ensemble average $\langle A \rangle$. In this case, we obtain for a function f in phase-space [146]

$$\lim_{T \rightarrow \infty} \frac{1}{T} \int_0^T dt f(q(t), p(t)) = \frac{1}{\Omega(E)} \int d\Gamma f(q, p). \quad (2.19)$$

If we choose $f(q, p) = \Theta(q, p \in G)$, with G as a part of the energy shell accessible to the system, we obtain for large T

$$\frac{\tau_G}{T} = \frac{|\Gamma_G|}{\Omega(E)}, \quad (2.20)$$

where τ_G is the time the trajectory spends in G and $|\Gamma_G|$ is the phase-space volume of G . From this follows that the time the system spends in the improbable region G is small. This statement is of particular importance for computer simulation, MC as well as MD simulations.

2.3 PHASE TRANSITIONS

The state of matter is in general characterized by different phases that can be classified by, e. g., translational or rotational symmetry and that differ in their thermal, mechanical, and electro-magnetic properties. By changing external thermodynamic potentials, e. g., temperature, pressure, or chemical potential, a system can change its properties from one phase to another, i. e., undergo a phase transition. These transitions change the symmetry or the order of the system. Examples are the ferromagnetic transition or demixing transitions of two component systems. Analytical approaches are often not able to provide a deep understanding of phase transitions in statistical ensembles. That is where computer simulations come into play. They provide a framework for the understanding and classification of phase transitions. In this section we will briefly introduce a survey of phase transitions that is needed in this work.

A simple classification of phase transitions was introduced by Ehrenfest, stating that a phase transition of n -th order is defined by a discontinuity of the n -th derivative of a thermodynamic potential, e. g., the Gibbs Free Energy (G). A more comprehensive definition was proposed by Fisher. It is the same for a first-order phase transition but all others are called continuous transitions since the first derivative of the thermodynamic potential changes continuously at the transition [168]. Before we discuss the difference of a first-order and a continuous phase transition we need to introduce the concept of the order parameter.

A phase transition changes the symmetry or the order of the system. In order to describe this change one makes use of an appropriate order parameter. This quantity is defined to be non-zero in the ordered phase and identically zero in the unordered phase. Examples for order parameters are the magnetization in a ferromagnet or the difference of the density of the gas and liquid phase in a condensation transition. The general concept of an order parameter is defined as

$$\Phi = -\frac{\partial G}{\partial h} \quad (2.21)$$

where h is an external potential, e. g., the temperature, an external magnetic field or the pressure. The behavior of the Gibbs Free Energy and the order parameter at a first-order and continuous phase transition is illustrated in Figure 6. The left panels show G and Φ as function of h , where at the critical field h_c a first-order phase transition takes place, indicated by the discontinuity of the first derivative of G and a jump of the order parameter at the transition. On the other hand the derivative of G displays no discontinuity at h_c for a continuous transition, shown in the right panels, but the first derivative Φ has a infinite slope at h_c .

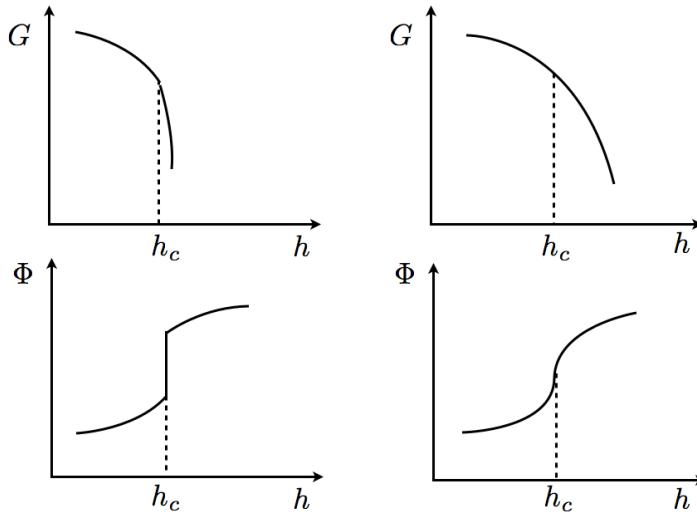


Figure 6: Gibbs Free Energy G and the order parameter Φ as function of the external field h at a first-order and second order phase transition. The value h_c refers to the critical field strength.

2.3.1 First-order phase transition

To determine the existence of a first-order phase transition in a computer simulation, specifically by using the MC technique, the order parameter distribution $P(\Phi)$ is a useful function. The distribution of the order parameter represents the density of states and is thus closely connected to the partition function. They differ only by an additive constant. This distribution is related to G by the relation [98]

$$G(\Phi) = -k_B T \ln[P(\Phi)]. \quad (2.22)$$

Recording a histogram of Φ provides us with a way to measure G of a system. If the system is at the low order state at $h < h_c$ we find one peak of $P(\Phi)$ corresponding to one stable minimum of G . By approaching h_c the potential G displays a second minimum, which represents a metastable state that coexists with the stable state. At h_c we find two equal minima that are expressed by a bimodal structure of $P(\Phi)$, where both peaks have equal areas under the peaks, i. e., are equally probable. Finally, at $h > h_c$ the histogram $P(\Phi)$ displays again only one peak that refers to the high order state. How this relation can be used to determine a vapor-liquid phase transition by MC simulations will be shown in Section 2.4.4.

2.3.2 Continuous phase transition

As introduced above a continuous phase transition is characterized by a discontinuity of the second (or higher) derivate of G with respect to the external field. This can be used in computer simulations to determine if the transition is, e. g., of second order. Computing the susceptibility defined as

$$\chi = - \left(\frac{\partial^2 G}{\partial h^2} \right)_{\tau}, \quad (2.23)$$

is a possible approach to a continuous transition. The specific heat defined by

$$c = -T \left(\frac{\partial^2 G}{\partial T^2} \right)_{h}, \quad (2.24)$$

is an example of a quantity related to the susceptibility. This quantity makes a jump or diverges at the transition and provides us with a hint to characterize the transition in a computer simulation. In this work we did not attempt to study continuous phase transitions in more detail, however, we introduce some more concepts related to continuous transitions.

Continuous phase transitions close to the critical point are characterized by a power law behavior of characteristic properties of the system. The order parameter, Φ , and the susceptibility, χ , are proportional to such power laws that define the so-called critical exponents. Using $\tau = (T - T_c)/T_c$ we can express their behavior accordingly as, e. g., for the order parameter $\Phi \propto (-\tau)^\beta$, for the susceptibility $\chi \propto |\tau|^{-\gamma}$ or the specific heat $c_v \propto |\tau|^{-\alpha}$. Experiments, computer simulations and theoretical models find different relations between the critical exponents, but we do not introduce them here. These relations can be explained by scaling laws. It turns out that the behavior of a phase transition is universal what is stated by the Universality Hypothesis [61]. It says that the critical exponents and the scaling functions are universal and depend only on

- the dimension of the system,
- the symmetry of the interaction,
- the range of the interaction (long or short range interaction).

The great importance of the critical exponents is based on the ability to measure these values experimentally and compare them to the theoretical predictions and computer simulations.

2.3.3 Percolation

A further phenomenon that is of importance in this work and that displays characteristics of a continuous phase transition is percolation.

We are starting to introduce percolation theory by considering a square lattice in two dimensions where each square or each bond between nodes can be occupied or not. The first case is referred to as side percolation, since two occupied squares are considered to belong to the same cluster if they share one side, whereas the second case is called bond percolation, since the nodes are in the same cluster if they share a bond. The percolation threshold, p_c , is the concentration of occupied sites or bonds at which an infinite network appears for the first time [154].

2.3.3.1 Percolation in one dimension

It is convenient to introduce the basic concepts of percolation theory in the one-dimensional case, where analytic solutions exist. We start with a chain of length L with $L \rightarrow \infty$. We find a cluster of size s with the probability $p^s(1-p)^2$, where p^s is the probability to find s occupied sites and $(1-p)^2$ is the probability that the left and right end are empty. The normalized cluster number is thus defined as

$$n_s = p^s(1-p)^2. \quad (2.25)$$

The probability a site belongs to a cluster of size s is then $n_s s$ and we conclude

$$\sum_{s=1}^{\infty} n_s s = p. \quad (2.26)$$

The probability that a randomly picked site belongs to a cluster of size s is

$$w_s = \frac{n_s s}{\sum_s n_s s}, \quad (2.27)$$

and the average cluster size is

$$S = \sum w_s s = \sum \frac{n_s s^2}{\sum n_s s}, \quad (2.28)$$

which can be solved analytically in one dimension and we obtain

$$S = \frac{1+p}{1-p}, \quad p < p_c. \quad (2.29)$$

It is clear that $p_c = 1$ in one dimension, since every unoccupied site destroys an infinite cluster of the chain. Therefore, we see that $S \rightarrow \infty$ as $p \rightarrow p_c$. We also introduce the correlation length that a site at distance r of an occupied site belongs to the same cluster by

$$g(r) = p^r, \quad (2.30)$$

and if r goes to infinity we obtain

$$g(r) = \exp\left(-\frac{r}{\xi}\right), \quad (2.31)$$

with the correlation length $\xi = -1/\ln p = 1/(p_c - p)$ for p close to p_c . The quantities S and ξ diverge close to the percolation transition similar to the critical behavior of continuous phase transitions.

2.3.3.2 Percolation in d dimensions

There are no analytic solutions for most percolation phenomena in higher dimensions, $d > 1$. To illustrate the difficulties in computing the percolation probability in higher dimensions we introduce a simple example. We consider the probability to find a cluster of size $s = 2$ in a two-dimensional square lattice. This resulting probability is the probability to find two occupied sites, p^2 , and six empty neighbour sites, $(1 - p)^6$. Further, the cluster can be orientated horizontally or vertically resulting in a factor 2 and we end up with the probability to find such a cluster, $2p^2(1 - p)^6$. For large clusters and higher dimensions it is not possible to find similar closed expressions for these probabilities, since the clusters are not linear in general but of complex shape.

However, one can derive expressions to describe the behavior of the above introduced quantities close to the percolation transition in dimensions $d > 1$. On the contrary to the one-dimensional case the normalized cluster number behaves at $p \rightarrow p_c$ according to

$$n_s \propto s^{-\tau} \exp(-cs), \quad (2.32)$$

where c depends on p with

$$c \propto |p - p_c|^{1/\sigma}. \quad (2.33)$$

This defines the quantity $s_\xi = 1/c$, which can be interpreted as the "cutoff" size that separates critical clusters from noncritical clusters by approaching the percolation transition. The mean cluster size also follows a power law according to

$$S \propto |p - p_c|^\gamma \quad (2.34)$$

with

$$\gamma = \frac{3 - \tau}{\sigma}. \quad (2.35)$$

These relations are just a few examples of the critical behavior of the clusters close to a percolation transition. However, they demonstrate the similarities with a continuous phase transition. In this work we consider fluid systems that are continuous. Percolation of continuous systems reveals to obtain similar power-law behavior as random percolation on lattice systems [30]. Recent simulations showed on the other hand that the critical exponents exhibit a strong dependence on the temperature, on the nature of the system and the cluster definition [178]. The question is still not solved, but since in this work we do not attempt to determine critical exponents of the percolation transition we do not discuss this problem further.

2.4 COMPUTER SIMULATIONS

During the last decades computer simulation established themselves as a powerful technique to study problems in many particle systems. With the growing computational power, simulations are capable to provide a powerful way to face challenging questions in theoretical physics, chemical engineering or material science. In this section we introduce the MC simulation technique along with advanced MC techniques to study first-order phase transitions. Further, we introduce DMD simulations that provide a possibility to study many particle systems, including dynamic properties and being extremely efficient. The fundamentals of this chapter are based on standard textbook of computer simulations [6, 46, 98].

2.4.1 Monte-Carlo simulations

In statistical mechanics one usually deals with multidimensional integrals as, e. g., the partition function of a system as introduced in the previous Section 2.2. The solution of these integrals is in most cases not possible by analytical means and thus one has to employ numerical methods. The MC method allows to solve such high dimensional integrals in a very efficient way. A brute force approach could be to randomly generate configurations of the many-particle system and to compute the Boltzmann factor of each configuration $\exp[-\beta U(\Gamma)]$. The partition function could then be estimated by [6]

$$Z \propto \frac{V^N}{M} \sum_{i=1}^M \exp[-\beta U(\Gamma_i)], \quad (2.36)$$

where $\beta = 1/k_B T$. But since for most configurations the Boltzmann factor is very small this procedure is highly inefficient because most generated configuration do not contribute significantly to the partition function.

2.4.1.1 Importance sampling

To overcome the aforementioned problem we choose the random configuration from a certain distribution. We make sure that we choose the configurations that have an important contribution to the partition function. We can write for an ensemble average of the observable A

$$\langle A \rangle = \int d\Gamma \rho(\Gamma) A(\Gamma) \quad (2.37)$$

with an appropriate distribution $\rho(\Gamma)$. The difficulty is to find the right choice for this distribution to make sure that we choose all configurations with the correct probability. For this purpose we construct a Markov chain with a limiting distribution. In general, a Markov process is defined as a memory-less process. That is, each state depends

only from the state before but not from earlier states. We assume the system goes from the old state (Γ_o) to the new state new (Γ_n). This transition can be described by a transition probability $\pi(o \rightarrow n)$. For all possible states (or configurations) we can build a stochastic matrix π that contains all transition probabilities. Accordingly to the Perron-Frobenius theorem such a stochastic matrix possesses one eigenvalue that is equal to unity. The corresponding eigenvector is the stationary distribution of the Markov chain. A further constrain to this matrix is ergodicity, that is, every state of the matrix has to be accessible which is important in the context of a physical system.

Now, we need to know how to construct such a Markov chain to sample an ensemble average. We can write down the probability density to find the system in a configuration around Γ by

$$\rho(\Gamma) = \frac{\exp[-\beta U(\Gamma)]}{Z}. \quad (2.38)$$

At this point it is necessary to introduce another important condition that the transition matrix has to obey, namely the Detailed Balance condition [46]

$$\rho(\Gamma_o)\pi(o \rightarrow n) = \rho(\Gamma_n)\pi(n \rightarrow o). \quad (2.39)$$

This condition guarantees the reversibility of the process and it ensures that the distribution of probabilities is stationary, i. e., in equilibrium. Let α be the probability of performing a trial move from Γ_o to Γ_n , that is, starting from the old configuration Γ_o and generate the new configuration Γ_n . This matrix is called the underlying matrix of the Markov chain. The probability to accept a trial move is described by $\text{acc}(o \rightarrow n)$ and thus we can write

$$\pi(o \rightarrow n) = \alpha(o \rightarrow n) \cdot \text{acc}(o \rightarrow n). \quad (2.40)$$

Rewriting the detailed balance condition leads to

$$\frac{\text{acc}(o \rightarrow n)}{\text{acc}(n \rightarrow o)} = \frac{\rho(\Gamma_n)}{\rho(\Gamma_o)} = \exp\{-\beta[U(\Gamma_n) - U(\Gamma_o)]\}, \quad (2.41)$$

which is referred to as the Metropolis algorithm.

To sum up the Metropolis algorithm in the canonical ensemble, we generate random configurations, compute the potential energy of the system and accept the new configuration according to Equation 2.41. That is, we generate a random number in the interval $(0,1)$ and accept the new configuration if the random number is less than $\exp\{-\beta[U(\Gamma_n) - U(\Gamma_o)]\}$ [6]. To improve the convergence of the sampling one chooses configuration that are close together in phase-space by allowing new configurations to be only in the vicinity of the old configuration.

2.4.2 Grand-canonical Monte-Carlo sampling

In the canonical ensemble we keep N, V, T constant, but sometimes we need information about the particle number or the density as function of an external condition. In particular, to study the vapor-liquid phase separation the GCMC ensemble is of great importance, since the density is the appropriate order parameter. For this purpose we translate the GC ensemble into the language of the MC simulation. In Metropolis MC measuring the Free Energy, the Entropy or the Gibbs Free Energy directly, is not possible. However, one can measure the difference of these quantities to a reference system.

For the sake of convenience we rewrite the canonical partition function by introducing scaled coordinates according to

$$\mathbf{r}_i = L\mathbf{s}_i, \quad (2.42)$$

and we obtain

$$Z(N, V, T) = \frac{V^N}{\Lambda^{3N} N!} \int_0^1 \dots \int_0^1 d\mathbf{s}^N \exp[-\beta U(\mathbf{s}^N)]. \quad (2.43)$$

If we now consider a system of N interacting particles in V and $M - N$ ideal gas particles in volume $V_0 - V$ we can write the partition function as

$$Z_G = \sum_{N=0}^M \frac{V^N (V_0 - V)^{M-N}}{\Lambda^{3M} N! (M - N)!} \int d\mathbf{s}^{M-N} \int d\mathbf{s}^N \exp[-\beta U(\mathbf{s}^N)]. \quad (2.44)$$

If we move one particle from $V_0 - V = V'$ to V we have to make sure that the underlying Markov chain is symmetric, and we end up at the acceptance criteria [46]

$$\text{acc}(N \rightarrow N + 1) = \frac{V(M - N)}{V'(N + 1)} \exp\{-\beta[U(\mathbf{s}^{N+1}) - U(\mathbf{s}^N)]\} \quad (2.45)$$

and

$$\text{acc}(N + 1 \rightarrow N) = \frac{V'(N + 1)}{V(M - N)} \exp\{-\beta[U(\mathbf{s}^N) - U(\mathbf{s}^{N+1})]\}. \quad (2.46)$$

If we assume that the second system is much larger, we can use $M \rightarrow \infty$, $V' \rightarrow \infty$ and $M/V' \rightarrow \rho$ and by using the expression of the chemical potential of an ideal gas

$$\mu = k_B T \ln \Lambda^3 \rho, \quad (2.47)$$

we can write [121]

$$\text{acc}(N \rightarrow N + 1) = \min \left[1, \frac{V}{\Lambda^3 (N + 1)} \exp\{\beta[\mu - U(N + 1) + U(N)]\} \right] \quad (2.48)$$

and

$$\text{acc}(N+1 \rightarrow N) = \min \left[1, \frac{\Lambda^{3N}}{V} \exp\{-\beta[\mu + U(N+1) - U(N)]\} \right]. \quad (2.49)$$

The relations in Equation 2.48 and Equation 2.49 can be used in an actual GCMC simulation to generate configurations with the variables T, V, μ , but with a fluctuating particle number.

2.4.3 Chemical potential

In the context of GCMC simulation, the chemical potential is an important quantity. Unfortunately, the chemical potential cannot be measured directly in a simulation, as it is the case for the Free Energy. In a simulation we thus measure the difference between the chemical potential of the system of interest and an ideal gas. There are several strategies to carry-out such a measurement. We are focusing on a widely used technique that we also used in this work, namely the Widom method [192].

The Free Energy of a statistical ensemble can be expressed as

$$F(N, V, T) = -k_B T \ln Z \quad (2.50)$$

$$= -k_B T \ln \left(\frac{V^N}{\Lambda^{dN} N!} \right) - k_B T \ln \left\{ \int ds^N \exp[U(\mathbf{s}^N)] \right\} \quad (2.51)$$

$$= F_{\text{id}} + F_{\text{ex}}. \quad (2.52)$$

By using the relation $\mu = \left(\frac{\partial F}{\partial N} \right)_{V, T}$ and by assuming a very large particle number N we can write

$$\mu = -k_B T \ln \left(\frac{Z_{N+1}}{Z_N} \right) \quad (2.53)$$

$$= -k_B T \ln \left(\frac{V/\Lambda^d}{N+1} \right) - k_B T \left\{ \frac{\int ds^{N+1} \exp[-\beta U(\mathbf{s}^{N+1})]}{\int ds^N \exp[-\beta U(\mathbf{s}^N)]} \right\} \quad (2.54)$$

$$= \mu_{\text{id}} + \mu_{\text{ex}}, \quad (2.55)$$

where in the above equations d is the dimension of the system. Now, it is possible to measure μ_{ex} by a regular Metropolis MC sampling. In practice, one generates a random particle which is inserted in the configuration and then computes the Boltzmann factor of both configurations. By averaging this value over a regular canonical MC simulation one obtains

$$\mu_{\text{ex}} = \left\langle \frac{1}{N} \exp\{-\beta[U(\mathbf{s}^{N+1}) - U(\mathbf{s}^N)]\} \right\rangle. \quad (2.56)$$

2.4.4 Advanced Monte-Carlo techniques

In many systems a regular Metropolis sampling scheme is not sufficient [44]. If we want, e. g., compare the free energy between two states or if the equilibration of a system is difficult due to large free energy barriers separating different states one has to improve the standard Metropolis scheme. The general idea of most techniques to overcome this problem and to improve the sampling is to change the regular Boltzmann probability to a sampling probability that is more suited to the concrete problem. In this section we give a short overview of techniques that can be used to overcome the free energy barriers in order to compute the phase separation in a first-order phase transition.

Indeed, during the past years a variety of sophisticated methods were developed to determine phase transitions in fluids via MC computer simulations. In particular, simulations near the critical point can be cumbersome, mainly for two reasons. First, below the critical point the two phases are typically separated by a significant free energy barrier. Second, particularly in systems with strongly directional and/or long-range interactions, very long simulation times are required to obtain reliable results.

2.4.4.1 Umbrella sampling

In order to introduce the sampling technique we start by noting that in general the free energy difference (ΔF) of two systems, 0 and 1, with partition functions Z_0 and Z_1 , can be written as

$$\Delta F = -k_B T \ln(Z_1/Z_0) = -k_B T \ln \left(\frac{\int d\Gamma \exp[-\beta U_1]}{\int d\Gamma \exp[-\beta U_0]} \right). \quad (2.57)$$

We assume that we sample system 1 by regular Metropolis MC and we are able to compute the potential energy of system 0 in the same configuration Γ and to determine the energy difference of both systems, $\Delta U = U_1(\Gamma) - U_0(\Gamma)$. In this way we can build a probability density of the energy difference

$$p_1(\Delta U) = \frac{\int d\Gamma \exp[-\beta U_1] \delta(U_1 - U_0 - \Delta U)}{\int d\Gamma \exp[-\beta U_1]} \quad (2.58)$$

$$= \frac{q_0}{q_1} \exp[-\beta \Delta U] p_0(\Delta U), \quad (2.59)$$

with $q_{0,1} = \int d\Gamma \exp[-\beta U_{0,1}]$ and p_0 is the probability density to find the energy difference ΔU by sampling over system 0. Now, we can write the free energy difference of system 0 and 1 by

$$\ln p_1(\Delta U) = \beta(\Delta F - \Delta U) + \ln p_0(\Delta U) \quad (2.60)$$

and by integrating this equation over ΔU we obtain

$$\int d\Delta U p_1(\Delta U) = \exp(\beta \Delta F) \int d\Delta U p_0(\Delta U) \exp(-\beta \Delta U) \quad (2.61)$$

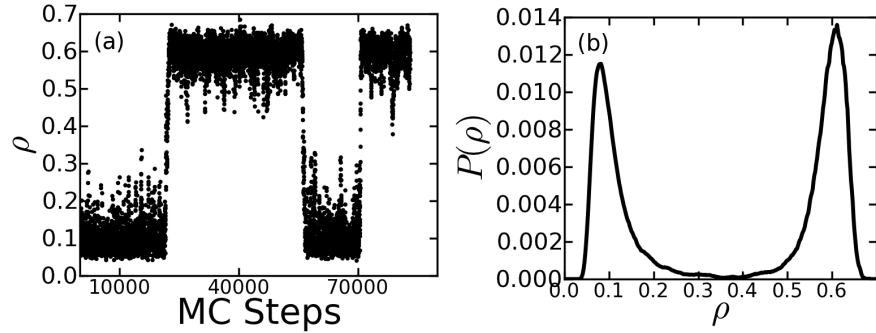


Figure 7: In (a) we show the current particle density during a GCMC simulation of Lennard-Jones particles in two dimensions close below the critical temperature. In (b) we show the density histogram recorded in (a).

and thus

$$\exp(-\beta\Delta F) = \langle \exp(-\beta\Delta U) \rangle_0. \quad (2.62)$$

In most practical cases large contributions to the average $\langle \exp(-\beta\Delta U) \rangle_0$ are from configurations with a small probability density p_0 at this configuration. To improve the sampling and the estimate of the free energy difference of system 0 and 1 the part of the configurational space where p_0 and p_1 are significantly different from zero must be sampled. For this purpose one introduces a weight-function $\eta(\Gamma)$ [165, 166] that changes the regular Boltzmann probabilities and the average becomes

$$\langle \exp(-\beta\Delta U) \rangle_0 = \frac{\int d\Gamma \eta(\Gamma) \exp[-\beta U_1(\Gamma)] / \eta(\Gamma)}{\int d\Gamma \eta(\Gamma) \exp[-\beta U_0(\Gamma)] / \eta(\Gamma)} \quad (2.63)$$

$$= \frac{\langle \exp(-\beta U_1) / \eta \rangle_\eta}{\langle \exp(-\beta U_0) / \eta \rangle_\eta}. \quad (2.64)$$

In order to sample regions of the configuration space where the averages of both systems are non zero, an appropriate weight-function must be chosen. In practice it is often better to perform several umbrella samplings in partially overlapping windows. An overview of how to choose the weight-function can be found in [46]. In the following part we introduce some state-of-the-art techniques to build a suitable weight-function and to overcome the free energy barrier, focusing on the case of a first-order phase transition.

2.4.4.2 Multicanonical Monte-Carlo

More recent techniques to determine a phase coexistence foot on GC ensemble. We already introduced the acceptance criteria of the GC sampling, see Equation 2.45 and Equation 2.46.

The GCMC simulation behaves in the vicinity of a gas-liquid phase separation as illustrated in Figure 7. The density ρ fluctuates from

the vapor (low-density) state to the fluid (high-density) state, and back. This situation is shown in Figure 7(a), where we recorded the current density during a simulation of regular Lennard-Jones particles in two dimensions close to the critical temperature. One observes clearly two distinct phases described by the order parameter ρ . If one accumulates at the same time a histogram of the densities reached during a GC simulation run one obtains Figure 7(b), where each peak corresponds to one density. Close to a gas-liquid phase-separation this double peaked structure of $P(\rho)$ is typical. If both peaks have equal probability, i. e., equal area under the peaks, one has found the coexistence parameters [194]. By successively tuning T and μ to this point one can reach the coexistence in a GCMC simulation.

The probability that the simulation passed from one phase to the other through the inter-phase region is very low. One strategy to overcome this barrier in the sampling is the so-called Multicanonical MC technique [16, 17, 63]. The idea of this sampling method is to pre-weight the simulation and to enhance the sampling of the inter-phase region in the configuration space. The probability density distribution to find N particles in a GCMC simulations is

$$p(N|T, V, \mu) = \frac{1}{Z_{GC}} \prod_{i=1}^N \left\{ \int dr_i \right\} \exp[-\beta H], \quad (2.65)$$

with the Hamiltonian $H = U(\Gamma) - \mu N$. If we replace H by an effective Hamiltonian $\tilde{H} = H + \eta(N)$, where $\eta(N)$ is the weight-function, we obtain

$$\tilde{p}(N) = \frac{1}{Z_{GC}} \prod_{i=1}^N \left\{ \int dr_i \right\} \exp[-\beta \tilde{H}]. \quad (2.66)$$

Now, we assume that we are able to choose the weight-function according to $\eta(N) = \ln p(N)$ and by inserting this condition in the above equation we see that this choice leads to $\tilde{p}(N) = \text{constant}, \forall N$. Clearly, we do not obey the Boltzmann statistics by using the modified Hamiltonian. Thus, we have to unfold the weight-function from the results to receive the physical relevant results by $p(N) = e^{\eta(N)} \tilde{p}(N)$. The GC acceptance rules read then

$$\begin{aligned} \text{acc}(N \rightarrow N+1) = \\ \min \left[1, \frac{V}{\Lambda^3(N+1)} \exp(\beta[\mu - \Delta U_{N \rightarrow N+1}]) + \eta(N) \right], \end{aligned} \quad (2.67)$$

and

$$\begin{aligned} \text{acc}(N \rightarrow N-1) = \\ \min \left[1, \frac{\Lambda^3 N}{V} \exp(-\beta[\mu + \Delta U_{N-1 \rightarrow N}]) + \eta(N) \right]. \end{aligned} \quad (2.68)$$

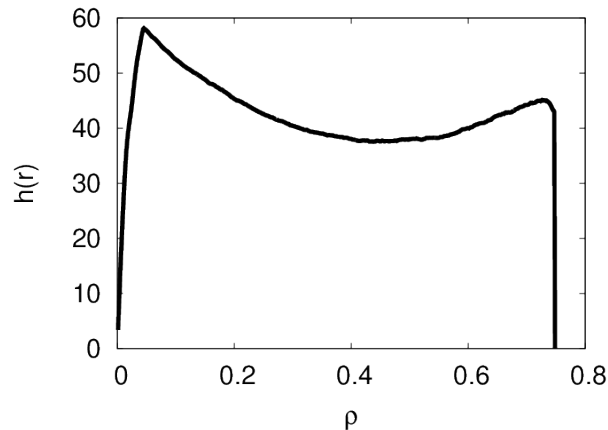


Figure 8: We plot the SU weight-function. The system we show are Stockmayer particles confined to two dimensions close below the critical temperature.

The weight-function we are assuming is however the logarithm of the probability distribution we are trying to find. To obtain a suitable weight-function is a difficult task. One approach is, e. g., to start with an unweighted GC simulation and to use the resulting density probability $p_0(N)$ as a weight-function, $\eta(n) = p_0(N)$, for a subsequent multicanonical simulation, obtaining the probability density $p_1(N)$. By iteratively improving the weight-function through subsequent multicanonical samplings one can obtain a flat histogram of all states. The following two sections introduce two state-of-the-art simulation techniques that are designed to obtain such a weight-function in a very efficient way.

2.4.4.3 Successive Umbrella sampling

This sampling methods allows to generate a flat histogram of all states close to a first-order phase transition without prior knowledge of a weight-function. In Section 2.4.4.1 we have already introduced the idea of using a weight-function in sampling different windows of a Density of States (DOS) but we have not explained how to obtain such a weight-function. The general idea of SU sampling is to divide the DOS into small windows, which are sampled subsequently and an estimate of the weight-function is determined on the fly. In the scheme proposed by Virnau *et al.* [176] one subdivides the density range into intervals which are simulated one after the other. These windows contain in the limit case only two particles. The simulation is allowed to insert or delete only one particle and thus the window contains either $(k-1)$ or k particles. At the same time one records a histogram for both sides of the k -th window, $H_{k_{\text{left}}}$ and $H_{k_{\text{right}}}$, which records how often the system has visited the state with k or $(k-1)$ states, respectively. All attempts to leave the window are not counted

in the histogram. The probability distribution of the whole density range can be obtained from the histograms by [176, 177]

$$\frac{P[N]}{P[0]} = \frac{H_{1_{\text{right}}}}{H_{1_{\text{left}}}} \cdots \frac{H_{N_{\text{right}}}}{H_{N_{\text{left}}}}, \quad (2.69)$$

where $k = 1, \dots, N$. The simulation is thus a regular GC sampling, whereas the particle number is kept in a very small window of only two particles.

The method becomes particularly efficient if it is combined with the multicanonical approach we described in the previous Section 2.4.4.2. To obtain the weight-function that is needed to make the sampling more efficient one can construct a weight-function that can be extrapolated from one already sampled window to the next window by using $\eta(n) = \ln P[n]$. The first window containing only 0, 1 particles is usually unweighted. Then the corresponding weight-function is extrapolated linearly in the second window and then quadratically into all next windows. This choice turned out to be advantageous since the weight function is curved [176].

In our simulations we use windows that contain two particles, and we perform $1 - 2 \cdot 10^6$ insertion/deletion tries. As a (qualitative) criterion for the convergence of the SU procedure, we increased the number of insertion/deletion tries and checked whether the accuracy is improved. If this is not the case, we consider the simulation as converged. In Figure 8 we show a weight-function obtained from a SU sampling of a two-dimensional Stockmayer system close below the critical temperatures. The peaks revealing the coexisting densities are clearly present. In comparison to Figure 9 we remark that the peaks are somehow more narrow, especially at the low density phase.

2.4.4.4 Wang-Landau sampling

The WL sampling method is a recent simulation technique that is used in a wide range of systems successfully in the case of phase transitions and complex free energy landscapes. It was originally developed for lattice systems [181] but later generalized to off-lattice systems, like simple fluids [149, 197], complex fluids (consisting of charged soft-spheres or dipolar particles) [49] or even proteins [202]. Some refinements to the sampling technique were also made in order to improve the performance [196]. Especially in the case of systems made of particles that possess long-range interactions the WL sampling proved to be very useful [49, 7, 88].

The method is derived from the idea that any thermodynamic information can be calculated from the DOS, $g(E)$, where E is the internal energy of the system. In order to obtain $g(E)$ in a WL sampling, one uses a modified MC scheme. Trial configurations of the system are generated randomly and accepted with the probability [181]

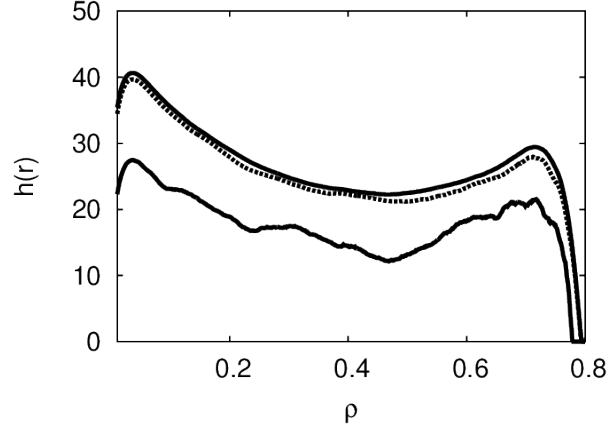


Figure 9: We plot the WL weight-function for three iteration steps, accordingly to the procedure described in the text. The system we show are Stockmayer particles confined to two dimensions close below the critical temperature.

$$p_{\text{acc}} = \min \left[\frac{g(E_1)}{g(E_2)}, 1 \right]. \quad (2.70)$$

In Equation 2.70, E_1 and E_2 are the internal energy of state 1 and 2, respectively. This equation is used instead of the standard Metropolis criterion in the regular MC sampling. To explore all possible states of the system we increase $g(E)$ each time the state with energy E is visited and thus the state becomes less likely to be visited again. In this way we generate a flat histogram of all possible states of the system. At the very beginning the DOS is unknown for all states and thus assumed to be equal for all energies, i. e., $g(E) = 1, \forall E$. During the simulation $g(E)$ is adapted by multiplying this function with a factor f , i. e., $g(E) \rightarrow g(E) \cdot f$, with $f > 1$, if the configuration with energy E was generated. We also record a histogram $h(N)$ of all visited states which is used to ensure that all states are visited with sufficient accuracy. The simulation runs until $h(N)$ is sufficiently flat. Once the criterion for flatness of $h(N)$ is fulfilled, $h(N)$ is set to zero for all N , the factor f is scaled down and we start again to record the histogram and to multiply $g(E)$ with the smaller factor f . By iteratively going through these steps the factor f approaches 1 ($f \rightarrow 1$) and $g(E)$ converges against its true value. At this point it is important to note that the detailed balance condition [6] is violated, since we change the acceptance criterion in each simulation step. However, since $g(E)$ finally converges against its true value, the condition of detailed balance is satisfied with an accuracy of $\ln(f)$.

In this work we aim at studying the condensation phase transition of dipolar systems. Due to the very long equilibration times in dipolar systems caused by the long-range interactions, sampling of the whole DOS is impractical, even for systems that contain “only” a

few hundred particles. This problem can be circumvented by fixing certain GC variables during the WL sampling. First, we write down the GC acceptance criteria with the additional weight-function $\eta(N)$ introduced in Section 2.4.4.2

$$p_{\text{acc}}(N \rightarrow N + 1) = \min \left[1, \frac{V}{\Lambda^3(N+1)} \exp(\beta[\tilde{\mu} - \Delta U_{N \rightarrow N+1}]) + \eta(N) \right], \quad (2.71)$$

and

$$p_{\text{acc}}(N \rightarrow N - 1) = \min \left[1, \frac{\Lambda^3 N}{V} \exp(-\beta[\tilde{\mu} + \Delta U_{N-1 \rightarrow N}]) + \eta(N) \right], \quad (2.72)$$

where $\tilde{\mu}$ is the chemical potential (see Equation 2.67 and Equation 2.68). In order to fix certain thermodynamic variables we replace Equation 2.70 by Equation 2.71 and Equation 2.72. In this way we ensure that the temperature and the chemical potential is fixed during a simulation. The DOS can then be modified through the weight-function $\eta(N)$. In this way we generate not totally random configurations, but configurations that are close to the desired temperature and chemical potential. This choice accelerates our simulation near the critical temperature significantly. In practice, we follow the approach of Binder *et al.* [177]. The initial guess for the weight-function in Equation 2.71 and Equation 2.72 is $\eta(N) = 0$. Each time a state is visited, we increase the weight-function by $\Delta\eta$ where $\Delta\eta \sim 10^{-4} - 10^{-5}$. At the same time we record a histogram $h(N)$ of all possible particle numbers. As soon as $|h(N) - \langle h(N) \rangle| < \epsilon \langle h(N) \rangle \forall N$, with $\epsilon \sim 0.5 - 0.1$, the histogram is sufficiently flat and we reduce $\Delta\eta$ to $\Delta\eta/10$. In a typical simulation run we iterate three or four steps to obtain the DOS. In Figure 9 we show the WL weight-function after three iteration steps for a system of two-dimensional Stockmayer particles close below the critical temperature. The lowest continuous line shows the first weigh-function, which is clearly not smooth. After two iterations (middle dashed line) and three iterations (topmost continuous line) we obtain a smooth weight-function and can identify both phases by the peaks at low density, $\rho \approx 0.01$ and at the high density, $\rho \approx 0.75$. We note that the performance of the technique strongly depends on a reasonable choice of the parameters ϵ and $\Delta\eta$. If $\Delta\eta$ is chosen too small the simulation will not converge in reasonable times; if it is too large the simulation will not sample all possible states and thus not map the real DOS. The parameter ϵ strongly depends on the system considered and controls the convergence of the algorithm.

2.4.4.5 Histogram reweighting

Histogram Reweighting (HR) foots on the idea that histograms of observables that are obtained at one set of parameters during a MC

sampling can give estimates of the histogram of the same observable at different values of the parameters [194]. Since we are dealing with GCMC simulations a natural choice of these parameters is, e. g., the inverse temperature $\beta = 1/k_B T$ and the chemical potential μ . The joint probability density at $\beta = \beta_0$ and $\mu = \mu_0$ in the GC ensemble is given by

$$p(N, U|\beta_0, \mu_0) = \frac{1}{Z_0} \prod_{i=1}^N \left\{ \int dr_i \right\} \delta(U - U(\{r_i\})) e^{-\beta_0 H_0}, \quad (2.73)$$

where $H_0 = U(\{r\}) + \mu_0 N$. The estimate at a new set of parameters β_1, μ_1 can now be obtained by reweighting the probability density according to [42, 43]

$$p(N, U|\beta_1, \mu_1) = \frac{Z_1}{Z_0} \exp\{-[\beta_1(U - N\mu_1) - \beta_0(U - N\mu_0)]\} p(N, U|\beta_0, \mu_0). \quad (2.74)$$

The factor Z_1/Z_0 emerging in Equation 2.74 is simply absorbed into the normalization of the probability density. In this way one can extend the information of one simulation obtained at one set of parameters to another set without running the simulation again. Unfortunately the overlapping region of the configuration space at both set of parameters is in general very poor. Hence, the statistics of the reweighted histogram may be bad. In practice one uses only a set of parameters that correspond to regions in the configuration space where both histograms overlap significantly.

In the case of a phase transition we showed in Section 2.4.4.2 that below the critical temperature one obtains a double-peaked histogram of the order parameter. The HR technique can serve in this context to extract the parameter set that corresponds to an equal probability of both phases and thus to extract the equilibrium parameters of the coexistence of both phases. This is done by successively tuning, e. g., the chemical potential μ until equal areas under both peaks is achieved by reweighting the histogram.

2.4.5 *Discontinuous Molecular Dynamics simulations*

The MC techniques we discussed so far give us no information about any time dependent quantities. Thus, we are turning towards computer simulations that are able to study dynamic properties of many particle systems. Basically, there are two approaches in MD simulations. The first is to solve Newton's equations of motion in constant time steps. We can compute the forces on each particle at this time, evolve the system according to the solution of the equation of motion and

repeat this step. To solve the equations we need continuous potentials. Examples for such potentials are the Soft-Sphere potential or the Lennard-Jones potential. The basic limitation of continuous MD is the time-step. The change of the potential over the time-step needs to be small. If this is not the case unexpected numerical errors can emerge. At the same time the time-step should not be too small in order to reach equilibrium in reasonable time.

These problems do not exist in DMD simulations, which was the first method suggested to study ensembles dynamically, even before continuous MD [4, 5]. The underlying idea is to evolve the system from one event to the next, where events describe basically collisions of particles. In order to apply this technique the potentials must be constant between the collisions. Due to the use of discontinuous potentials the method is called Discontinuous MD.

2.4.5.1 Collision dynamics

To introduce the DMD simulation technique we start with simple Hard-Spheres defined by

$$U_{\text{HS}} = \begin{cases} 0 & \text{if } r > \sigma \\ \infty & \text{if } r \leq \sigma \end{cases}, \quad (2.75)$$

where σ is the particle diameter and r the distance between two particles. We assume two particles at position \mathbf{r}_i and \mathbf{r}_j with velocities \mathbf{v}_i and \mathbf{v}_j , respectively. We use the relative distance $\mathbf{r} = \mathbf{r}_i - \mathbf{r}_j$ and velocity $\mathbf{v} = \mathbf{v}_i - \mathbf{v}_j$. These two particles will collide if the distance is equal to the particle diameter σ . The time of this event is simply given by

$$|\mathbf{r} + \tau\mathbf{v}| = \sigma, \quad (2.76)$$

and the solution is

$$\tau = \frac{-b - \sqrt{b^2 - v^2(r^2 - \sigma^2)}}{v^2} \quad (2.77)$$

with $b = \mathbf{r} \cdot \mathbf{v}$. The square root has to be positive, which corresponds to events in the future and b has to be negative, meaning the particles are moving towards each other. The collision changes the velocities accordingly to

$$\Delta\mathbf{v}_i = -\Delta\mathbf{v}_j = -\frac{b}{\sigma^2} \cdot \mathbf{r}. \quad (2.78)$$

The collision has been solved and the two particles have new velocities. The above equations can be used to compute the dynamics of the Hard-Sphere system successively. A basic algorithm works as follows:

1. Initialize simulation
2. Compute all collision times according to Equation 2.77
3. Solve the collision with the smallest collision time τ , i. e., the next event using Equation 2.78
4. Evolve all other particles ballistically with the time step τ
5. Compute the new collision time associated to both particles of step 3
6. Go to step 3

This method can also be used to simulate more complicated interactions. To introduce the idea we discuss shortly how to use DMD for a square-well potential [151]. The square-well potential is defined as follows

$$U_{\text{SW}} = \begin{cases} \infty & \text{if } r \leq \sigma \\ -\epsilon & \text{if } \sigma_1 < r \leq \sigma_2 \\ 0 & \text{if } r > \sigma_2 \end{cases} , \quad (2.79)$$

where ϵ is the square-well depth and $\sigma_2 - \sigma_1$ the width. In this case the possible events consist of several cases:

- Collision between the hard cores
- Particles entering or leaving the square-well
- Bouncing of the particles at the square-well

We introduce the hard-core diameter σ_c and square-well diameter $\sigma_w = \sigma_2 - \sigma_1$. The collision time can be determined by [134]

$$\tau = \frac{-b + s\sqrt{b^2 - v^2(r^2 - \sigma^2)}}{v^2} \quad (2.80)$$

where the parameter s has to be chosen accordingly to the event type. The hard core collision is described by $s = -1$ and $\sigma = \sigma_c$. If the event is within the square-well and the particles are departing there can be either dissociation or bounce at the square-well border. These cases are described by $s = 1$ and $\sigma = \sigma_w$. In the case that the distance between both particles is larger than σ_w but the particles are approaching each other, we choose $s = -1$ and $\sigma = \sigma_w$.

The velocities are computed according to [134]

$$\Delta \mathbf{v}_i = -\Delta \mathbf{v}_j = \Phi \mathbf{r}, \quad (2.81)$$

with

$$\Phi = \frac{-b + s\sqrt{b^2 - 4r^2\Delta u/m}}{2r^2}, \quad (2.82)$$

where Δu is the change in the potential energy at the collision, i. e., dissociation or capture of particles by the square-well potential and m is the mass of the particles. The parameter s is chosen according to the events above and $\Delta u = 0$ for a hard-core collision and $\Delta u = -w$ for a capture and $+w$ for a dissociation.

2.4.5.2 DMD in the canonical ensemble

In classical statistical mechanics the probability to find an ensemble at a energy state at constant temperature is given by the Maxwell-Boltzman distribution

$$P(\mathbf{p}) = \left(\frac{\beta}{2\pi m}\right)^{3/2} \exp[-\beta p^2/(2m)], \quad (2.83)$$

where p is the inertia and m the particle mass. We need a further relation that connects the state of an ensemble to the thermodynamics, namely the equipartition theorem. The average kinetic energy per degree of freedom is given by

$$\left\langle \frac{1}{2} m v_\alpha^2 \right\rangle = \frac{1}{2} k_B T, \quad (2.84)$$

where v_α is the α -th component of the velocity. This relation allows us to connect the temperature of a system directly to the simulation. There are several ways to control the kinetic energy and thus the temperature during a simulation. One method, proposed by Andersen [9], simulates directly a heat bath to control the temperature. Stochastic collisions with randomly selected particles simulate the heat bath. These random collisions can be regarded as MC steps that move the system from one constant energy shell to another according to the Boltzman distribution. In practice we choose one random particle and set its velocity according to the Maxwell-Boltzman distribution, Equation 2.83, at the desired temperature. The coupling of the thermostat can be adjusted by the frequency of the collisions.

Beside the Andersen thermostat, that is used in our simulations, there are other ways to control the temperature. One foots on the use of an extended Lagrangian. In the so-called Nosé-Hoover thermostat, further variables are used to solve the Newton equations of motion deterministically and to adjust the velocity in each time-step. Velocity rescaling is a further and very popular technique to control the temperature of a simulation.

2.4.6 Further simulation techniques

The introduced simulation techniques, MC and DMD, are focusing only on the properties of the particle model. In real systems colloidal particles are, however, dispersed in a solvent that might have an influence on the aggregation and dynamic behavior of such colloids. To take these effects into account several simulation techniques have been developed that include solvent effects like friction, Brownian motion, and hydrodynamic interactions.

The Dissipative Particle Dynamics (DPD) method adds to conservative forces that are used in MD and DMD a friction force due to the solvent and a random force, which emerges from the Brownian motion of the solvent particles. Consequently, the total energy is not conserved but the momentum is conserved locally. Each time a random force is assigned to a particle, the opposite random force is assigned to an interacting counterpart, resulting in a local momentum conservation. In Brownian Dynamics (BD) where the same forces are applied, on the contrary, there is no such constrain and the local momentum is not necessarily conserved. In the long run, however, the random force cancels itself out and one obtains physically correct results. Through the coupling of two interacting particles the DPD method can be used to model hydrodynamic interactions [46]. But also the BD technique can be extended to take hydrodynamic interactions into account. One route is for example to include the Rotne-Prager tensor as the diffusion tensor in the equation of motion of a BD simulation [39]. A detailed derivation of these techniques goes beyond the scope of this work and can be found in [46, 39]. Further simulation techniques that incorporate hydrodynamic interactions on a mesoscale level are, e. g., Lattice Boltzmann, Stokesian Dynamics and Multi-particle collision dynamics.

In this work we are not taking any of these effects into account. The MC technique is suitable to study equilibrium properties where hydrodynamic effects and the influence of the solvent are expected to be rather small. Further, advanced MC techniques to overcome the free-energy barrier between the liquid and the vapor phase are much more efficient to determine the phase-diagram. The DMD technique, as already stated, is a very efficient simulation technique. Computer simulations that incorporate solvent and hydrodynamic effects are significantly slower. We are aiming to map a phase-diagram in a broad range of densities and temperatures and we are thus employing this fast alternative.

However, we have controlled some effects of the solvent. As we will discuss in Section 3.4, we have studied a two-dimensional system of dipoles exposed to a rotating external field. Due to the rotation of the particles hydrodynamics may influence the phase behavior. Sebastian Jäger studied these effects by employing BD simulations including

hydrodynamic interactions by using the Rotne-Prager tensor and the same particle model as in our MC simulations. The additional forces had only little influence on the phase behavior. Further, we studied the dynamics of the networks discussed in Chapter 5 including the effect of the solvent through employing BD simulations, again carried out by Sebastian Jäger with essentially the same model as in our MC simulations. The dynamics did not display any significant change compared to regular MD simulations, compare the corresponding discussion in Chapter 5. Therefore, we will in the rest of this work mainly focus on the properties of the colloids and neglect solvent and hydrodynamic effects.

2.4.7 Long-range interactions

In this work we use different particle models suited to each of the problem we are intended to investigate. In general, particle interactions in computer simulations can be divided into two parts, short-range and long-range interactions. Examples for short range interaction are, e. g., the Soft-Sphere (SS) potential or the LJ potential (Equation 2.1). These examples decay with the inter-particle distance greater than $U \propto r^{-n}$ with $n > 6$ which defines them as short-range. Such interactions can be truncated without losing important parts of the interaction and thus it is sufficient to compute the interactions in one simulation box.

Particle interactions that decay with $U \propto r^{-n}$ with $n < 6$ are usually referred to as long-range interactions. Since we use a finite simulation box with a finite number of model particles the long-range interactions need a special treatment. They cannot be truncated since this would cut out important parts of the interaction.

2.4.7.1 Ewald summation for Coulomb system

In this work we use to so-called Ewald summation technique to treat our long-range interactions. We will start to introduce the technique by treating a system of point charges, the extension to point dipole systems is straightforward. This part follows closely the derivation in [144].

Let us assume we have N charged particles, q_i , in a finite volume $V = s_x, s_y, s_z$. As a whole the system is uncharged $\sum_{i=1}^N q_i = 0$. The potential energy of the N particle system is

$$U_c = \frac{1}{2} \sum_{i=1}^N q_i \Phi(\mathbf{r}_i), \quad (2.85)$$

where $\Phi(\mathbf{r}_i)$ is the electrostatic potential of particle i . Now, if we assume that the central simulation cell is surrounded by identical replicas in all three dimensions the potential can be written as

$$\Phi(\mathbf{r}_i) = \sum'_{\{\mathbf{n}\}} \sum_{j=1}^N \frac{q_j}{|\mathbf{r}_{ij} + \mathbf{n}|}, \quad (2.86)$$

with $\mathbf{r}_{ij} = \mathbf{r}_i - \mathbf{r}_j$ and $\{\mathbf{n}\}$ is the set of lattice vectors generating the replica of the central simulation cell with $\mathbf{n} = (n_x s_x, n_y s_y, n_z s_z)$ and $n_{x,y,z} \in \mathbb{Z}$. We omit the term $i = j$ in the central simulation box $\mathbf{n} = 0$, which is indicated by the prime in the first summation. The Poisson equation describes the relation between a charge density and the potential produced by

$$\Phi(\mathbf{r}_i) = \int d\mathbf{r}' \frac{\rho_i(\mathbf{r}_i)}{|\mathbf{r}_i - \mathbf{r}'|}. \quad (2.87)$$

We also assume that the charges can be described as simple delta functions and thus the density as a sum of delta functions. Since the potential decays according to $\sim 1/r$ the above sum converges slowly and is practically not feasible in real computer simulations. The Ewald summation technique solves this problem by rewriting the δ -like densities as a sum of three contributions. This approach starts by superposing each δ charge a cloud of charge with the opposite sign. One usually chooses a Gaussian distribution for these clouds

$$\rho_{j,\mathbf{n}}(\mathbf{r}') = -q_j \left(\frac{\alpha}{\sqrt{\pi}} \right)^3 \exp[-\alpha^2(\mathbf{r}' - \mathbf{r}_j + \mathbf{n})^2]. \quad (2.88)$$

In the above equation α controls the width of the Gaussian distribution and thus the convergence of the corresponding summation over all distributions. The whole charge distribution is then comprised of the δ like point charges which are screened by oppositely charged Gaussian distributions

$$\rho_i^{(1)}(\mathbf{r}') = \sum'_{\{\mathbf{n}\}} \sum_{j=1}^N [q_j \delta(\mathbf{r}' - \mathbf{r}_j + \mathbf{n}) + \rho_{j,\mathbf{n}}(\mathbf{r}')]. \quad (2.89)$$

It can be shown, see [144], that the potential is then given by

$$\Phi^{(1)}(\mathbf{r}_j) = \sum'_{\{\mathbf{n}\}} \sum_{j=1}^N q_j \frac{\text{erfc}(\alpha|\mathbf{r}_{ij} + \mathbf{n}|)}{|\mathbf{r}_{ij} + \mathbf{n}|} \quad (2.90)$$

with the complementary error function erfc . Since we artificially added Gaussian charge clouds we need to subtract this contribution in order to obtain the original charge density

$$\rho_i(\mathbf{r}_{ij}) - \rho_i^{(1)}(\mathbf{r}') = - \sum'_{\{\mathbf{n}\}} \sum_{j=1}^N \rho_{j,\mathbf{n}}(\mathbf{r}'). \quad (2.91)$$

This sum is split into two contributions for the sake of convenience

$$\rho^{(2)} = -\sum'_{\{\mathbf{n}\}} \sum_{j=1}^N \rho_{j,\mathbf{n}}(\mathbf{r}') \quad (2.92)$$

$$= \sum'_{\{\mathbf{n}\}} \sum_{j=1}^N q_j \left(\frac{\alpha}{\sqrt{\pi}} \right)^3 \exp[-\alpha^2(\mathbf{r}' - \mathbf{r}_j + \mathbf{n})^2] \quad (2.93)$$

and in

$$\rho^{(3)}(\mathbf{r}') = \rho_{i,0}(\mathbf{r}') \quad (2.94)$$

$$= -q_i \left(\frac{\alpha}{\sqrt{\pi}} \right)^3 \exp[-\alpha^2(\mathbf{r}' - \mathbf{r}_i)^2]. \quad (2.95)$$

In Equation 2.93 we have a sum of Gaussian charges that are periodically distributed in space. As a consequence it is more practical to carry out the summation in the reciprocal space, that is spanned by $\mathbf{k} = (2\pi m_x/n_x, 2\pi m_y/n_y, 2\pi m_z/n_z)$ with $m_{x,y,z} \in \mathbb{Z}$. The resulting potential is finally given by

$$\Phi^{(2)}(\mathbf{r}_i) = \frac{4\pi}{V} \sum_{\mathbf{k} \neq 0} \sum_{j=1}^N \frac{q_j}{k^2} \exp\left[-\frac{k^2}{4\alpha^2}\right] \exp[-i\mathbf{k}\mathbf{r}_{ij}] + \Phi_\infty. \quad (2.96)$$

The last term Φ_∞ corresponds to the term $\mathbf{k} = 0$ and is the long range contribution. This term depends on the assumed boundary conditions of the actual simulation. If one assumes that the simulation cell and all of its replicas are surrounded by a dielectric continuum with dielectric constant ϵ this contribution is given by

$$\Phi_\infty(\mathbf{r}_i) = \frac{4\pi}{V} \frac{\mathbf{r}_i \mathbf{M}}{2\epsilon + 1}, \quad (2.97)$$

where $\mathbf{M} = \sum_{j=1}^N q_j \mathbf{r}_j$. In our simulations we usually assume a simulation surrounded by metal and we obtain thus $\epsilon = \infty$ and $\Phi_\infty = 0$. The term in Equation 2.95 corresponds to the unphysical self-interaction of the charges in the central simulation box with themselves. This contribution is given by

$$\Phi^{(3)}(\mathbf{r}_i) = -q_i \frac{2\alpha}{\sqrt{\pi}}. \quad (2.98)$$

All contributions to the potential are now solved and we can write down the expression for the potential energy of the N-particle system. We insert the expressions in Equation 2.85 and obtain for the contribution from real space

$$U_{CF} = \frac{1}{2} \sum_{i=1}^N \sum_{j=1}^N \sum'_{\{\mathbf{n}\}} q_i q_j \frac{\text{erfc}(\alpha|\mathbf{r}_{ij} + \mathbf{n}|)}{|\mathbf{r}_{ij} + \mathbf{n}|}, \quad (2.99)$$

the contribution from Fourier space

$$U_{\text{CF}} = \frac{1}{2} \sum_{i=1}^N \sum_{j=1}^N \sum_{\mathbf{k} \neq 0} \frac{q_i q_j}{k^2} \exp\left[-\frac{k^2}{4\alpha^2}\right] \exp[-i\mathbf{k} \cdot \mathbf{r}], \quad (2.100)$$

from the long-range contribution

$$U_{\text{CLR}} = \frac{2\pi}{V} \frac{1}{2\epsilon + 1} M^2, \quad (2.101)$$

and from the self-contribution

$$U_{\text{CS}} = -\frac{\alpha}{\sqrt{\pi}} \sum_{i=1}^N q_i^2. \quad (2.102)$$

In practical use of the Ewald summation technique in an actual computer simulation some points have to be considered. The parameter α in the above equations controls the convergence of the real space contribution, Equation 2.99. Usually, this parameter is chosen such that in Equation 2.99 only the central simulation box, i. e., $\mathbf{n} = 0$ has to be taken into account. Typical values for α are $\alpha \cdot L \sim 5 - 7$, which corresponds to a cut-off of this contribution at half the length of the central simulation cell, L . The Fourier contribution is evaluated until to a maximum wave vector k_{max} . This value depends on the choice of α through the Gaussian damping function $\exp[-k^2/4\alpha^2]$. Consequently, k_{max} can not be chosen independently from α . A fast convergence in the real space leads to a slow convergence in the Fourier space and vice versa. Typical values for k_{max} are $k_{\text{max}} \sim 30 - 70$. Another important point for the practical implementation is the fact that the Fourier part can be rewritten as

$$U_{\text{CF}} = \frac{2\pi}{V} \sum_{\mathbf{k} \neq 0} \frac{1}{k^2} \exp\left[-\frac{k^2}{4\alpha}\right] \tilde{a}(\mathbf{k}) \tilde{a}^*(\mathbf{k}), \quad (2.103)$$

where

$$\tilde{a}(\mathbf{k}) = \sum_{i=1}^N q_i \exp[-i\mathbf{k} \cdot \mathbf{r}_i] \quad (2.104)$$

and $\tilde{a}^*(\mathbf{k})$ is the complex conjugate of $\tilde{a}(\mathbf{k})$. This re-formulation allows us to evaluate this sum in $2N$ steps instead of N^2 steps in the original formulation and saves computation time.

2.4.7.2 Ewald summation for dipoles

Since in this work we are interested in the behavior of dipolar systems we need to formulate the Ewald summation for dipoles. We start by expressing the regular dipole-dipole interaction

$$u_{\text{DD}}(\mathbf{r}_{ij}, \boldsymbol{\mu}_i, \boldsymbol{\mu}_j) = \frac{\boldsymbol{\mu}_i \cdot \boldsymbol{\mu}_j}{r_{ij}^3} - 3 \frac{(\boldsymbol{\mu}_i \cdot \mathbf{r}_{ij})(\boldsymbol{\mu}_j \cdot \mathbf{r}_{ij})}{r_{ij}^5}. \quad (2.105)$$

This equation can be rewritten as

$$u_{DD}(\mathbf{r}_{ij}, \boldsymbol{\mu}_i, \boldsymbol{\mu}_j) = (\boldsymbol{\mu}_i \nabla_i)(\boldsymbol{\mu}_j \nabla_j) \Psi(r_{ij}), \quad (2.106)$$

where $\Psi(r_{ij}) = 1/r_{ij}$. If we compare this equation with the Coulomb interaction we see that by replacing $q_i \rightarrow (\boldsymbol{\mu}_i \nabla_i)$ and $q_j \rightarrow (\boldsymbol{\mu}_j \nabla_j)$ the interaction of two dipoles can be derived from the interaction of two charges. In a very similar way to charges the Ewald summation of dipoles can be derived and we obtain finally for the real space contribution

$$u_{DR} = \frac{1}{2} \sum_{i=1}^N \sum_{j=1}^N \sum'_{\{\mathbf{n}\}} (\boldsymbol{\mu}_i \cdot \boldsymbol{\mu}_j) B(|\mathbf{r}_{ij} + \mathbf{n}|, \alpha) \\ - [\boldsymbol{\mu}_i \cdot (\mathbf{r}_{ij} + \mathbf{n})][\boldsymbol{\mu}_j \cdot (\mathbf{r}_{ij} + \mathbf{n})] C(|\mathbf{r}_{ij} + \mathbf{n}|, \alpha), \quad (2.107)$$

for the Fourier space contribution

$$u_{DF} = \frac{2\pi}{V} \sum_{\mathbf{k} \neq 0} \frac{1}{k^2} \exp\left(-\frac{k^2}{4\alpha^2}\right) \tilde{M}(\mathbf{k}) \tilde{M}^*(\mathbf{k}), \quad (2.108)$$

for the long range contribution

$$u_{DLR} = \frac{2\pi}{2\epsilon + 1} \frac{M^2}{V}, \quad (2.109)$$

and for the self contribution

$$u_{DS} = -\frac{2\alpha}{3\sqrt{\pi}} \sum_{i=1}^N \mu_i^2. \quad (2.110)$$

In the above equations the functions are defined as follows

$$B(r, \alpha) = \frac{1}{r^3} \left[\frac{2\alpha r}{\sqrt{\pi}} \exp(-\alpha^2 r^2) + \operatorname{erfc}(\alpha r) \right] \quad (2.111)$$

and

$$C(r, \alpha) = -\frac{1}{r^5} \left[\frac{2\alpha r}{\sqrt{\pi}} (3 + 2\alpha^2 r^2) + 3\operatorname{erfc}(\alpha r) \right]. \quad (2.112)$$

In the Fourier contribution we have defined

$$\tilde{M}(\mathbf{k}) = \sum_{i=1}^N (\boldsymbol{\mu}_i \cdot \mathbf{k}) \exp(-i\mathbf{k} \cdot \mathbf{r}_i) \quad (2.113)$$

and $\tilde{M}^*(\mathbf{k})$ is the complex conjugate. Finally, the long range contribution contains the term

$$\mathbf{M} = \sum_{i=1}^N \boldsymbol{\mu}_i. \quad (2.114)$$

These equations are valid for a three dimensional system of dipoles. The same considerations concerning the choice of parameters in order to implement the summation in an efficient way, as in the Coulomb system, apply.

2.4.7.3 Ewald summation for quasi two-dimensional dipoles

In the previous sections we have introduced the Ewald summation technique for Coulomb and three-dimensional dipoles. The particle model we explained in Section 2.1.1 consists of the short-range LJ potential and the long-range quasi two-dimensional dipoles. The Ewald summation has to be adapted to the situation that the system is not infinite in the direction perpendicular to the plane. However, the interaction of 3D dipoles in quasi-2D systems can be written as an absolutely convergent Ewald sum. The resulting energy expression separates into an in-plane contribution, U_{\parallel} , and an out-of-plane contribution, U_{\perp} , each of which consists of a real-space and a reciprocal part. Specifically, one has [187, 144]

$$U_{\parallel} = -\frac{1}{2} \sum_{i,j=1}^N \left(B(r_{ij}) \boldsymbol{\mu}_i^{\parallel} \cdot \boldsymbol{\mu}_j^{\parallel} + C(r_{ij}) \left(\boldsymbol{\mu}_i^{\parallel} \cdot \mathbf{r}_{ij} \right) \left(\boldsymbol{\mu}_j^{\parallel} \cdot \mathbf{r}_{ij} \right) \right) + \frac{\pi}{A} \sum_{\mathbf{G} \neq 0} \frac{\text{erfc}(G/2\alpha)}{G} F_{\parallel}(\mathbf{G}) F_{\parallel}^*(\mathbf{G}) - \frac{2\alpha^3}{3\sqrt{\pi}} \sum_{i=1}^N |\boldsymbol{\mu}_i^{\parallel}|^2, \quad (2.115)$$

and

$$U_{\perp} = -\frac{1}{2} \sum_{i,j=1}^N B(r_{ij}) \boldsymbol{\mu}_i^{\perp} \cdot \boldsymbol{\mu}_j^{\perp} + \frac{\pi}{A} \sum_{\mathbf{G} \neq 0} \left[\frac{2\alpha}{\sqrt{\pi}} \exp\left(-\frac{G^2}{4\alpha^2}\right) - \text{Gerfc}\left(\frac{G}{2\alpha}\right) - F_{\perp}(\mathbf{G}) F_{\perp}^*(\mathbf{G}) \right] + \frac{2\sqrt{\pi}\alpha}{A} \sum_{i=1}^N \sum_{j=1}^N \boldsymbol{\mu}_i^{\perp} \cdot \boldsymbol{\mu}_j^{\perp} - \frac{2\alpha^3}{3\sqrt{\pi}} \sum_{i=1}^N (\boldsymbol{\mu}_i^{\perp})^2. \quad (2.116)$$

In Equation 2.115 and Equation 2.116, the functions B and C are defined as

$$B(r) = -\frac{\text{erfc}(\alpha r)}{r^3} - \frac{2\alpha \exp(-\alpha^2 r^2)}{\sqrt{\pi} r^2}, \quad (2.117)$$

and

$$C(r) = 3\frac{\text{erfc}(\alpha r)}{r^5} + \frac{2\alpha}{\sqrt{\pi}} \left(\frac{3}{r^2} + 2\alpha^2 \right) \frac{\exp(-\alpha^2 r^2)}{r^2}. \quad (2.118)$$

Further, we have introduced the quantities

$$F_{\parallel}(\mathbf{G}) = \sum_{i=1}^N (\mathbf{G} \cdot \boldsymbol{\mu}_i^{\parallel}) \exp(i\mathbf{G} \cdot \mathbf{r}_i), \quad (2.119)$$

and

$$F_{\perp}(\mathbf{G}) = \sum_{i=1}^N \boldsymbol{\mu}_i^{\perp} \exp(i\mathbf{G} \cdot \mathbf{r}_i). \quad (2.120)$$

In Equation 2.115-Equation 2.116 and Equation 2.119-Equation 2.120, A denotes the area of the simulation box and \mathbf{G} are two-dimensional wavevectors with components $G_{x,y} = 2\pi/(\sqrt{A})n_{x,y}$, where $n_{x,y} \in \mathbb{Z}$. As already introduced in Section 2.4.7, the convergence of the Ewald sum is controlled by the parameter α and the number of lattice vectors taken into account in the reciprocal space. In this work we use $\alpha \cdot L = 6.5$ and $(n_x + n_y)^2 < n_{\max}$ with $n_{\max} = 24$. To control this choice we performed test calculations with larger n_{\max} , but they did not yield any significant differences.

2.4.7.4 Parallelization of Ewald summation

In the previous section we introduced the Ewald summation for a dipolar system. The computation of Equation 2.115-Equation 2.120 is the most expensive part in our simulations. In fact, the computation of the Ewald sum takes more than 90% of the overall computation time. There are several strategies to accelerate the computation of these computational expensive parts.

One straightforward way is the use of OpenMP [123], which can be utilized to parallelize the summations over N particles and k_{\max} wave vectors. If the program is running on a machine with multiple CPU's and shared memory, this can lead to significant speed ups. In our case, the overhead through communication introduced by using OpenMP was compensated already at system sizes $N > 200$ particles. This strategy turned out to be extremely time saving.

Another way to improve the computation time is the use of MPI (Message Passing Interface) [114]. If the program is running on a computing cluster and we have access to several machines, we can use them simultaneously to compute the expensive parts of the Ewald sum. The large sums can be split in several parts. These are then sent to different machines, are computed by each machine and finally merged together. Unfortunately this strategy is plagued by a large overhead due to the communication. It turned out to be efficient for systems $N > 1000$.

A third and very exciting strategy is the use of the Graphic Processing Unit (GPU) to compute the Ewald sum. We used the thrust library, a library of parallel algorithms resembling the standard template library in C++ [163]. It provides a high level interface to GPU programming. The basic idea is similar to vector machines. On the GPU computations of large vectors can be performed extremely parallel, since the GPU is made of several hundred CPU's. The Ewald sum can be translated into vector operations and thus computed on the GPU. The overhead is also rather large and this strategy turned out to be efficient for $N > 1500$.

2.5 STATIC PROPERTIES OF FLUIDS

2.5.1 *Fluctuations*

In computer simulations one can measure some quantities of interest directly, e. g., the internal energy U , the temperature T or the particle number N by taking averages throughout the simulation. But even in a well equilibrated system these values are not completely constant. These interesting observable quantities are associated to fluctuations. By computing the standard deviation of a quantity, we can estimate how much we approximate the quantity by just regarding the mean value. In Section 2.3 we have introduced the concept of a first-order and continuous phase transition. Fluctuations are one strategy to characterize such a phase transition and are thus particularly useful in computer experiments and in this work.

A very important example is the energy of a system. The average is defined by [118]

$$U = \langle H \rangle = \frac{1}{Z} \int d\Gamma e^{-\beta H} H, \quad (2.121)$$

this relation can be written in terms of the partition function as

$$U = -\frac{1}{Z} \frac{\partial Z}{\partial \beta} = -\frac{\partial \log Z}{\partial \beta}. \quad (2.122)$$

We can also compute the average of the square

$$\langle H^2 \rangle = \frac{1}{Z} \int d\Gamma e^{-\beta H} H^2 = \frac{1}{Z} \frac{\partial^2 Z}{\partial \beta^2}. \quad (2.123)$$

The instantaneous measurement away from the mean value yields

$$\langle (H - \langle H \rangle)^2 \rangle = \langle E^2 \rangle - \langle E \rangle^2 = \frac{\partial^2 \log Z}{\partial \beta^2}. \quad (2.124)$$

The specific heat is defined as

$$c = \frac{\partial U}{\partial T} = -k_B \beta^2 \frac{\partial U}{\partial \beta} = k_B \beta^2 \frac{\partial^2 \log Z}{\partial \beta^2}, \quad (2.125)$$

which allows us to read the specific heat as

$$\langle E^2 \rangle - \langle E \rangle^2 = \frac{c}{k_B \beta^2}. \quad (2.126)$$

Similar fluctuation relations exist for other quantities as well, e. g., the isothermal susceptibility. We define the magnetization of a system by $M = \sum_i \sigma_i$, where σ_i is the spin of particle i . The susceptibility is then defined as [98]

$$k_B T \chi = \langle M^2 \rangle - \langle M \rangle^2 = \sum_{i,j} (\langle \sigma_i \sigma_j \rangle - \langle \sigma_i \rangle \langle \sigma_j \rangle). \quad (2.127)$$

Also in the GC ensemble we can measure fluctuations. The average particle number is given by

$$\langle N \rangle = \frac{1}{Z_G} \sum_{N_1} \int d\Gamma e^{-\beta(H_1 - \mu N_1)} N \quad (2.128)$$

where Z_G is given by Equation 2.12 and can be written as [146]

$$Z_G = k_B T \frac{1}{Z_G} \frac{\partial Z_G}{\partial \mu}. \quad (2.129)$$

We find then

$$\frac{\partial \langle N \rangle}{\partial \mu} = \beta(\langle N^2 \rangle - \langle N \rangle^2) \quad (2.130)$$

and by using the relation

$$\kappa_T = -\frac{1}{V} \left(\frac{\partial V}{\partial P} \right) = \frac{V}{N^2} \left(\frac{\partial N}{\partial \mu} \right) = \frac{V}{N^2} \beta(\langle N^2 \rangle - \langle N \rangle^2), \quad (2.131)$$

we connect the isothermal compressibility to the particle number fluctuations in a GCMC simulation.

These examples show how information about the ensemble can be gained by computing fluctuations of observables during a simulation.

2.5.2 Correlation functions

Correlation functions are very important quantities to gain insight into the structural properties of fluid systems. We make use of the separation of the configurational integral and the kinetic part introduced in Section 2.2.3. We define the n -particle distribution function by

$$g_N^{(n)}(r^n) = \frac{\rho_N^{(n)}(r_1, \dots, r_n)}{\prod_{i=1}^n \rho_N^{(1)}(r_i)}, \quad (2.132)$$

where we use

$$\rho_N^{(n)} = \frac{N!}{(N-n)! Z_N} \int dr^{(N-n)} \exp(-\beta V_N). \quad (2.133)$$

The above function measures how much the structure of a fluid deviates from complete randomness [66]. In an isotropic fluid the pair distribution function $g_N^{(2)}(r_1, r_2)$ depends only on the distance between two particles and is called the radial distribution function, usually denoted by $g(r)$. The particle density can also be expressed in terms of delta functions, e. g.,

$$\rho_N^{(2)}(r, r') = \left\langle \sum_{i=1}^N \sum_{j \neq i}^N \delta(r - r_i) \delta(r' - r_j) \right\rangle. \quad (2.134)$$

In the same way we can write the pair distribution function in a more convenient way

$$g(r) = \frac{V}{N^2} \left\langle \sum_{i=1}^N \sum_{j \neq i}^N \delta(r - r_j + r_i) \right\rangle. \quad (2.135)$$

The pair correlation function is very important since this quantity can be measured in radiation scattering experiments. It allows us insight into the structure of fluids and many thermodynamic quantities can be expressed by $g(r)$. In general, ensemble averages can be computed by using $g(r)$ [6]

$$\left\langle \sum_i \sum_{j>i} a(r_{ij}) \right\rangle = \frac{1}{2} N \rho \int_0^\infty a(r) g(r) 4\pi r^2 dr. \quad (2.136)$$

In a real simulation one makes use of the delta function representation of $g(r)$. We choose a bin-width δr and we compute a histogram of all pair distances according to δr during a simulation, which is denoted by H_{total} . After taking the ensemble average $H(r) = \langle H_{\text{total}}/N \rangle$, we compare this value to the average number of particle of an ideal gas. The ideal gas leads to the histogram

$$H_{\text{ideal}} = \frac{4\pi\rho}{3} [(r + \delta r)^3 - r^3] \quad (2.137)$$

and we finally obtain

$$g(r + \delta r) = H(r)/H_{\text{ideal}}. \quad (2.138)$$

In a two-dimensional system we choose $H_{\text{ideal}} = \pi\rho[(r + \delta r)^2 - r^2]$. The typical behavior of $g(r)$ is shown in Figure 10.

This function can be extended to the case where the particles depend on separation and orientation. The general form is then [59]

$$g(r_{ij}, \Omega_i, \Omega_j) = \sum_{l_1 l_2 l} \sum_{m_1 m_2 m} \sum_{n_1 n_2} g(l_1 l_2 l; n_1 n_2; r) \\ C(l_1 l_2 l; m_1 m_2 m) \\ \times D_{m_1, n_1}^{l_1}(\Omega_1)^* D_{m_2, n_2}^{l_2}(\Omega_2)^* Y_{lm}^*(\Omega)^*. \quad (2.139)$$

In this equation $C(l_1 l_2 l; m_1 m_2 m)$ are the Clebsch-Gordon coefficients, D_{mn}^l are the general spherical harmonics and Y_{lm}^* are the spherical harmonics. The function $g_{000}(r)$ is the isotropic component and corresponds to the pair distribution function. A complete discussion of this function goes beyond the scope of this work, but can be found in [59].

2.5.3 Structural properties

A quantity to study the local order of a fluid is the so-called bond orientational order parameter. This value is defined by [98]

$$\Psi_n = \frac{1}{N_b} \left| \sum_{i=1}^N \exp(in\theta_i) \right|, \quad (2.140)$$

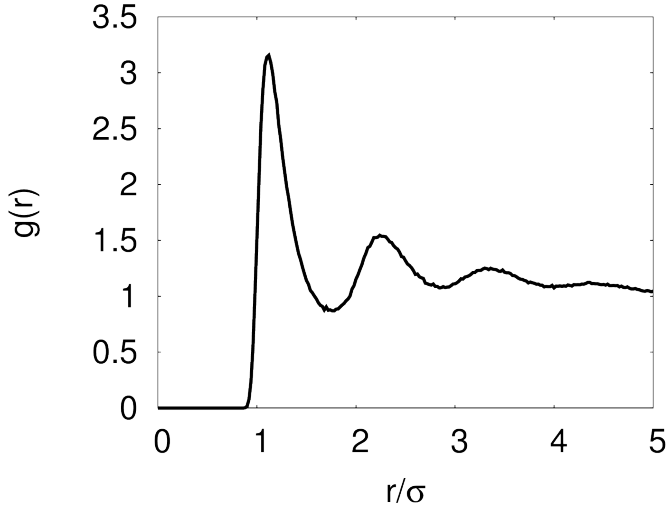


Figure 10: Pair correlation function $g(r)$ of a two-dimensional Lennard-Jones fluid at $T^* = 1.5$ and $\rho^* = 0.4$.

where N_b is the number of local neighbours of one particle and θ_i is the bond angle with neighbour i with respect to an arbitrary axis. This order parameter is 1 if the system displays a n -symmetry and 0 in an isotropic state. A hexagonal order is thus described by a large value of Ψ_6 or a square order by Ψ_4 .

In the case of anisotropic interactions the orientation of particles is an important information as well. To measure the corresponding order parameter of the orientational structure of a system the director has to be identified first. This can be done by using the orientation matrix defined as [6]

$$\mathbf{Q} = \frac{1}{2N} \sum_{i=1}^N 3\hat{e}_{i\alpha}\hat{e}_{i\beta} - \delta_{\alpha\beta}, \quad (2.141)$$

where $e_{i\alpha}$ is the α -th component of the unit vector pointing into the direction of particle i . By solving the eigensystem we can identify the eigenvector \mathbf{n} that is associated with the largest eigenvalue of the matrix \mathbf{Q} . This eigenvalue is usually referred to as P_2 . We can then measure the orientation of all particles with respect to the director what defines the order parameter P_1 by

$$P_1 = \frac{1}{N} \sum_{i=1}^N \hat{e}_i \cdot \mathbf{n}. \quad (2.142)$$

If the system is in a phase with a global orientational order like in a, e. g., nematic or ferroelectric phase, the value of P_1 is close to 1 and in an isotropic phase $P_1 \sim 0$.

2.5.4 Clusters

A crucial question in determining the properties of a fluid system is the definition of clusters. Basically there are two approaches to define if two particles are associated or not. The first possibility is by measuring the distance and if the distance is smaller than a certain minimum, we consider the particles as associated. In the case of anisotropic interactions it is also common to use an energy related definition. Two particles are considered to belong to the same cluster if the interaction energy between these two is attractive and stronger than a certain threshold. In this work we choose the first criterion, since we mainly deal with systems that are not dense. In these systems it is clear if two particles belong into the same cluster or not. We choose the first minimum of the pair correlation function $g(R)$ as the minimum distance, since this value corresponds to the closest neighbours. Also in dense systems we used the same criterion, even though it might not be the best choice. However, slight changes of the parameters revealed no significant changes in our cluster determination. Another important point at high densities is the question how to determine the nearest neighbours. We decided to use the Voronoi decomposition since this criterion is definite.

In fluid systems the aggregation into clusters is a consequence of attractive potentials and the change of the associated order parameter can be described by the degree of polymerization. This quantity measures the amount of particles associated into clusters. It is defined by [33, 153]

$$\Phi = \left\langle \frac{N_a}{N} \right\rangle, \quad (2.143)$$

where N_a is the number of particles in clusters and N is the total number. This order parameter can describe a transition from an unclustered fluid into a polymer fluid, see Section 4.1.1.

A further quantity that is related to clustering in a fluid is the percolation probability. In our simulations we determine the percolation probability Π by controlling if one cluster connects two opposite sites of the simulation box. If that is the case we set $\Pi = 1$, else $\Pi = 0$. During the simulation we take the ensemble average $\langle \Pi \rangle$ to obtain the final percolation probability.

2.6 DYNAMIC PROPERTIES OF FLUIDS

2.6.1 Mean-Square-Displacement

In order to study the dynamic behavior of a fluid system we begin by introducing the ideas underlying the Brownian motion. This stochastic process describes particles that are solved in much smaller and

lighter particles. These small particles collide randomly with the larger particles due to thermal fluctuations. The corresponding equation of motion, introduced by Langevin, reads

$$m\dot{\mathbf{u}} = -m\xi\mathbf{u}(t) + \mathbf{R}(t). \quad (2.144)$$

In this equation $\mathbf{u}(t)$ is the particle velocity, ξ is the friction coefficient and $\mathbf{R}(t)$ is the random force and defined by

$$\langle \mathbf{R}(t) \rangle = 0 \text{ and } \langle \mathbf{R}(t)\mathbf{u}(0) \rangle \geq 0; t > 0, \quad (2.145)$$

and

$$\langle \mathbf{R}(t+s)\mathbf{R}(s) \rangle = 2\pi R_0 \delta(t), \quad (2.146)$$

with

$$\frac{1}{2\pi} \int_{-\infty}^{\infty} \langle \mathbf{R}(t)\mathbf{R} \rangle \exp(i\omega t) dt = R_0. \quad (2.147)$$

The above equations describe the so-called “white-noise” random force. By using the equipartition theorem $\langle \mathbf{u}(t \rightarrow \infty) \rangle = 3k_B T/m$ one can show that [66]

$$\xi = \frac{\pi\beta R_0}{3m} = \frac{\beta}{3m} \int_{-\infty}^{\infty} \langle \mathbf{R}(t)\mathbf{R}(0) \rangle dt, \quad (2.148)$$

which is an example of the fluctuation-dissipation theorem. Now, we can calculate the Mean-Square-Displacement (MSD) of the particles and the Langevin equation yields after some transformations

$$\frac{d^2}{dt^2} \langle |r(t)|^2 \rangle + \xi \frac{d}{dt} \langle |r(t)|^2 \rangle = \frac{6k_B T}{m}, \quad (2.149)$$

and we obtain the solution

$$\langle |r(t)|^2 \rangle = \frac{6k_B T}{\xi m} \left(t - \frac{1}{\xi} + \frac{1}{\xi} \exp(-\xi t) \right). \quad (2.150)$$

The above equation leads to the limiting cases at short times, i. e., $\xi t \ll 1$

$$\langle |r(t)|^2 \rangle \approx \frac{3k_B T}{m} t^2 = \langle \mathbf{u}^2 \rangle t^2 \quad (2.151)$$

and at large times $\xi t \gg 1$

$$\langle |r(t)|^2 \rangle \approx \left(\frac{6k_B T}{\xi m} \right) t. \quad (2.152)$$

By using the definition of the MSD

$$D = \lim_{t \rightarrow \infty} \frac{\langle |r_i(t) - r_i(0)|^2 \rangle}{2dt} \quad (2.153)$$

with the dimension d of the system we obtain the Einstein relation in three dimensions

$$D = \frac{k_B T}{\xi m}. \quad (2.154)$$

The above relations are true for Brownian motion. In this work we employ DMD and MD simulations where the solvent is not simulated explicitly. The limiting cases hold however also in the case of colloidal systems, since the particle movement can be regarded as a random walk and displays the same behavior for small times ($\langle \Delta r \rangle \sim t^2$) and large times ($\langle \Delta r \rangle \sim t$). The behavior is in many cases more complex, like in gels or glassy systems, where the MSD displays subdiffusive characteristics due to cluster formation. We will discuss such a behavior in further detail in Section 4.1.2 and Section 5.3.1.

2.6.2 Van-Hove function

Beside the time correlation functions as, e. g., the MSD the time and space correlation functions provide also important information about a fluid system. Van Hove introduced such a time and space dependent distribution by [66]

$$G(\mathbf{r}, t) = \left\langle \frac{1}{N} \sum_{i=1}^N \sum_{j=1}^N \delta[\mathbf{r} - \mathbf{r}_j(t) + \mathbf{r}_i(0)] \right\rangle \quad (2.155)$$

which can be written as

$$G(\mathbf{r}, t) = \frac{1}{\rho} \langle \rho(\mathbf{r}, t) \rho(\mathbf{0}, 0) \rangle. \quad (2.156)$$

This density-density time correlation can be separated into a “self” and a “distinct” part

$$G(\mathbf{r}, t) = G_s(\mathbf{r}, t) + G_d(\mathbf{r}, t) \quad (2.157)$$

with

$$G_s(\mathbf{r}, t) = \left\langle \frac{1}{N} \sum_{i=1}^N \delta[\mathbf{r} - \mathbf{r}_i(t) + \mathbf{r}_i(0)] \right\rangle \quad (2.158)$$

and

$$G_d(\mathbf{r}, t) = \left\langle \frac{1}{N} \sum_{i=1}^N \sum_{i \neq j}^N \delta[\mathbf{r} - \mathbf{r}_j(t) + \mathbf{r}_i(0)] \right\rangle. \quad (2.159)$$

We obtain at $t = 0$ $G_s(\mathbf{r}, t) = \delta(\mathbf{r})$ and $G_d(\mathbf{r}, 0) = \rho g(\mathbf{r})$. This function can be interpreted as the amount of particles j in $d\mathbf{r}$ around \mathbf{r} at time t , given that there was a particle at $\mathbf{r} = \mathbf{0}$ at $t = 0$. The self part corresponds to the situation that i and j are the same particle where the distinct part represents the correlation between different particles. With increasing time t G_s develops into a bell-shaped curve and G_d disappears.

3

PHASE TRANSITIONS OF TWO-DIMENSIONAL DIPOLAR FLUIDS AND INFLUENCE OF EXTERNAL FIELDS

In the previous chapter we have introduced the basic concepts of statistical mechanics and computer simulations to study fluid systems. In this chapter we present results of extensive GCMC simulations to study first-order phase transitions of dipolar particles that are confined to two dimensions according to the model introduced in Section 2.1.1. We apply external fields of different strength parallel and perpendicular to the two-dimensional dipolar system. In addition, we discuss briefly the case of a rotating external field, where these results are part of a project carried out by Sebastian Jäger within his PhD thesis. We further aim at comparing SU and WL sampling in terms of computational efficiency, introduced in Section 2.4.4.3 and Section 2.4.4.4, respectively.

3.1 SYSTEM WITHOUT EXTERNAL FIELD

In order to study the phase transition of the quasi two-dimensional Stockmayer model we consider three system sizes defined by the simulation box size $L = \sqrt{A} = 27.7\sigma, 37.0\sigma$ and 52.0σ . Each of these systems contains about $N_{\max} = 600, 1000, 2000$ particles in the fluid phase, respectively. Due to the GC sampling the particle number is not constant. By SU and WL sampling we obtain the density probability distribution $P(N)$ of coexisting vapor and liquid at a fixed temperature and chemical potential $\tilde{\mu}$ not exactly at the coexistence point. We then extrapolate $P(N) \rightarrow P'(N)$ to the thermodynamic state at $\tilde{\mu}'$ where both peaks of $P'(N)$ have an equal area [42]. In Section 2.4.4.5 we introduced histogram reweighting to extrapolate the histogram of an order parameter at one thermodynamic state to another state in the vicinity [42, 43]. Once we have obtained the double-peaked structures with equal areas under both peaks, we fit the peaks by a gauss-function and determine the error by the standard deviation of the gaussian fit. We approach the critical temperature by sampling coexisting vapor and liquid phases at different temperatures close to the critical point. From these points in the $\rho - T$ plane we finally obtain the critical

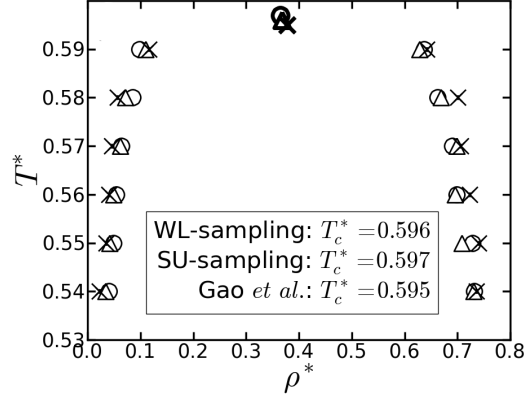


Figure 11: Vapor-liquid coexistence curves at weak coupling of $\mu^* = \sqrt{1}$. Circles denote SU sampling results, triangles denote WL results and crosses correspond to results of Gao *et al.* [51]. For each method, the critical temperature T_c^* is indicated by corresponding bold symbols; the absolute values are shown in the insets.

temperature T_c and critical density ρ_c . We fit our phase diagrams to the scaling law

$$\rho_{\text{liquid}} - \rho_{\text{vapor}} = A(T_c - T)^\beta, \quad (3.1)$$

and the rectilinear law

$$\frac{\rho_{\text{liquid}} + \rho_{\text{vapor}}}{2} = \rho_c + B(T_c - T). \quad (3.2)$$

In Equation 3.1 we use the exponent $\beta = 0.125$ corresponding to the 2D Ising universality class. Indeed, for 3D dipolar systems it is quite established (see, e.g., [50]) that the exponents characterizing the vapor-liquid transition differ only marginally from the 3D Ising results (although, strictly speaking, the long-ranged dipolar interactions give rise to a distinct universality class [2]). For 2D dipolar systems, no such arguments exists; however, consistent with earlier studies [51, 127] we have found that our data for the coexistence line can be fitted quite well assuming 2D Ising behavior. To confirm this assumption we used as an independent check of the critical temperature, for one exemplary system, the behavior of the fourth-order Binder cumulant [22, 137] (see Section 3.1.2).

3.1.1 Weakly coupled systems

As a first benchmark for our techniques we compare phase diagrams obtained by WL and SU sampling with results obtained by Gao and Zeng [51] who used the GEMC technique, with $N = 512$ particles. In Figure 11 and Figure 12 we present results for $\mu^* = \sqrt{1}$ and $\mu^* = \sqrt{3}$, respectively, based on a system size of $L = 27.7\sigma$. Such a system size corresponds to $N \approx 600$ in the fluid phase. We find that at $\mu^* = \sqrt{1}$

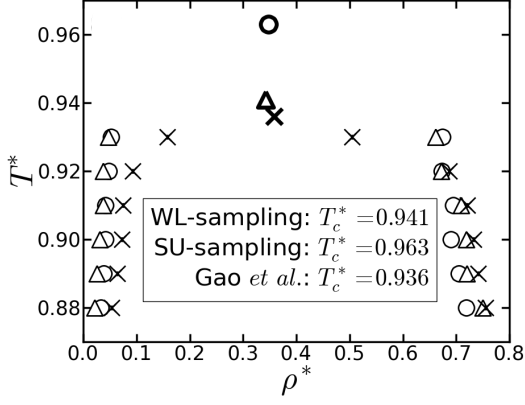


Figure 12: Vapor-liquid coexistence curves at medium coupling of $\mu^* = \sqrt{3}$. Symbols are the same as Figure 11.

the results from the three different techniques are in good agreement. Closer inspection shows that the SU sampling yields a slightly higher critical temperature than the WL sampling. This effect becomes even more pronounced at $\mu^* = \sqrt{3}$ in Figure 12. These differences between WL and SU sampling result from the tendency of the particles in the more strongly coupled system to form head-to-tail configurations such as chains and rings [190, 160]. An illustration is given by the snapshot in the upper part of Figure 13, where $\mu^* = \sqrt{3}$ where short chains and rings are obvious.

The cluster formation yields a problem for the SU sampling method, particularly when small window sizes are used. The reason is that it becomes very unlikely to find a particle that fits into the already formed clusters, like chains and rings, especially at low densities. Increasing the number of insertion/deletion steps did not improve our results. Indeed, an improvement is expected by using larger sampling windows. This, however, would cancel the efficiency of the method as compared to WL sampling or multicanonical MC.

We also see from Figure 12 that, at $\mu^* = \sqrt{3}$, both SU and WL sampling yield smaller vapor densities than the GEMC calculations performed by Gao and Zeng [51]. A possible reason for the deviations could be that in GEMC, the total particle number is fixed, yielding particularly small particle numbers in the vapor phase. Thus, pronounced finite size effects can emerge. Poor statistics is a known problem of GEMC [26]. In our calculations, on the other hand, we did not find large deviations for the vapor densities when considering different system sizes.

To provide more insight into the system we show three snapshots of the weakly coupled system, $\mu^* = \sqrt{1}$, close below the critical temperature of $T_c^* \approx 0.59$ at $T^* = 0.55$ in Figure 14 obtained by canonical MC. One snapshot (left panel) is in the vapor phase, $\rho^* = 0.01$, displaying clearly an isotropic vapor. The metastable phase (middle panel) at

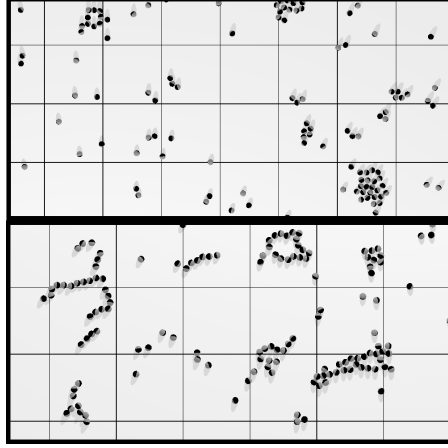


Figure 13: Snapshots of the quasi two-dimensional Stockmayer system at $\mu^* = \sqrt{3}$ (top) and $\mu^* = \sqrt{6}$ (bottom) in the vapor phase.

$\rho^* = 0.4$ shows the coexistence of the vapor and liquid phase, where one liquid cluster together with a small amount of gaseous particles is present. The liquid phase (right panel) is clearly identifiable at the density $\rho^* = 0.75$. The preferred alignment of the dipolar particles in the plane due to the head-to-tail preference without an external field is present, even for the weakly coupled system.

We now consider the system size dependence of the critical temperatures and densities as obtained from Equation 3.1. The system size is an important factor in identifying if the transition may be induced by, e. g., periodic boundary conditions. Our findings are summarized in Table 2 for $L = 27.7\sigma$, 37.0σ and 52.0σ along with the corresponding chemical potentials at the coexistence.

For $\mu^* = \sqrt{1}$ the SU and WL techniques show similar, yet rather small finite-size effects. In particular, the critical temperature [assuming 2D Ising behavior in Equation 3.1] decreases slightly with increasing system size. The finite-size effects become more pronounced for larger dipole moments $\mu^* = \sqrt{3}$. Specifically, the critical temperature T_c^* shows a deviation of about 3% (1.3%) for systems with $L = 52.0\sigma$ as compared to a small system with $L = 27.7\sigma$ for SU (WL) sampling. These findings can be explained by the emerging structures (see snapshot in Figure 13 top) that are sampled less accurately by SU than WL sampling. However, since we are also interested in efficiency we regard the computation time. The SU sampling is around four times faster than the WL sampling in the case of $\mu^* = \sqrt{1}$, and even five times faster at $\mu^* = \sqrt{3}$ (at $L = 37.0\sigma$), see also Table 5. The reason is that with the small window size in SU we perform considerably less insertion and deletion tries as compared to WL.

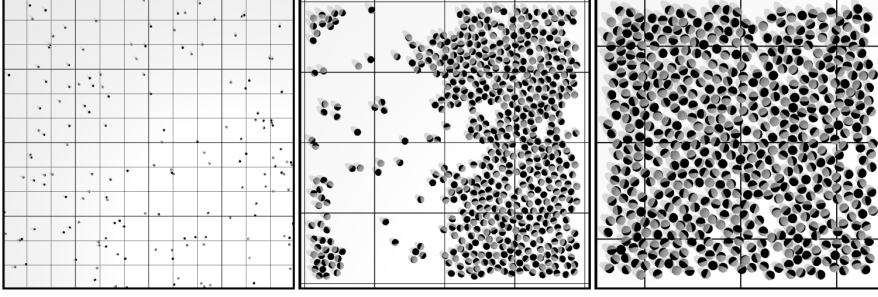


Figure 14: Snapshots of the quasi two-dimensional Stockmayer system at $\mu^* = \sqrt{1}$ and at a temperature close below the critical temperature ($T_c^* \approx 0.59$) at $T^* = 0.55$. The left panel shows the system at $\rho^* = 0.01$, the middle panel at $\rho^* = 0.4$, and the right panel at $\rho^* = 0.75$. The underlying grid in these (and the subsequent) snapshots has a grid width of 10σ .

In order to estimate the system-size dependence of WL sampling we recall that the GC partition function is given as

$$Z(\mu, V, T) = \sum_{N=0}^{\infty} Z(N, V, T) \exp(\beta\bar{\mu}N), \quad (3.3)$$

where $Z(N, V, T)$ is the canonical partition sum. Therefore, and since the WL sampling explores all energy states in a self-adapting way, one would naively expect the computation time to increase exponentially with the system size. However, as indicated by Table 5, the computation time of our WL sampling increases actually slower. We interpret this non-exponential dependence as a consequence of our implementation of parallelization techniques in the use of the Ewald sum, introduced in Section 2.4.7.4. Unfortunately, since we considered only three different system sizes, our data do not allow for a more precise statement on the N-dependence of the computation time. One should also mention that the computation time strongly depends on the sampling parameters. Further, our notion that SU is "faster" refers only to relative times since, obviously, the absolute time to determine one phase coexistence point is strongly correlated to the implementation and architecture the program is running on. Here we used Intel Quad-core 2.83GHz CPUs.

3.1.2 Binder cumulant

If the quasi two-dimensional Stockmayer fluid can be considered as part of the 2D-Ising universality class is still an open question. To elucidate this issue we use as an independent estimate of the critical temperature which, contrary to Equation 3.1, does not require

Table 2: Critical temperature T_c^* , critical density ρ_c^* and corresponding chemical potential $\tilde{\mu}_c^*$ at $\mu^* = \sqrt{1}$, $\mu^* = \sqrt{3}$ and various system sizes.

L	SU			WL		
	$\mu^* = \sqrt{1}$					
	T_c^*	ρ_c^*	$\tilde{\mu}_c^*$	T_c^*	ρ_c^*	$\tilde{\mu}_c^*$
27.7 σ	0.597	0.365	-2.051	0.596	0.368	-2.053
37.0 σ	0.595	0.363	-2.052	0.594	0.362	-2.048
52.0 σ	0.594	0.371	-2.043	0.592	0.381	-2.000
	$\mu^* = \sqrt{3}$					
27.7 σ	0.976	0.348	-3.810	0.948	0.337	-3.810
37.0 σ	0.956	0.345	-3.799	0.954	0.354	-3.804
52.0 σ	0.948	0.346	-3.799	0.960	0.361	-3.816

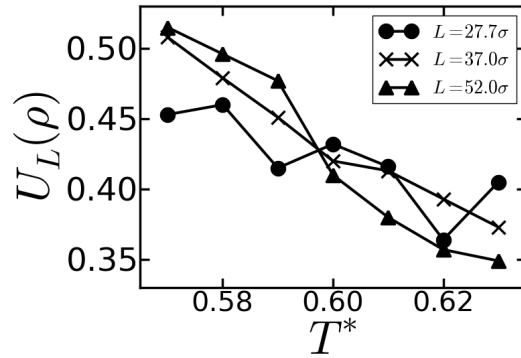


Figure 15: The cumulant $U_L(\rho) = 1 - \langle \rho^4 \rangle / (3\langle \rho^2 \rangle^2)$ as function of temperature at $\mu^* = \sqrt{1}$ and three system sizes (results from WL sampling).

any assumption of the universality class. For this purpose we have calculated the fourth-order Binder cumulant [137], defined by

$$U_L(\rho) = 1 - \frac{\langle \rho^4 \rangle}{3\langle \rho^2 \rangle^2}, \quad (3.4)$$

for all three system sizes. Directly at the critical point of the condensation transition this function is known to become independent of the system size [98]. Therefore, the intersection of the Binder cumulant for different system sizes indicates the location of the critical point. Results for $U_L(\rho)$, which were obtained with WL sampling, as function of the temperature are plotted in Figure 15. The smallest system ($L = 27.7\sigma$) is clearly plagued by pronounced fluctuations. Still, the overall behavior of the corresponding curve already indicates that the transition is strongly rounded as expected in such a small system. The data for the two larger systems in Figure 15 then reflect the sharpening of the transition with increasing system size. Clearly, a

Table 3: Simulation results for coexisting vapor and liquid states at $\mu^* = \sqrt{6}$ and $L = 27.7\sigma$.

SU			
T^*	ρ_{vapor}^*	ρ_{liquid}^*	$\tilde{\mu}^*$
1.54	0.042(15)	0.457(39)	-7.204
1.53	0.109(197)	0.483(62)	-7.236
1.52	0.054(161)	0.500(34)	-7.257
1.51	0.037(12)	0.606(26)	-7.276
1.50	0.051(22)	0.614(26)	-7.310
1.49	0.030(8)	0.530(82)	-7.345
WL			
1.54	0.032(9)	0.340(25)	-7.227
1.53	0.032(20)	0.549(37)	-7.146
1.52	0.041(23)	0.585(55)	-7.276
1.51	0.031(16)	0.616(91)	-7.315
1.50	0.028(14)	0.686(21)	-7.258
1.49	0.018(6)	0.681(26)	-7.338

thorough finite-size scaling study (which was not in the focus of the present work) would require significantly more system sizes and a finer resolution of data points. Nevertheless, based on the intersection point suggested in Figure 15, we can estimate $T_c^* \approx 0.597$, a value which is in fair agreement with our data based on Equation 3.1. In the following we therefore assume our strategy to extrapolate the critical parameters on the basis of Equation 3.1 to be reasonable.

3.1.2.1 Strongly coupled systems

In order to study the capabilities of both techniques when applied to more strongly coupled dipolar systems we now consider the case $\mu^* = \sqrt{6}$. In such systems the formation of structures is very pronounced. In Table 3 we show our simulation results for the coexisting vapor and liquid phase obtained by SU and WL sampling and the system size $L = 27.7\sigma$.

A snapshot of the system in the vapor phase is presented in Figure 13 (bottom), revealing pronounced self-assembly of the particles into chains and rings. Comparing the two techniques, WL sampling yields slightly better statistics in the liquid phase and significant better results in the vapor phase. We obtain considerably smaller standard deviations of our gaussian fits of $P(N)$ (compare values in brackets in Table 3). We can determine $T_c^* = 1.545$, $\rho_c^* = 0.267$ from SU sampling and $T_c^* = 1.550$, $\rho_c^* = 0.291$ from WL sampling. Thus, the critical tem-

Table 4: Critical temperatures, densities, and chemical potentials at $\mu^* = \sqrt{6}$ and various system sizes.

L	SU			WL		
	T_c^*	ρ_c^*	$\tilde{\mu}_c^*$	T_c^*	ρ_c^*	$\tilde{\mu}_c^*$
27.7σ	1.545	0.267	-7.204	1.550	0.291	-7.227
37.0σ	1.536	0.292	-7.188	1.546	0.314	-7.215
52.0σ	1.537	0.282	-7.231	~ 1.55	~ 0.30	~ -7.21

perature for both techniques agrees quite well, despite the different errors. Larger deviations are seen for ρ_c^* , which is also the case for the systems $\mu^* = \sqrt{1}$ and $\mu^* = \sqrt{3}$ (see Table 2). Obviously is the critical density quite sensitive to slight changes in the densities of the corresponding vapor and liquid phase [see Equation 3.2]. Regarding the system-size dependence, we obtain results that are summarized in Table 4, where we show the critical parameters for three system sizes. The finite-size effects are generally smaller for WL sampling. The reason lies in the already mentioned structure formation that is better sampled by the self-adapting WL algorithm which is also reflected by the smaller errors of our fit function. Recall, we sample all states until we reach a “flat” histogram for all densities of interest. This advantage, however, has to be balanced against the much larger simulation times. We note that our WL simulations at $\mu^* = \sqrt{6}$ and the largest system size ($L = 52.0\sigma$) did not converge against a smooth DOS in reasonable time (which is within a month on a computing cluster). We illustrate the problem in Figure 16, where we plot weight-functions for three dipole moments as obtained by WL sampling after 3 iteration steps. Whereas the weight-function for $\mu^* = \sqrt{1}$ is smooth, it already shows some roughness for $\mu^* = \sqrt{3}$. The even rougher landscape at $\mu^* = \sqrt{6}$ indicates that we have to simulate much longer to smooth out the weight-function. Practically, from such a weight-function it is not possible to extract useful information, since the density distribution is the exponential of the weight-functions plotted in Figure 16. The roughness leads to strong errors of the final density distribution. An additional factor is the exponential increase of the number of states with N_{\max} . In Table 5 we compare estimates of our simulation times. The system with $L = 37.0\sigma$ and $\mu^* = \sqrt{6}$ can be explored by SU sampling about ten times faster than with WL sampling. Already at the weak dipole coupling we remark a significant difference of the computation time at large system, what becomes even more pronounced at increasing coupling and system size.

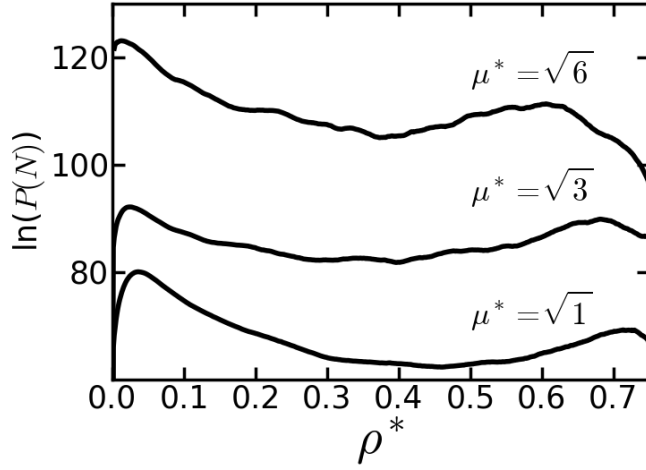


Figure 16: WL results for the DOS of the systems $\mu^* = \sqrt{1}$, $\mu^* = \sqrt{3}$ and $\mu^* = \sqrt{6}$ at temperatures slightly below the corresponding critical temperatures, and $L = 27.7\sigma$. The plots show $\ln(P(N))$ after 3 WL iterations according to our algorithm described in Section 2.4.4.4.

Table 5: Estimated computation time for SU and WL sampling. We use the simulation time of the system at $\mu^* = 1$, $B^* = 0$ and $L = 27.7\sigma$ by SU sampling as a normalization. The rows in SU and WL time indicate results for $L = 27.7\sigma, 37.0\sigma, 52.0\sigma$, respectively.

μ^*	B^*	SU time			WL time		
$\sqrt{1}$	0	1.0	1.2	3.3	2.2	4.8	9.5
$\sqrt{3}$	0	1.0	1.2	3.3	3.5	5.7	15.3
$\sqrt{6}$	0	1.0	1.2	3.3	8.4	12.3	~ 45
$\sqrt{1}$	3	-	-	-	15.1	21.8	-
$\sqrt{3}$	5	-	-	-	8.8	13.6	-

3.2 EXTERNAL FIELD PERPENDICULAR TO PLANE

We now consider the influence of an external field directed in z -direction, i.e. perpendicular to the plane. Figure 17(a) shows the field-induced, average dipole moment at $\mu^* = \sqrt{1}$ in z -direction, defined by

$$m_z = \frac{1}{N\mu} \sum_{i=1}^N \langle \mu_{i,z} \rangle. \quad (3.5)$$

In Figure 17 we show results for m_z . At the very small density $\rho^* = 0.01$, almost all dipoles are aligned in field direction ($m_z \sim 0.9$) already for a weak external field ($B_{\perp}^* = 4$). In the dense system ($\rho^* = 0.80$), the response is much weaker due to the more pronounced competition between the perpendicular ordering favored by the field, on one hand, and the tendency of the particles to arrange in-plane, head-to-tail configurations, on the other hand. Clearly, if the particles were fully aligned perpendicular to the plane, the dipolar interaction Equation 2.2 would be purely repulsive, i.e.

$$U_{DD}(i, j) = U_{DD}^{\perp}(r_{ij}) = \frac{\mu^2}{r_{ij}^3}. \quad (3.6)$$

In Figure 18 we plot the resulting total potential $U_{DD}^{\perp}(r_{ij}) + U_{LJ}(r_{ij})$ in such a perfectly aligned situation. The attractive part of the LJ potential gets balanced out by the repulsive part of the dipole-dipole interaction. At $\mu^* = \sqrt{1}$ the total potential still has an attractive region, but range and magnitude of this region are already significantly reduced relative to the pure LJ case ($\mu^* = 0$). At $\mu^* = \sqrt{3}$ the attraction then completely disappears. In such a situation one would not expect any vapor-liquid transition.

From now on, we therefore focus on a more weakly coupled system characterized by $\mu^* = \sqrt{1}$ and $B_{\perp}^* = 3$. For this system we are still able to determine vapor-liquid phase coexistence. In the inset of Figure 18 we show simulation results for the average two-particle potential, $\langle U_{DD} + U_{LJ} \rangle(r_{ij})$, within the two coexisting phases. In the vapor phase (circles), more dipoles are orientated perpendicular to the plane [see Figure 17(a)] and thus the interaction is less attractive (in both, magnitude and range) than in the liquid phase (triangles).

The orientational bias induced by the external field makes it significantly more difficult for MC simulations to locate phase coexistence as compared to the zero field case. Indeed, with SU sampling we were unable to obtain the DOS in reasonable computation time, not even by increasing the insertion/deletion tries significantly. WL sampling, however, samples the DOS sufficiently well, and we were able to locate the coexistence line of the system with $\mu^* = \sqrt{1}$ and $B_{\perp}^* = 3$. The result is shown in Figure 19.

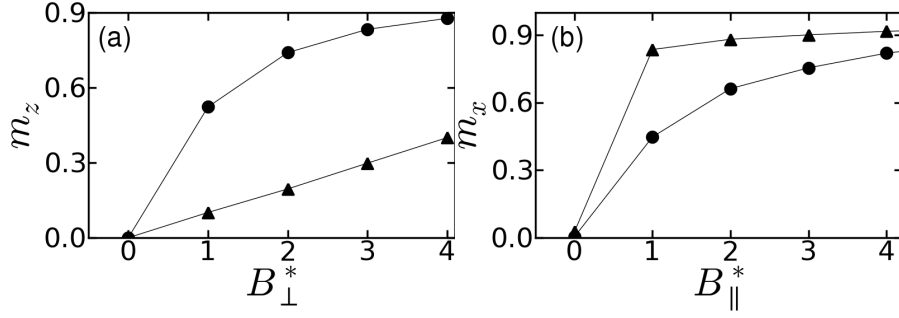


Figure 17: Average dipole moment as function of an external field directed perpendicular to the plane (a) or in-plane (b). For each system, the data have been obtained at a value of μ^* where a clear vapor-liquid transition occurs; the temperatures considered are somewhat below the corresponding critical temperatures. Specifically, we show in (a) results at $\mu^* = \sqrt{1}$, $T^* = 0.4$, and densities $\rho^* = 0.01$ (circles), $\rho^* = 0.80$ (triangles) related to the vapor and liquid phase, respectively. Plot (b) shows corresponding results at $\mu^* = \sqrt{3}$, $T^* = 0.9$, $\rho^* = 0.01$ (circles) and $\rho^* = 0.80$ (triangles).

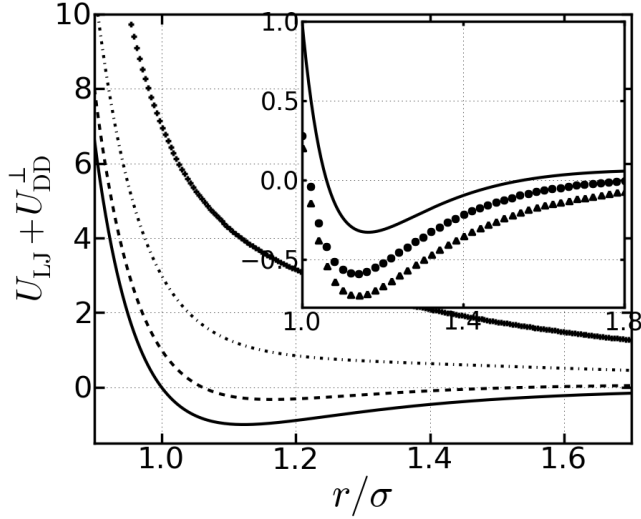


Figure 18: Main part: total pair potential for Stockmayer particles which are perfectly aligned perpendicular to the plane. From bottom to top: $\mu^* = 0$ (solid), $\mu^* = \sqrt{1}$ (dashed), $\mu^* = \sqrt{3}$ (dots), $\mu^* = \sqrt{6}$ (crosses). The inset shows the theoretical curve (solid line) compared to our simulation data ($\mu^* = \sqrt{1}$, $B_{\perp}^* = 3$) for the vapor (circles) and liquid phase (triangles).

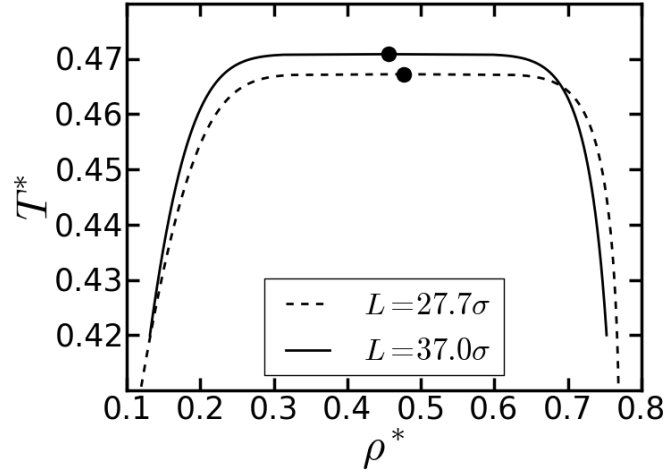


Figure 19: Phase diagram obtained by WL sampling at $\mu^* = \sqrt{1}$, $B_{\perp}^* = 3$, and two system sizes. The filled circles indicate the critical temperature T_c^* .

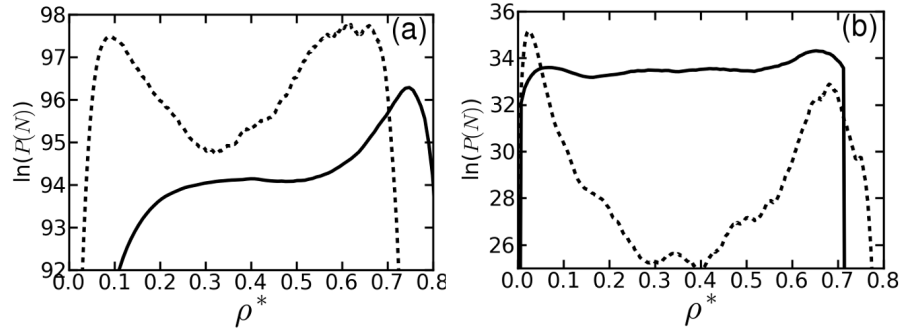


Figure 20: (a) Weight-functions obtained by WL sampling at $\mu^* = \sqrt{1}$, $B_{\perp}^* = 3$ after 4 WL iterations (solid line) and $\mu^* = \sqrt{1}$, $B^* = 0$ after 2 WL iterations (dashed line). In (b) we plot the WL weight-functions at $\mu^* = \sqrt{3}$, $B_{\parallel}^* = 5$ after 4 WL iterations (solid line) and at $\mu^* = \sqrt{3}$, $B^* = 0$ after 3 WL iterations (dashed line).

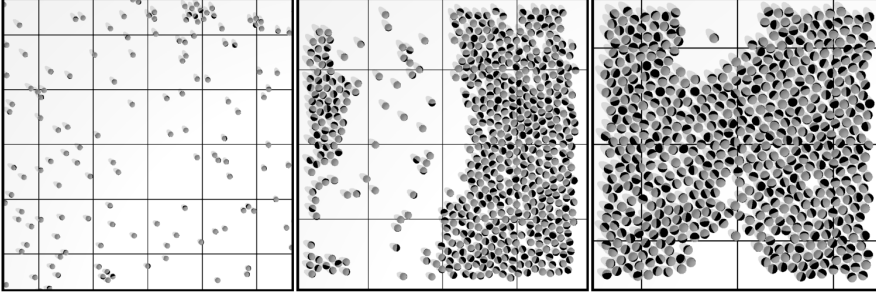


Figure 21: Snapshots of the quasi two-dimensional Stockmayer system at $\mu^* = \sqrt{1}$, $B_{\perp}^* = 3$, and at a temperature close below the critical temperature ($T_c^* \approx 0.47$) at $T^* = 0.42$. The left panel shows the system at $\rho^* = 0.05$, the middle panel at $\rho^* = 0.45$, and the right panel at $\rho^* = 0.75$.

For $L = 27.7\sigma$, the critical parameters are $T_c^* = 0.467$ and $\rho_c^* = 0.476$. Increasing the system size to $L = 37.0\sigma$ we find $T_c^* = 0.471$ and $\rho_c^* = 0.456$, indicating that particularly the critical density is sensitive to the system size, a fact that we already found in the zero field case. We also note that the critical temperature has decreased around 20% as compared to the same system without external field. This decrease is expected due to the increase of the overall repulsion induced by the field.

As a technical remark, we note that the computational time to obtain a smooth DOS within the WL method for this system ($B_{\perp}^* = 3$) is about seven times longer than for the same system at $B^* = 0$. These problems are illustrated in Figure 20(a) where we compare the corresponding DOSs. Although the weight-function in field is rather smooth, the peak of the liquid phase is much more pronounced than the corresponding vapor peak. This indicates the difficulties of the system to build a stable vapor phase.

In Figure 21 we show three snapshots of the system at the vapor phase, $\rho^* = 0.05$ (left panel), metastable phase $\rho^* = 0.45$ (middle panel), and liquid phase $\rho^* = 0.75$ (right panel) obtained by canonical MC. These snapshots are at a temperature of $T^* = 0.42$ which is close below the critical temperature of $T^* \approx 0.47$. Compared to the same system without external field in Figure 14 the metastable phase and the liquid phase are somehow more compact. The reason is that the vapor-liquid coexistence takes place at a lower temperature due to the stronger repulsion emerging from the interaction of dipoles aligned perpendicular to the field. Thus, the LJ part of the interaction is more dominant and keeps the particles at close distances together.

Finally, an interesting aspect of the perpendicular field is that it favors crystallization. The crystal structures that one may expect in such a system were already studied [27]. This is demonstrated in Figure 22, where we plot the in-plane correlation function for different densities at a temperature close to $T_c^* = 0.471$. The correlation function $g(r)$

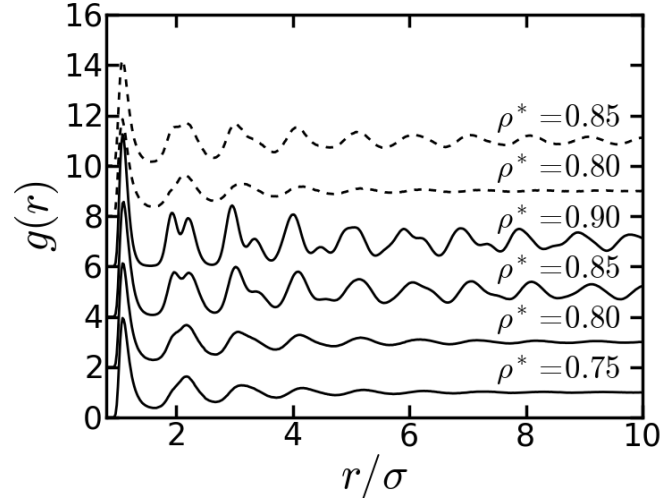


Figure 22: In-plane correlation function $g(r)$ for different densities at $T^* = 0.45 < T_c^* = 0.471$ for $\mu^* = \sqrt{1}$ and $B_{\perp}^* = 3$ (solid lines). The dashed lines show $g(r)$ in the corresponding zero-field system at $T^* = 0.57$ (the critical temperature is $T_c^* = 0.596$).

for $\rho^* = 0.80$ is still fluid-like. By slightly increasing the density to $\rho^* = 0.85$ we observe double-peaks which are indicative of hexagonal ordering. This effect becomes even more pronounced for $\rho^* = 0.90$. The dashed lines in Figure 22 show $g(r)$ for the same system without external field, where the ordering is clearly less developed even at $\rho^* = 0.85$. Therefore, the system in the perpendicular field is already at or close to the tri-critical point, which occurs at somewhat larger densities in zero field. We note that the preference of crystalline over liquid states is a very typical phenomenon in systems where the overall attractive range is particularly small [65]. In the present case, the reduction of attraction occurs as a consequence of the perpendicular field and the resulting repulsive (average) dipolar interactions. However, very similar behavior (to the point of a complete suppression of the liquid phase) is found in colloid-polymer mixtures and in some molecular fluids such as C_{60} , all of which are characterized by very narrow ranges of attraction in the corresponding interaction potentials [65].

3.3 EXTERNAL FIELD IN THE PLANE

We finally consider a system with an external field directed in the plane. In this situation, there is no competition between field and interaction effects; the field rather supports the in-plane, head-to-tail configurations of the dipolar particles. As a consequence, the system strongly orders already at small field strengths (such as $B_{\parallel}^* = 1$) as reflected by the magnetization plots in Figure 17(b) at $\mu^* = \sqrt{3}$.

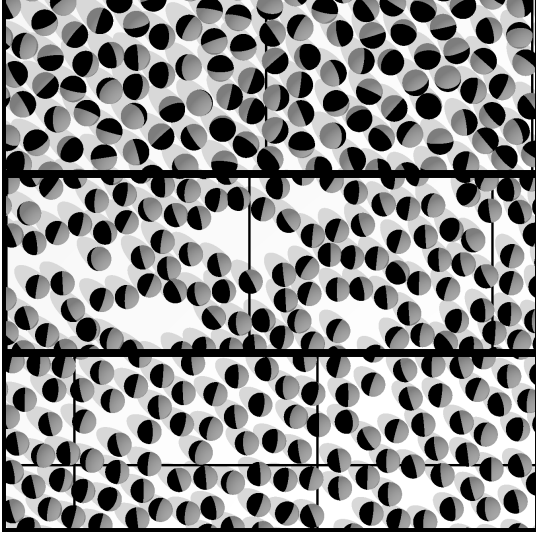


Figure 23: Snapshots at $\mu^* = \sqrt{3}$, $\rho^* = 0.65$, and $B_{\parallel}^* = 0$ (directed from left to right), 5, and 10 (from top to bottom).

The corresponding microscopic structure is illustrated in Figure 23 where we present snapshots under liquid-like conditions and different B_{\parallel}^* .

Whereas the zero-field system is essentially homogeneous, a parallel field of strength $B_{\parallel}^* = 5$ induces a network-like structure. Upon further increase to $B_{\parallel}^* = 10$, the network changes into long chains that are aligned parallel to the field. Due to these strongly correlated structures, sampling of the fluid phase is very time-consuming. The strong orientational order flattens the free energy landscape, which makes it essentially impossible for SU sampling to correctly identify the free energy minima of the gas and the liquid phase. Indeed, we were not able to identify the vapor and liquid phase with SU sampling. WL sampling, on the other hand, is perfectly suited to locate phase coexistence. Interestingly, the WL simulations require only slightly longer times to yield a smooth DOS than at $\mu^* = \sqrt{3}$ and $B^* = 0$. An exemplary case is shown in Figure 20(b) where we show the DOS obtained after several WL iterations for the system without field and with the in-plane field. The peaks corresponding to the free-energy minima of the two coexisting phases are very weak compared to the zero field case. The resulting phase diagrams for two system sizes ($L = 27.7\sigma$ and 37.0σ) are plotted in Figure 24.

The critical parameters are $T_c^* = 1.310$ (1.306), $\rho_c^* = 0.338$ (0.331) for the smaller (larger) system, respectively. The finite-size effect is rather small. Comparing with the corresponding zero-field system we find that the critical temperature is increased by about 40%.

To illustrate the system we show again three snapshots close below the critical temperature, $T_c^* \approx 1.31$, at $T^* = 1.24$ in Figure 25 at the density $\rho^* = 0.05$ (left panel), $\rho^* = 0.4$ (middle panel), and $\rho^* = 0.7$

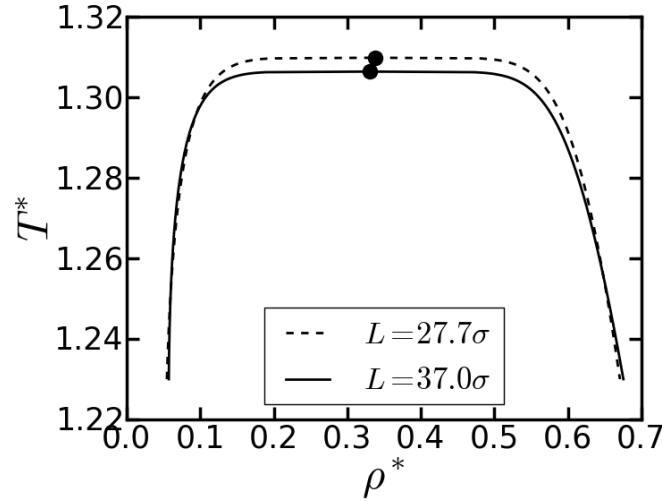


Figure 24: Phase diagram at $\mu^* = \sqrt{3}$, $B_{\parallel}^* = 5$ and two system sizes. The filled circles represent the critical temperature.

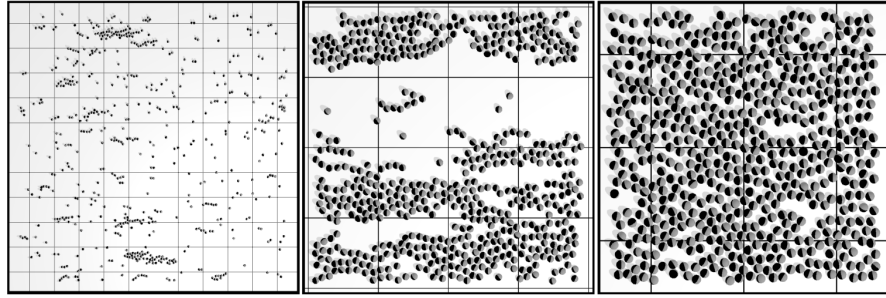


Figure 25: Snapshots of the quasi two-dimensional Stockmayer system at $\mu^* = \sqrt{3}$, $B_{\parallel}^* = 5$ (directed from left to right), and at a temperature close below the critical temperature ($T_c^* \approx 1.31$) at $T^* = 1.24$. The left panel shows the system at $\rho^* = 0.05$, the middle panel at $\rho^* = 0.4$, and the right panel at $\rho^* = 0.7$.

(right panel). These snapshots were obtained by canonical MC. The preference into the external field direction is clearly obvious even in the low-density phase. The metastable phase displays a larger cluster than a similar system without field (see Figure 14). The liquid phase is isotropic, even though a strong orientational bias is introduced by the external field.

3.4 ROTATING EXTERNAL FIELD

The results of this section are part of a project carried out by Sebastian Jäger within his PhD thesis. He performed extensive Molecular Dynamics and Brownian Dynamics simulations to study the dynamic properties of a dipolar system in two dimensions exposed to a rotating

external field. In this work the dipolar Soft-Sphere model was used, contrary to the previous sections.

By exposing the quasi two-dimensional dipolar system to a rotating field of sufficient strength and frequency an agglomeration of the particles into clusters can be observed in experiments [184, 195]. This clustering leads to the conclusion that attractive forces resulting from the dipolar interaction are present. Indeed, by averaging the dipolar inter-particle interaction potential over one rotational period of the external field under the assumption that the particles rotate synchronously with the field, i. e., follow the field at a constant phase difference we obtain

$$U_{ID}(\mathbf{r}_{ij}) = -\frac{\mu^2}{2r_{ij}^3}. \quad (3.7)$$

Hence, if the particles do not move significantly during one period of the field, the effective inter-particle potential is attractive and decays isotropically as $\propto 1/r^3$. For Equation 3.7 to be a sufficient good approximation to the true inter-particle interaction, it is crucial that essentially all the particles follow the field. An extensive analysis of this synchronization behavior of the dipolar particles with the field in three dimensions can be found in [79].

Thus, by assuming the particles are fully synchronized with the external field we can study the non-equilibrium field driven system with the equilibrium MC methods. The system can be investigated as an equilibrium system with the effective interaction given in Equation 3.7. We show that the observed clustering in the experiments [184, 195] is a consequence of an equilibrium first-order phase transition. To this end, we have performed WL simulations of $N = 900$ particles. The long-range character of the interaction can be taken into account by assuming that the regular dipole-dipole interaction Equation 2.2 reduces to Equation 3.7, if the dipoles are oriented perpendicular to the plane [150]

$$U_{DD}(\boldsymbol{\mu}_{i,j} = \mu \mathbf{e}_z) = \frac{\mu^2}{r^3} = -2U_{ID}. \quad (3.8)$$

To this end, we employ the Ewald summation to compute the long range character of the effective interaction.

In order to focus on the dipole driven phase separation we use the dipole-dipole interaction combined with the purely repulsive SS potential. We use a strong coupling of $\mu^* = \sqrt{9}$ which is necessary to obtain a condensation transition. We obtain from our WL simulations a phase diagram that is presented in Figure 26. Indeed we found a gas-liquid phase transition in the non-driven system. How does this translate to the field-driven non-equilibrium system? Since the effective particle-interaction in the driven system approaches the one

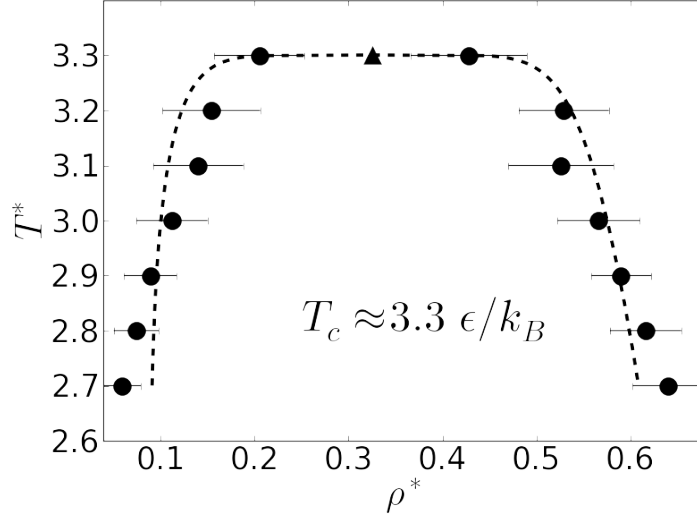


Figure 26: Phase diagram of dipolar Soft-Spheres with $\mu^* = \sqrt{9}$ and a rotating external field. T_c is the critical temperature.

given by Equation 3.7 for sufficiently high frequencies of the field, we expect the non-equilibrium system to behave very similarly to the equilibrium one. In this work we did not carry out the necessary non-equilibrium investigation. Further, we did not use different system sizes or different simulation techniques for this system. We could, however, identify the phase separation of a quasi two-dimensional system exposed to a rotating external field. This behavior is in marked contrast to the systems of quasi two-dimensional dipoles on a plane without field or exposed to a static field parallel and perpendicular to the plane studied in the previous sections. Earlier simulation studies confirm that an additional attractive interaction is necessary to observe a condensation transition of dipolar fluids [29, 49, 56]. The dipoles exposed to a rotating external field display, however, a phase separation even without additional attractive potentials.

3.5 SUMMARY

In this chapter we have used MC simulations combined with SU and WL sampling to study vapor-liquid phase transitions in quasi 2D Stockmayer fluids with 3D dipole moments. Our results for $\mu^* = \sqrt{1}$ and $\mu^* = \sqrt{3}$ (and zero field) agree well with previous GEMC results [51]. Moreover, there is also fair agreement with very recent MD data [127], where the coexistence curves were determined by a Maxwell construction. Both other studies used however smaller system sizes, containing $N \approx 500 - 600$ particles, whereas we studied these system at considerable larger system sizes. At most our simulations contain $N \approx 2000$ particles in the liquid phase.

From a methodological perspective, our calculations indicate that SU sampling is faster than WL in terms of computation time, compare Table 5; moreover, it is quite accurate if the dipolar coupling is not too strong. Indeed we found good agreement in the zero field case, see Table 3 and Table 4. However, due to the small window size, finite-size effects are more pronounced in SU than in WL sampling. On the other hand, the computation time for WL sampling increases significantly with the dipolar coupling because the free energy landscape becomes more and more rough, yielding difficulties to explore all states. To explore all states and to obtain a flat histogram we need significantly more insertion/deletion tries. Still, judging from finite-size effects, WL sampling seems to be the more reliable method to locate critical parameters in strongly coupled, zero-field systems (such as in the case $\mu^* = \sqrt{6}$ considered here). In test calculations, we still found phase separation for higher couplings, $\mu^* > \sqrt{6}$. However, we did not attempt to determine at which value of μ^* the condensation transition possibly disappears. This is due to the strong increase of computation time in strongly coupled systems.

We also studied the influence of external fields perpendicular and parallel to the plane on the condensation phase transition. The external field generally flattens the DOS [106] and thus makes it difficult for MC simulations to locate the free energy minima for gas and liquid phase. Indeed, by SU sampling we were not able to find those minima at all.

The external field introduces a strong orientational bias which makes it generally more difficult for MC simulations to locate the free energy minima for gas and liquid phase (as compared to the zero-field situation). As an attempt to solve that problem one could check the performance of a biasing algorithm as suggested, e.g., in Ref. [26]. Here we did not pursue that problem further, but studied the systems by WL sampling.

A field perpendicular to the plane introduces a competition between the alignment parallel to the field and the otherwise favored in-plane, head-to-tail configurations. The overall interaction becomes less attractive, compared to the pure LJ fluid, even purely repulsive for strong dipolar couplings, see Figure 18. As a consequence the critical temperature decreases significantly even for relatively weak dipolar coupling and field strengths. On the other hand, we found that the effective (average) potential between the (partially) aligned Stockmayer particles yields a higher tendency for crystallization. This is consistent with earlier findings on the occurrence of crystalline phases in two-dimensional systems with long-range, repulsive interactions [27, 76, 11]. More generally, our finding comforts with the well-known phenomenon [65] that reduction of the attractive range of the interaction potential stabilizes crystalline states.

We discussed a system under the influence of an in-plane field. Compared to the perpendicular field, the WL sampling converges even faster, and we were able to determine the full phase diagram for $\mu^* = \sqrt{3}$ and $B_{\parallel}^* = 5$. At larger dipole couplings or external fields we still found evidence for phase separation, but did not investigate these cases systematically due to the strong increase of computation time.

The influence of an rotating field was also investigated in this work. If the particles are fully synchronized with the external field we obtain a effective interaction that can be studied by equilibrium MC techniques. We could identify a vapor-liquid phase separation of such a driven system by employing WL simulations. Remarkably is the fact that such a system shows a phase separation induced by the dipole-dipole interaction, which is not present in any other dipolar system.

To conclude this chapter, SU sampling turned out to be well suited for dipolar systems with pronounced minima in the free energy landscape, a situation occurring at zero field and not too large dipolar coupling. Moreover, in these cases SU is significantly faster than WL sampling. Clearly, due to the restricted quality of our data and the fact that we considered only up to three different system sizes, we were merely able to draw qualitative conclusions about the computation times of SU and WL sampling. For a future, more quantitative comparison it seems promising to analyze certain autocorrelation functions as function of the MC steps, particularly the decay of the density-density autocorrelation, as suggested in a GCMC study of Orkoulas [124]. In this way we could give a quantitative criterion for the convergence of the sampling. For systems under the influence of an external field only WL sampling generates the true DOS, since it is self-adapting. The smoothness of the DOS, however, is at the expense of computation time. We note that interesting information regarding the occurrence of condensation can be obtained by inspecting the weight-function during the WL procedure.

Starting from our results it would be very interesting to study the effect of inhomogeneous external fields on the phase behavior. Such fields are realized, e.g., in dielectrophoretic experiments with polarizable colloids [47]. A further question concerns the impact of particle size heterogeneity [158, 99], which is essentially omnipresent in real systems.

4

PHASE DIAGRAM OF TWO-DIMENSIONAL SYSTEMS OF DIPOLE-LIKE COLLOIDS. A MOLECULAR DYNAMICS STUDY.

In the previous Chapter 3 we investigated first-order phase transitions of quasi two-dimensional Stockmayer particles, a combination of LJ and dipole-dipole interactions. By using advanced MC techniques we focused on the “static” behavior of these systems.

In the present chapter we turn towards dipole-like colloids that are confined to the plane and possess a two-dimensional interaction. We use the DMD method and we investigate the one-component model of [56] in 2D. In the previous Chapter 3 we performed extensive MC simulations with true dipoles. The long-range interactions were handled via the Ewald summation technique. The gain in simulation time of the DMD method compared to the long-range interactions is about 10-20 times. In fact, with our computational resources it would be impossible to carry out a broad investigation of the phase diagram with true dipoles. We concentrate in this chapter on both, static and dynamic phenomena. We investigated several order parameters to sketch a phase diagram for such a system. Further, we elucidate the question of gelation of our particle model confined to a plane.

4.1 FLUID PHASES

4.1.1 *Polymerization*

We first study the system at low and medium densities. At high temperatures the colloids form a completely disordered fluid phase corresponding to the behavior of the pure HS system. Upon decreasing the temperature the anisotropic interactions between the dipole-like colloids become more and more important. As a result the particles start to connect into clusters. The strong clustering finally yields a polymerization “transition”. In general, there are two different approaches which allow to locate polymerization in the phase diagram. One strategy consists of searching for a maximum in the specific heat [83]. The other method, introduced in Section 2.5.4, to measure such a transition of an unclustered fluid into a fluid dominated by clusters is the degree of polymerization Φ [33, 153].

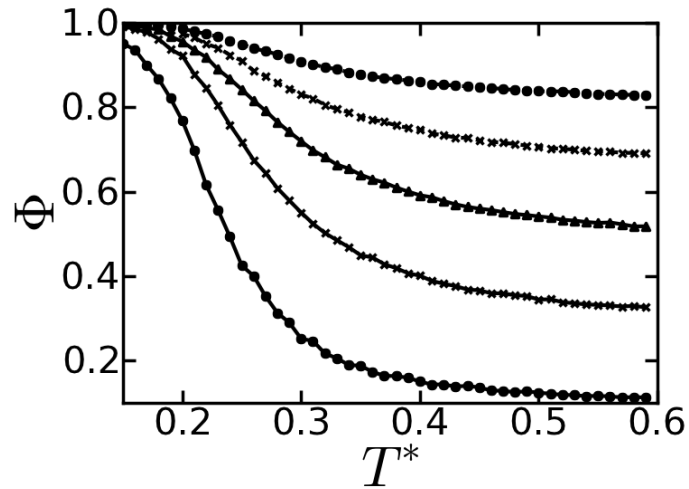


Figure 27: Degree of polymerization as function of temperature at different densities. From bottom to top: $\rho^* = 0.05, 0.15, 0.25, 0.35, 0.55$.

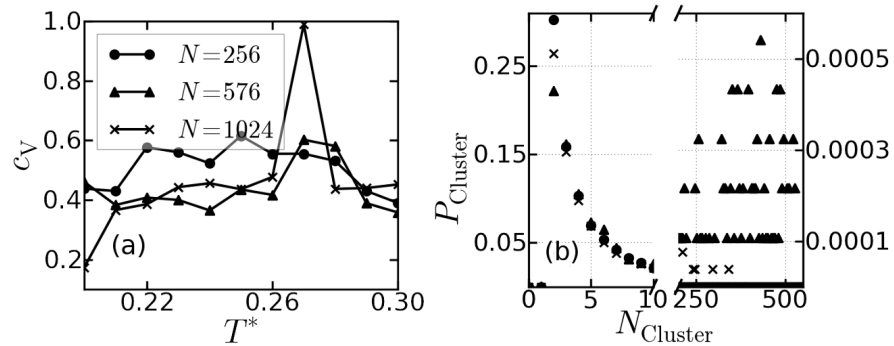


Figure 28: (a) Specific heat c_V of the system at $\rho^* = 0.1$ and three system sizes. (b) Probability P_{Cluster} of finding a cluster with size N_{Cluster} at $\rho^* = 0.4$ and a system size of $N = 576$. Circles correspond to $T^* = 0.35$, crosses to $T^* = 0.25$, and triangles to $T^* = 0.2$. At $N_{\text{Cluster}} = 2$, there is a pronounced peak for all three temperatures considered. In the range $N_{\text{Cluster}} \sim 200 - 576$, there is essentially no peak at $T^* = 0.35$ (circles) and only a small non-zero probability at $T^* = 0.25$ (crosses). On the other hand, at $T^* = 0.2$ (triangles) a clear peak arises at $N_{\text{Cluster}} \sim 400$.

To measure the quantity defined in Equation 2.143 we consider two particles to be associated into the same cluster if the distance between the HS is smaller than the “critical” radius $r_c = 1.25\sigma$. This value was chosen because it corresponds to a distance close to the first minimum of the radial distribution function for a broad range of temperatures and densities. We identify the nearest neighbours by using a Voronoi decomposition. The latter proves to be particularly useful in the high density regime.

In Figure 27 and Figure 28(a) we present results for the two quantities Φ and c_V as function of the temperature and different densities. Both quantities have been evaluated for three different system sizes, $N = 256, 576$, and $N = 1024$. As seen from Figure 28(a), the specific heat does display a maximum, but only for the largest system size considered. Moreover, the whole function $c_V(T^*)$ is subject to strong statistical errors. We therefore focus on the order parameter Φ , which turns out to be robust against variation of N . The polymerization temperature is commonly identified by the inflection point of the function $\Phi(T^*)$ at a given density [153]. Inspecting the data in Figure 27 one notes that, based on the above criteria, a pronounced transition only occurs at low densities ($\rho^* < 0.3$). Upon increasing ρ^* , the parameter Φ has relatively large, non-zero values already at higher temperatures, making the detection of an inflection point less obvious. Indeed, an inspection of corresponding snapshots from the simulations reveals aggregation into small clusters already at large T^* . Nevertheless, upon lowering T^* we observe a change of Φ from intermediate values to a value close to 1, indicating a sudden increase of the largest cluster size. As an additional criterion for polymerization particularly at high densities, we have investigated the cluster-size distribution, that is, the probability to find a cluster of size N_{Cluster} . In Figure 28(b) we plot corresponding numerical results for $\rho^* = 0.4$ and three different temperatures (at the system size $N = 576$). Above the polymerization temperature $T^* = 0.314$ [as determined via the inflection point of the function $\Phi(T^*)$] most particles are already associated into small clusters of size $2 < N_{\text{Cluster}} < 10$. Within the polymerized state ($T^* = 0.25$) the distribution reflects the presence of a small number of large clusters with $N_{\text{Cluster}} \sim 250$ [see crosses on the right hand side of Figure 28(b)]. By further cooling the system one then observes the emergence of a second peak in the cluster-size distribution, indicating the presence of a significant amount of large clusters. This occurs slightly above the percolation temperature ($T_{\text{perc}}^* = 0.194$, see next section). The estimated transition line $T^*(\rho^*)$ which separates the non-aggregated high-temperature regime (region I) from the aggregated polymerized “state” (region II) is shown in Figure 29. Interestingly, these predictions from our DMD simulations are quite consistent with those from a recent integral equation study [104] for a two-dimensional system of DHS. In the latter study, the temperatures related to aggregation

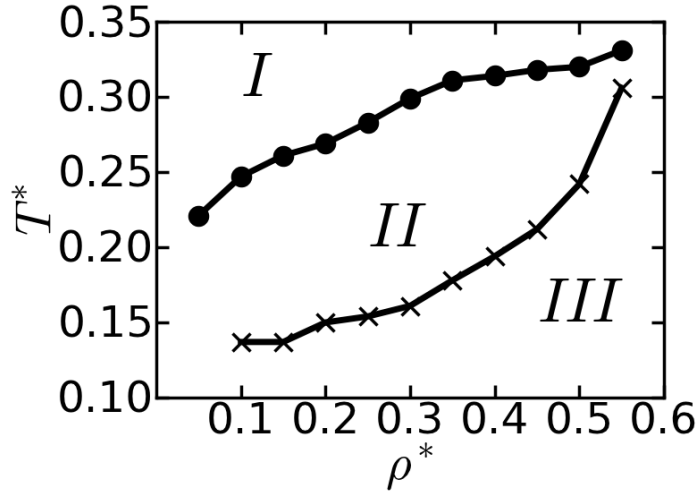


Figure 29: Phase diagram of the system at low and medium densities. Regions I, II and III correspond to the homogeneous fluid (I), the string fluid (II), and the percolated fluid (III), respectively. The upper (lower) line denotes the temperatures $T^*(\rho^*)$ related to the polymerization (percolation).

have been estimated on the basis of the reference hypernetted chain approximation for the pair correlation function.

4.1.2 Percolation and related dynamics

By further decreasing the temperature within the low and medium density region, the small clusters characterizing the polymerized state start to connect into large clusters that span the whole system. The parameter range of the resulting low-temperature state is indicated by region III in Figure 29. The two snapshots shown in Figure 30 illustrate the change of microstructure between region II and III. If one cluster connects two opposite ends of the simulation cell we consider the system as percolated. To determine the percolation probability we count 1 if during a simulation we find a percolating cluster and 0 else. By taking the ensemble average we finally obtain the percolation probability.

In order to investigate the percolation transition more quantitatively, we plot in Figure 31(a) the percolation probability Π at the density $\rho^* = 0.3$ for two different system sizes as function of the temperature T^* . In principle, the transition temperature is determined by the crossing point of the curves for different system sizes [118]. However, to restrict the computational effort we limit the system size to $N = 1024$ at $\rho^* > 0.2$ and $N = 576$ at $\rho^* < 0.2$. For these systems, we determine the transition temperatures by the point where $\Pi(T^*) \sim 0.5$ (see, e.g., [111] for a similar strategy). Nevertheless, as seen from Figure 31(a),

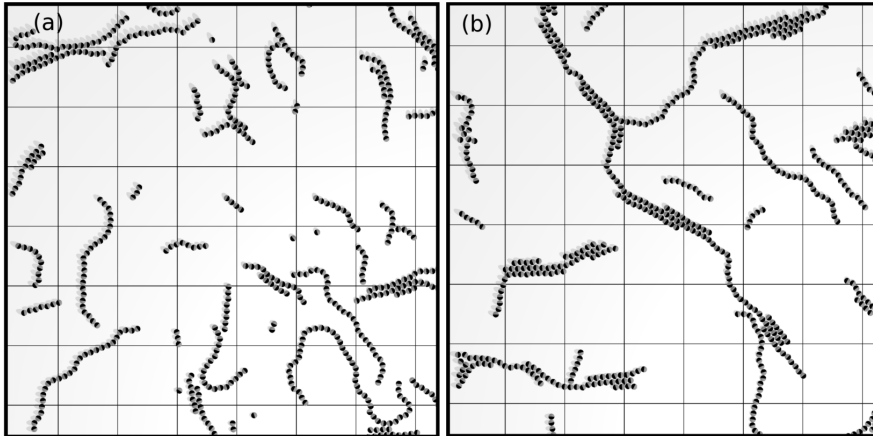


Figure 30: DMD simulation snapshots of the system at $\rho^* = 0.1$ at two temperatures close to the percolation transition occurring at $T_{\text{perc}}^* = 0.134$. In (a) the system is close above the transition ($T^* = 0.15$) while in (b) it is close below the percolation threshold ($T^* = 0.125$).

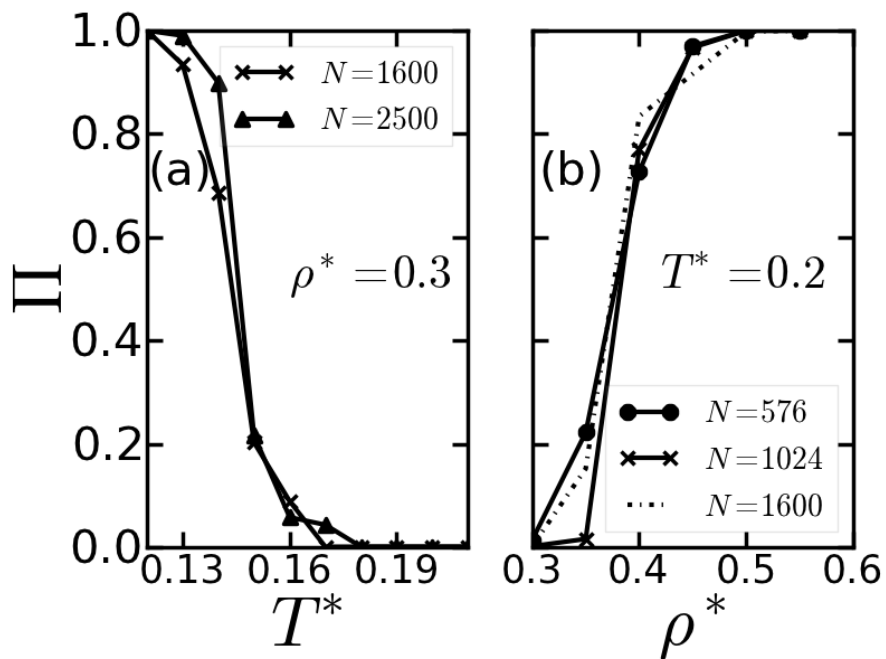


Figure 31: (a) Percolation probability Π as function of the temperature at $\rho^* = 0.3$ for two different system sizes. (b) Percolation probability as function of the density ρ^* at temperature $T^* = 0.2$.

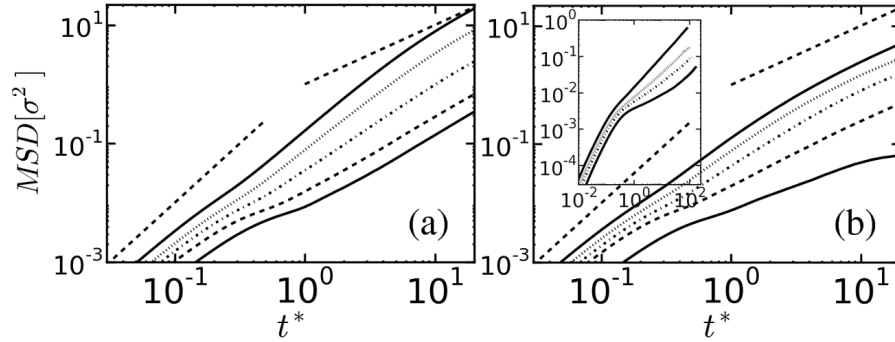


Figure 32: The MSD defined according to Eq. (4.1) at (a) $\rho^* = 0.1$ and (b) $\rho^* = 0.5$ in a double-logarithmic representation. The lines correspond to different temperatures $T^* = 0.3, 0.25, 0.20, 0.10, 0.05$ from top to bottom. The dashed lines show ideal ballistic (slope 1) and diffusive (slope 2) behavior. The inset of (b) shows the MSD at $\rho^* = 0.5$ at larger time scales for the temperatures $T^* = 0.2, 0.15, 0.10, 0.05$ (from top to bottom).

rather large system sizes ($N = 1024 - 2500$) are required to identify the percolation temperature from the plots of $\Pi(T^*)$; for smaller sizes ($N = 576, 1024$) the data are plagued by pronounced statistical errors. Indeed, from the perspective of reducing finite-size effects it turns out to be advantageous to consider the percolation probability as function of the density (rather than as function of T^*). Corresponding data are plotted in Figure 31(b). By increasing the density of the system the percolation temperature continuously increases. Finally, at the density $\rho^* \sim 0.55$ the polymerization and the percolation lines collapse Figure 29.

We now turn to the question whether the percolation (and accompanying network formation) in our system leads to gelation. Indeed, previous studies of a variety of aggregating colloidal systems, e. g., patchy particles [200] have shown that percolation is prerequisite of gelation, however, it is not sufficient. A gel or glass is characterized by transient networks that change the dynamic properties of the system. Due to the network structure the motion of the particles slows down significantly. Network formation can become enhanced in systems with long-ranged particle interactions; such systems are therefore more likely to build gel phases [111]. Another factor that favors gelation is branching. Recent studies of systems of dipolar dumbbells have shown that even a modest elongation of the particles leads to branching and, at very low temperatures, to gelation [24, 111]. Since our model allows the charges within the colloidal particles to fluctuate, the particles have some similarities with dumbbells, and branching may occur more likely than in point-dipole systems.

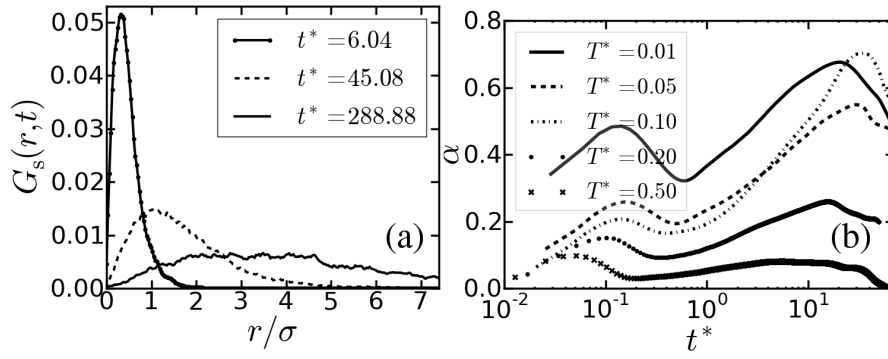


Figure 33: (a) Self part of the van-Hove function $G_s(r, t)$ as function of the distance and three times t^* at $\rho^* = 0.1$ and $T^* = 0.01$. (b) Non-gaussian parameter $\alpha(t)$ as function of the time at density $\rho^* = 0.1$ and different temperatures.

As an important indicator of anomalous dynamical behavior within the percolated phase we determine the MSD, introduced in Section 2.6.1 and defined by

$$\Delta \mathbf{r}^2(t) = \left\langle \frac{1}{N} \sum_{i=1}^N [\mathbf{r}_i(t) - \mathbf{r}_i(0)]^2 \right\rangle. \quad (4.1)$$

In gel-like systems the MSD shows a plateau at intermediate times between the regular ballistic and diffusive regime [108]. This slowing-down mechanism can be explained by particles trapped in transient networks [23].

In Figure 32 we plot the MSD of our system at $\rho^* = 0.1$ and $\rho^* = 0.5$ at different temperatures in a double-logarithmic representation. At small times all systems show regular ballistic behavior characterized by $\Delta \mathbf{r}^2(t) \propto t^2$. At very high temperatures ($T^* > 0.3$) this ballistic behavior changes directly into diffusive behavior $\Delta \mathbf{r}^2(t) \propto t$ (see Section 2.6.1 for a derivation of this behavior). At lower temperatures we observe (for both densities) deviations from this simple behavior, as seen in Figure 32(a) and (b). Specifically, the MSD of the dilute system [see Figure 32(a)] displays a time-dependence with exponent less than one at intermediate times ($t^* \sim 0.1 - 1$) for all temperatures $T^* < 0.25$. This implies that already the string formation occurring below the polymerization ($T_{\text{poly}}^* = 0.247$) somewhat slows down the dynamics. An even more pronounced slowing-down is seen at the temperatures $T^* = 0.10$ and $T^* = 0.05$, where the system is within the percolated phase ($T_{\text{perc}}^* = 0.137$). At the medium density $\rho^* = 0.5$ the effects in the afore-mentioned temperature range are less pronounced. However, by further cooling the denser system towards $T^* = 0.05$ we again observe a pronounced plateau in the MSD. This is even better revealed by the inset of Figure 32(b). The time range related to the trapping of the particles is almost two orders of magnitude larger than in the low-density case ($\rho^* = 0.1$).

Only at very long times the particles can escape their cages, yielding eventually a diffusive regime. Another interesting point concerns the “cage size”, that is, the typical length related to the plateau in the MSD. As seen from Figure 32(b) [and, less clearly, also from Figure 32(a)], this length is significantly smaller than one particle diameter ($\approx 10^{-2}\sigma$). Such small cage size is reminiscent of what one finds in various polymeric [13], dipolar [85], and glass-forming [13] systems. On the other hand, much larger cage sizes of the order of one particles diameter are observed in typical colloidal gels [140, 111].

The appearance of transient networks in our system is also reflected by the self-part of the van-Hove function [66], $G_s(r, t)$. In a purely diffusive or ballistic system, $G_s(r, t)$ is a gaussian function, see Section 2.6.2. Results for $G_s(r, t)$ are plotted in Figure 33(a), where we consider three typical times at $\rho^* = 0.1$. Deviations from the standard gaussian behavior are seen particularly at the small time $t^* \sim 6$ and intermediate time $t^* \sim 45$. In order to quantify these deviations we determine the parameter α defined by

$$\alpha(t) = \frac{\langle(\Delta r(t))^4\rangle}{3\langle(\Delta r(t))^2\rangle^2} - 1. \quad (4.2)$$

The function $\alpha(t)$ is zero in both, the ballistic and diffusive regime. In Figure 33(b) we plot $\alpha(t)$ at $\rho^* = 0.1$ and different temperatures. At the highest temperature considered ($T^* = 0.5$) the α parameter is very small, indicating that the van-Hove function is nearly gaussian at all times. Decreasing the temperature leads to an emergence of two peaks at small and large times. The peak at large times becomes particularly pronounced right below the percolation transition which takes place at $T_{\text{perc}}^* = 0.137$. In various recent simulation studies of aggregating systems [111, 54], such peaks in $\alpha(t)$ have been interpreted as presence of different “populations” of particles (*i.e.* as dynamic heterogeneities). As an attempt to identify such populations in the present system, we have calculated the distribution of squared displacements [132], $P(r^2, t)$ at fixed times. From this function one should be able to extract information about different populations, *i.e.*, if there exist different “typical” travel distances in the system. However, we did not find any significant behavior (such as a double-peak structure indicating presence of “slow” and “fast” particles) at the conditions considered.

To summarize our discussion about the appearance of gelation in the present (model) system, we note that there are some features pointing in this direction, whereas other are not. One main feature typical for gels is the presence of percolated and branched structures as seen in Figure 30(b) [and also later in Figure 34]. Moreover, particularly at intermediate densities we find that these structures lead to plateau-like behavior of the mean-squared displacement, accompanied by a peak of the alpha-parameter. However, the typical cage size of a gel is not observed in our system. Also, there is no evidence for dynamical

heterogeneities, and the observed structures are transient rather than stable (as it is the case, e.g., in gels of branched dendrimers). We therefore consider the present model involving short-ranged, fluctuating dipolar interactions as a system showing dynamic anomalies with weak hints pointing into a gel-like behavior.

4.2 ORDERED PHASES

At low temperatures and sufficiently high densities the dipole-like colloids start to build crystalline structures characterized by long-ranged positional ordering of the particles. The degree of translational order can be studied by various bond-order parameters. Here we focus on the hexagonal order parameter [40], introduced in Section 2.5.3, which reads for the hexagonal case

$$\Psi_6 = \left\langle \frac{1}{N_b} \left| \sum_{i=1}^{N_b} \exp(i6\theta_{ij}) \right| \right\rangle. \quad (4.3)$$

If each particle is surrounded by six nearest neighbours the order parameter Ψ_6 becomes one (hexagonal lattice (HL)), whereas in a homogeneous state Ψ_6 is zero.

In addition to positional order, the degree and type of global orientational order (if it occurs) is also of interest. For this purpose we have introduced in Section 2.5.3 the order parameter measuring the orientational order of a system. Recall, the first-rank orientational order measures the orientation with respect to the global director. The director is defined as the eigenvector corresponding to the largest eigenvalue of the matrix \mathbf{Q} (see Equation 2.141). This value is unity in a ferroelectric state and zero in an anti-ferroelectric or isotropic phase. The second-rank order parameter P_2 is defined as the largest eigenvalue of \mathbf{Q} , and describes the alignment of the particles without carrying the information of the direction. As we will show below, the present system has (only) a ferroelectric phase. Hence, we focus on the order parameter P_1 since P_2 shows less significant changes.

The transition into a ferroelectric state is characterized by an increase of the parameter P_1 from zero to one. The corresponding curves $P_1(T^*)$ turned out to be essentially independent of the system size (presumably due to the short-ranged character of the pair interactions in our model). We thus determine the ferroelectric transition from simulations with $N = 1024$. In addition to the system size, we investigate the impact of the geometry of the simulation box. To this end we implemented a variable box-length Monte-Carlo algorithm [145]. To preserve a canonical ensemble, the area of the simulation box was kept constant. We also performed a few simulations with a fixed, rectangular shape of the simulation box. However, the order parameter turned out to be robust against all these tests.

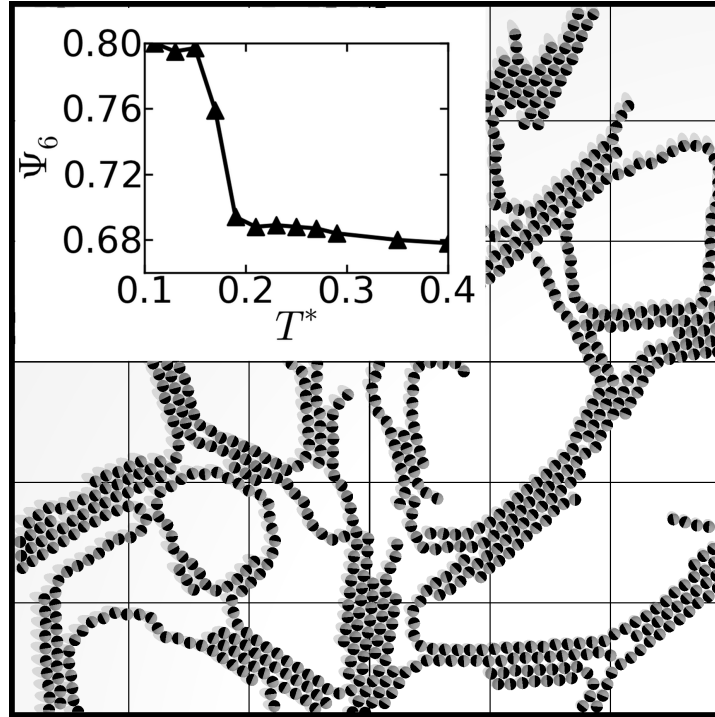


Figure 34: Snapshot at $\rho^* = 0.3$ and $T^* = 0.13$ (within the percolated phase). The inset shows the order parameter Ψ_6 as function of T^* .

4.2.1 Low densities

As discussed in Section 4.1, the regime of low and medium densities is characterized by a polymerization and percolation transition. To complete the picture, we now discuss the corresponding behavior of the orientational and translational order parameters. As an example we consider the density $\rho^* = 0.3$. In Figure 34, we present a snapshot illustrating the structure of the system at temperature $T^* = 0.13$, which is slightly below the percolation temperature (see Figure 29). As expected, one observes system-spanning clusters consisting of dipolar chains. Interestingly, however, some of these chains are merged into “bundles” characterized by a parallel arrangement of pieces of chains. Within these bundles, neighbouring chains are shifted relative to one another by half a particle diameter. These arrangements correspond to an energetically highly favorable situation, as reflected by the sketch in the last row in Figure 5. Having in mind that the present colloidal particles lack of any *isotropic* attractive interactions, we conclude that the bundle formation observed in Figure 34 is driven by the attractive, lateral interactions between (pieces of) dipolar chains. It is clear that these lateral interactions and the resulting bundles also favor branching and thus, gel-like behavior, as reflected e. g. by the MSD (see Figure 32(b)). A further consequence of the pronounced local ordering is that the bundle structures (such as those in Figure 34 for $\rho^* = 0.3$) are characterized by relatively large values of the hexagonal order

parameter, Ψ_6 . The temperature dependence of Ψ_6 is plotted in the inset of Figure 34. From the inflection point of Ψ_6 we can determine a hexagonal transition temperature at $T_{\text{hex}}^* = 0.174$, which is slightly higher than the percolation temperature $T_{\text{perc}}^* = 0.161$. We note, however, that the system at temperatures $T^* < T_{\text{hex}}^*$ is not a solid; rather it remains to be disordered down to the lowest temperature considered. Also, there is (obviously) no global orientational order, that is, $P_1 \sim 0$. Similar behavior of Ψ_6 and P_1 is found at other densities in the range $\rho^* < 0.4$.

We note that bundle formation has also been observed in 2D systems of dipolar particles with additional Yukawa interaction [187] where, however, the density was higher. In fact, our model prefers bundle formation as compared to a system of true dipolar spheres, where the chain-chain interaction is considerably weaker. This becomes clear from Figure 5 (bottom), where we compare the energy of hexagonal-like configurations in the two types of models. As a consequence, our model supports bundle formation already at lower densities. Prominent real systems where pronounced bundling and accompanying local hexagonal order occurs, are ferro-colloids in external magnetic fields [68], but also polarizable colloids [102] and Janus colloids [47] in electric fields.

4.2.2 High densities

In the density range discussed so far, hexagonal ordering occurs only locally (i. e., within bundles). This changes at densities $\rho^* \geq 0.6$ where we find, at sufficiently low temperatures, the formation of crystalline structures characterized by long-range positional, hexagonal order. The change from the isotropic high-temperature into the hexagonal low-temperature state is illustrated in Figure 35, where we present various snapshots of systems at the representative density $\rho^* = 0.9$. At the lowest temperature considered, the system is nearly close-packed apart from small defects.

The hexagonal translational structure is, in fact, expected in view of the behavior of the pure HS system underlying our model. Note, however, that the HS systems freezes only at a density [80] $\rho^* \approx 0.91$, that is, much later than the present system. This is consistent with our findings in the previous paragraph, according to which the dipole-like interactions tend to stabilize the hexagonal-like ordering at lower densities (as compared to HS).

A further, and much more dramatic, consequence of the dipole-like interactions is that the translational ordering at high densities is accompanied by long-ranged ferroelectric order. This can be directly seen from the (low-temperature-) snapshot in Figure 35(a) and Figure 35(b), and, more quantitatively, from the behavior of the parameters Ψ_6 and P_1 . In Figure 36 we have plotted the functions $\Psi_6(T^*)$

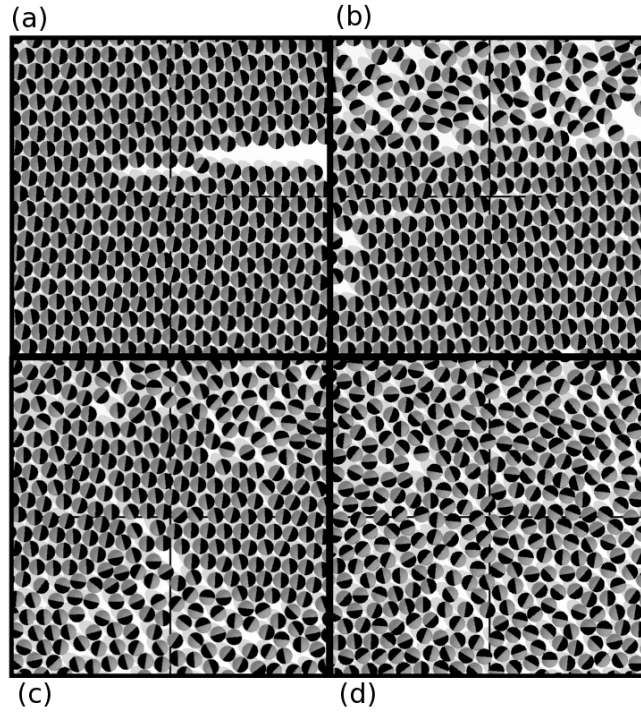


Figure 35: Snapshots at $\rho^* = 0.9$ at different temperatures illustrating the melting transition. The reduced temperature is $T^* = 0.2$ in (a), $T^* = 0.3$ in (b), $T^* = 0.4$ in (c) and $T^* = 0.5$ in (d).

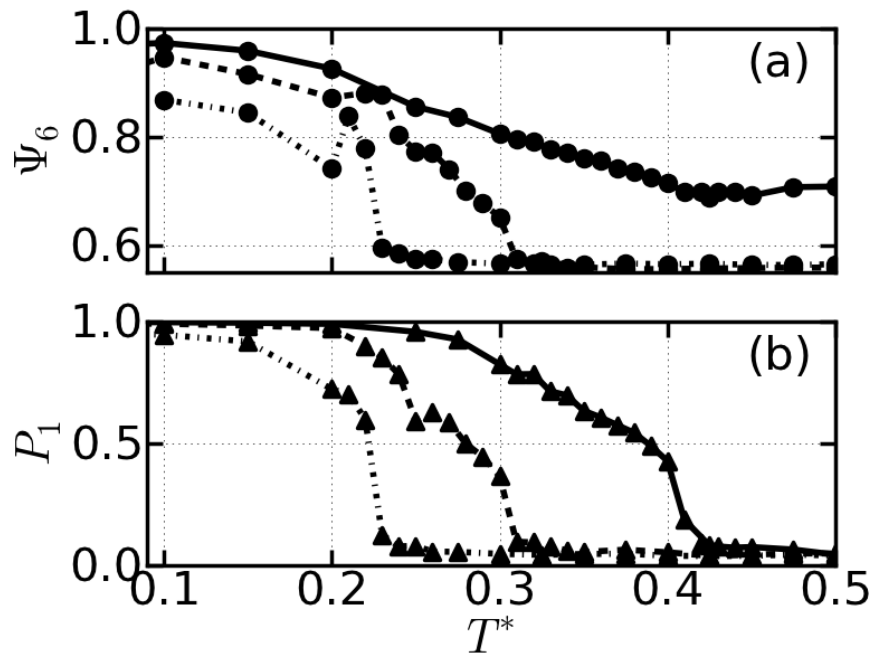


Figure 36: (a) Order parameters Ψ_6 and (b) P_1 at densities $\rho^* = 0.9$ (straight line), 0.8 (dashed line) and 0.6 (dotted line).

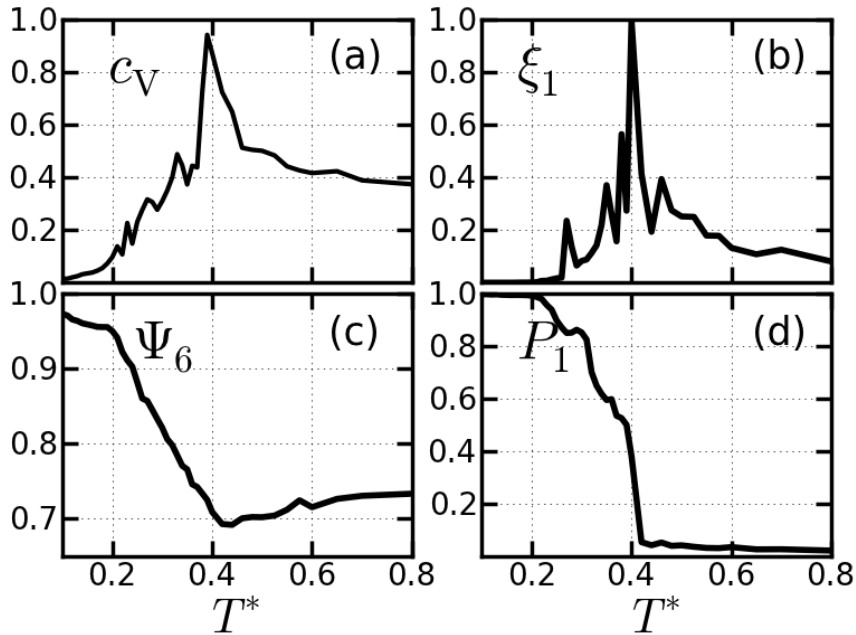


Figure 37: Transition from isotropic fluid to ordered phase at density $\rho^* = 0.9$. In (a) we plot the specific heat c_V , in (b) the fluctuations of the orientational order ξ_1 . The order parameters at the transition are shown in (c) Ψ_6 and (d) P_1 .

and $P_1(T^*)$ for three (large) values of ρ^* . In all cases, one observes a sudden, pronounced increase of P_1 upon lowering the temperature from the isotropic high-temperature state ($P_1 \sim 0.0$). Moreover, the temperature where P_1 starts to deviate from zero, coincides with the temperature where the parameter Ψ_6 increases significantly from the smaller (and essentially T^* -independent) values characterizing the high-temperature state. In fact, the data in Figure 36 suggest that the order parameters increase from their high- T^* values nearly continuously, indicating presence of a second-order (or, at the least, weak first-order) phase transition. Here, we did not attempt to clarify that issue systematically. We note, however, that the coupled hexagonal/ferroelectric transition is accompanied by significant fluctuations. This is illustrated in Figure 37, where we plot the functions $\Psi_6(T^*)$ and $P_1(T^*)$ together with the specific heat c_V (measuring fluctuations of the (potential) energy), and the quantity $\xi_1 = \langle P_1^2 \rangle - \langle P_1 \rangle^2$ (the latter has been normalized by its maximum value since the absolute values are rather small). Both quantities display a pronounced peak at the temperature related to the onset of the hexagonal/ferroelectric ordering. Similar behavior is found at other values of ρ^* in the high-density regime, with the peak heights in c_V and ξ_1 becoming less pronounced, the smaller ρ^* .

The appearance of long-ranged ferroelectric order in our model is in marked contrast to what is known about the behavior of true

dipolar spheres in 2D. In fact, while model systems like dipolar hard and soft spheres do display ferroelectric order in the 3D case, MC simulations of corresponding 2D systems rather reveal frustrated structures characterized by large domains of local ferroelectric order, but no long-range order [190]. The same conclusion emerged from (MD) simulations of confined, slab-like dipolar systems where the long-ranged ordering is lost upon lowering the film thickness towards the 2D limit [167]. Clearly, an important technical issue particularly at very high densities and low temperatures concerns the influence of the system size considered in the simulations. Indeed, for true dipolar systems it is well known that a too small simulations system can stabilize ferroelectric ordering under conditions, where simulations with larger systems would just reveal large domains. To check this point, we have additionally run some simulations with $N = 2000 - 4000$ particles. Additionally we have investigated the decay behavior of the two particle correlation function of the dipolar vectors, that is, the function

$$g_{110}(r) = \frac{1}{N\rho} \left\langle \sum_i \sum_{j \neq i} \delta(r - r_{ij}) \hat{\mu}_i \hat{\mu}_j \right\rangle, \quad (4.4)$$

where $\hat{\mu}_i$ is a unit vector. In the limit of large r , this function should saturate to a finite value determined by the order parameter P_1 [189]. In our case, for systems of $N = 1500$, the function $g_{110}(r)$ still revealed additional peaks of the correlation function at half length of the simulation box. In Figure 38 we show $g_{110}(r)$ at $\rho^* = 0.9$ and $T^* = 0.2$ for $N = 2500$ particles. The particle density corresponds to a simulation box of length $L \approx 52$. After a distance of $r = 20\sigma$ there are only weak correlations present, whereas the correlation converges against a constant value. We thus conclude that the system size of $N \sim 2500$ is sufficient to check for true long-range ferroelectric order. Inspecting snapshots, it turns out that the larger systems generally display more defects. However, on the whole the combined hexagonal and ferroelectric ordering remains.

4.3 SUMMARY

We have used DMD computer simulations to study a system of nanoparticles with dipole-like interactions in two dimensions. A prerequisite of the DMD technique (and the main reason for its computational efficiency), are discontinuous, short-ranged potentials. To this end we have approximated the true dipole-dipole interaction by a short-ranged three-step potential suggested in an earlier study of a corresponding 3D system [56]. Based on that model, which mimics the directional dependence of the dipolar interactions on short length scales, we were able to study a wide range of densities and temperatures. An overview of the equilibrium behavior, that is, a rough (yet

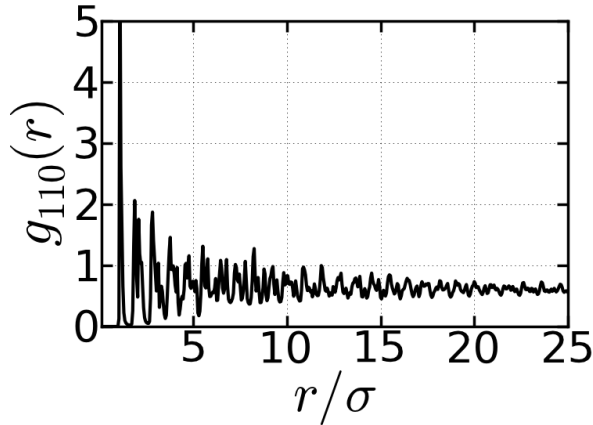


Figure 38: We show the two particle correlation function of the dipole vector $g_{110}(r)$ at a system size of $N = 2500$.

not complete) phase diagram, is given in Figure 39. Apart from a homogeneous, isotropic high-temperature phase (I), we find a polymerized ("string") fluid (II), a percolated phase (III), and a hexagonal, ferroelectric crystal (IV). An open point, which was beyond the scope of the present study, concerns the transition *between* the percolated and the crystal phase, as well as the occurrence of glassy phases. We also note that we have seen no evidence for a gas-liquid transition within the fluid phase, consistent with the behavior of the corresponding 3D model [56] and also with that of true dipolar hard or soft spheres in two and three dimensions [161, 188]. On the other hand, the absence of gas-liquid condensation is in contrast to many other aggregating systems such as, e.g. Janus particles, which display a combined condensation-micellisation transition [147]. Similar models with short-ranged potentials, such as patchy particles, also show a gas-liquid separation provided the number of patches per particle is sufficient [20, 21].

As described in the previous sections, all lines in Figure 39 have been defined via a thorough analysis of suitable order parameters. In particular, to define the polymerization line we used the so-called degree of polymerization (measuring the number of particles involved in clusters), which showed almost no finite-size effects (contrary to the specific heat). Interestingly, the resulting line agrees quite well with a corresponding result from a recent integral equation study of 2D systems of true dipoles [104]. Moreover, our polymerization temperatures are very close to those found in the 3D version of the present model [56], although the latter (DMD) study used a somewhat different order parameter, namely a strong increase of the average cluster size. Less agreement is found with respect to the percolation which occurs in both, the 3D [56] and the 2D system, at temperatures below the polymerization. We have located the percolation threshold in

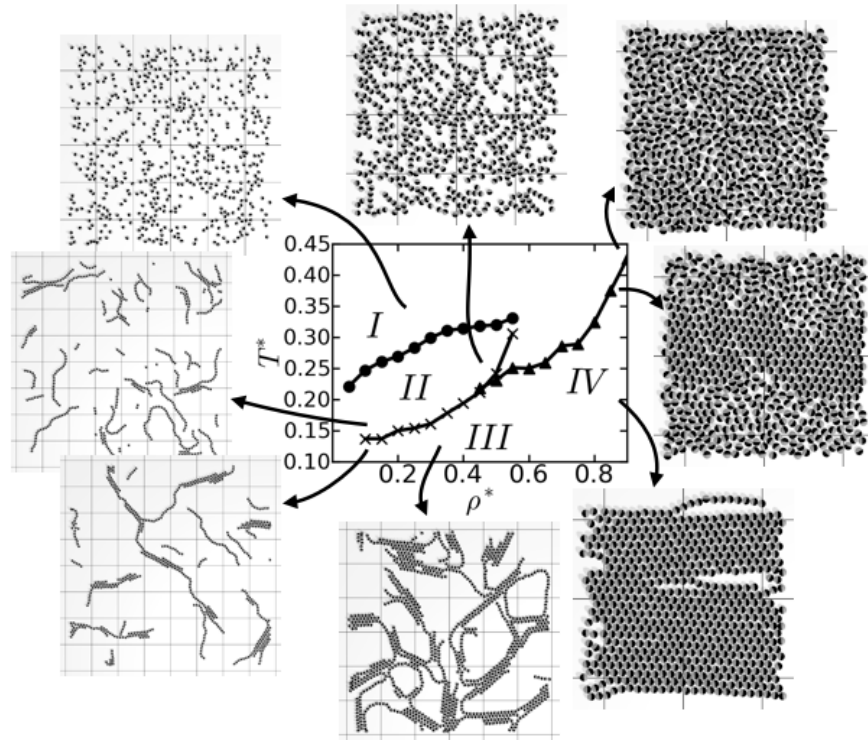


Figure 39: Phase diagram involving all transition lines determined in this work together with corresponding snapshots. The labels I, II, III, and IV refer to the isotropic fluid, the polymerized fluid, the percolated phase, and the ferroelectric crystal, respectively. We have not attempted to determine the transition between percolated fluid and the crystal at low temperatures.

the "traditional" way, that is, by monitoring the percolation probability. The resulting percolation temperatures are significantly lower than those in the 3D model. We note however, that [56] used a different definition of percolation such that the quantitative comparison with our data has to be considered with care. We would like to note that in the case of true dipoles in 2D ring formation is observed in the polymerized fluid phase [101], contrary to the 3D case, where this effect is less pronounced. A similar system where such a behavior can be observed is a mixture of patchy particles, with 2 and 3 patches. In these systems rings and inter-cluster bonding is also very pronounced, which is due to particles with 3 patches building connections [159]. In our system, however, the formation of rings is relatively weak in the polymerized fluid phase.

Given the preference of head-to-tail configurations and thus, chain formation, in our model, the very appearance of polymerization and percolation at low temperatures and densities is clearly expected. A less explored question concerns the corresponding dynamics. While systems of true dipolar hard or soft spheres (in zero field) display normal dynamics despite pronounced chain formation [85], a recent

MD study of dipolar dumbbells [111] revealed anomalous, gel-like dynamics accompanying the formation of branched chains and networks. Our model bears some similarity with the dumbbells insofar as the "dipoles" in our particles consist of two "charges" whose position can fluctuate. Motivated by this fact we have investigated the present system via various time-dependent (single-particle) quantities. For some state points deep within the percolated phase, we do indeed find features reminiscent of gels such as plateau-like behavior of the mean-squared displacement, accompanied by a peak of the alpha-parameter. The picture emerging from these measures (and from a corresponding structural analysis) is that the particles form transient networks consisting of percolated chains and bundles thereof. Of course, network formation also occurs in systems of true dipoles [161], including the dipolar dumbbells studied in [111]. However, compared to the dumbbells it seems that the networks in our case are less stable. One factor might be that the interactions in [111] are of coulombic and thus, long-ranged nature, a factor which tends to stabilize the networks. Concerning the dynamics, we note that the present system shows no evidence of dynamical heterogeneities, and that the cage sizes extractable from the MSD are extremely small. Taken altogether, we conclude that the dynamics do possess anomalous features, but that there is no clear gel "phase" such as in systems of dipolar dumbbells [111] and patchy particles [108, 140].

Finally, we have investigated the crystallization. As expected in view of the 2D character of our model, the particles form a hexagonal lattice. Interestingly, these solid-like structures appear already at densities far below the freezing density of the corresponding hard disk fluid. Moreover, the ordering into a hexagonal lattice goes together with the onset of long-ranged ferroelectric order. In this respect, our model behaves fundamentally different from 2D systems of true dipolar (hard or soft) spheres where, at the most, large ferroelectric domains (rather than true global polarization) are observed. In our view, the main reason for this difference is that the present model slightly prefers (relative to the true dipolar case) arrangements of parallel oriented, shifted chains.

Taken altogether, our study reveals a complex static and dynamic behavior of the colloidal model system under consideration. Clearly, the short-ranged nature of our model is an approximation, when one thinks about true dipoles; we note however, that in a true colloidal system involving particles with charges, the effective range of the interaction can be tuned by parameters such as salt, pH, or concentrations of ionic adsorbing species. From our view, one particularly interesting (and novel) result is the gel-like behavior found in the percolated phase. Indeed, the unusual dynamics observed, e. g., in the mean-squared displacement (see Figure 32) suggests a non-trivial, non-linear behavior also in rheological properties such as the shear vis-

cosity and, more generally, the mechanical response of the material to external stress. This is clearly an aspect which deserves further attention and could also be studied via the DMD method. Moreover, given the overwhelming variety of colloidal particles being synthesized with increasing complexity and precision [95], it would be very interesting to extend the present study towards more complex particles which have, e. g., quadrupolar character [48].

5

NETWORK FORMATION IN SYSTEM OF INDUCED DIPOLES IN TWO DIMENSIONS

In the previous Chapter 4 we investigated a sketch of the phase diagram of dipole-like colloids in two dimensions. One very interesting phenomenon we identified is the gel-like behavior of the percolated phase. Due to the branching of the particle model we observe large networks that slow down the dynamics of the system. This subdiffusive behavior is typical for gels and glassy systems [23]. In the present chapter we are now focusing on the network formation in dipolar systems in two dimensions. Contrary to the two previous chapters where the dipoles were free to rotate in three dimensions (Chapter 3) and in two dimensions (Chapter 4), we are fixing them in this chapter to one dimension. This can be achieved by inducing dipoles via an external field.

We are motivated and inspired by current experimental work in designing complex colloidal particles that assemble into two-dimensional networks by applying a uni-axial external field [48]. These particles show the fascinating phenomenon to build structures parallel and perpendicular to the external field. We are only aware of one similar phenomenon that can be observed by using binary mixtures of particles with different dielectric properties [60, 52]. In the present chapter we study the static and dynamic properties of colloidal networks by employing MC and MD simulations.

5.1 BACKGROUND

5.1.1 *Experimental background*

Recent experiments in the research group of Prof. Velev [48] have designed a novel type of colloidal particles. Through Glancing Angle Deposition a single gold patch is placed on polystyrene particles of diameter $5.0 \mu\text{m}$. By adjusting the angle the gold patch can cover 5 – 50% of the particle surface. Then, an AC-field of 0.5 – 1000 kHz is applied with a strength of $\sim 200 \text{ Vcm}^{-1}$ to these particles. The external field induces a dipole moment in the polystyrene particle. The

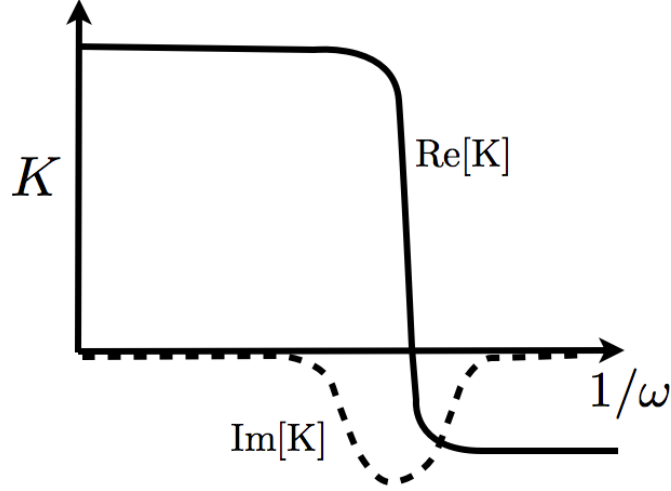


Figure 40: Sketch of the real part and imaginary part of the Clausius-Mossotti relation as function of the frequency of the external field.

Clausius-Mossotti relation describes the permittivity of two different media (1 and 2) according to

$$K(\omega) = \frac{\epsilon_2^* - \epsilon_1^*}{\epsilon_2^* + 2\epsilon_1^*} \quad (5.1)$$

with the complex permittivities

$$\epsilon^* = \epsilon - i\frac{\sigma}{\omega}, \quad (5.2)$$

where ω is the frequency of the external field and σ the conductivity. In general, the effective polarizability of a dielectric particle in a solvent is given by the real part of the Clausius-Mossotti relation, K , by [84]

$$\Re|K| = \frac{\epsilon_2 - \epsilon_1}{\epsilon_2 + 2\epsilon_1} + \frac{3(\epsilon_1\sigma_2 - \epsilon_2\sigma_1)}{\tau_{MW}(\sigma_2 + 2\sigma_1)^2(1 + \omega^2\tau_{MW}^2)}. \quad (5.3)$$

In this equation ϵ_1 (ϵ_2) is the dielectric permittivity of the media (particle) and σ_1 (σ_2) is the conductivity of the media (particle) [19, 96]. The quantity τ_{MW} denotes the Maxwell-Wagner relaxation time defined by

$$\tau_{MW} = \frac{\epsilon_2 + \epsilon_1}{\sigma_2 + 2\sigma_1} \quad (5.4)$$

which describes the response time of the system to the external field. The polarizability in Equation 5.3 is a function of the frequency of the external field, ω . A typical behavior of this quantity is sketched in Figure 40. The polarizability changes its sign from positive to negative by increasing the frequency of the external field. This effect is due to the ionic layer around each particle. The ionic polarizability disappears at high frequencies and the polarizability of the dielectric

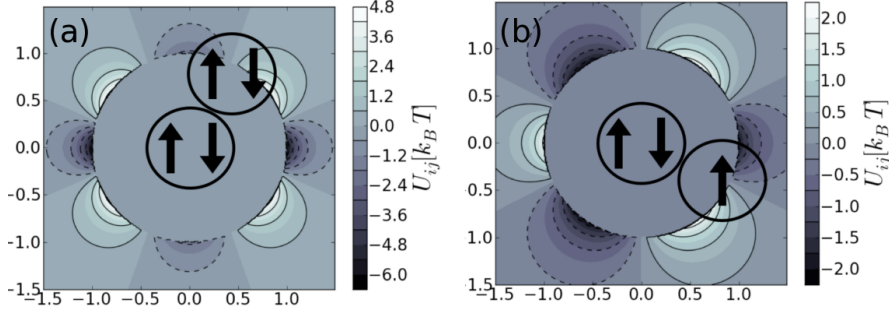


Figure 41: (a) Interaction potential of two DID. Distances on the x-y axis are indicated in σ . In (b) we show the interaction of one DID with one ID.

particle switches its sign from positive to negative. This relation makes these particles controllable by an external field. The particles used in [48] have a crossover frequency of about 200kHz. The gold patch has no frequency dependent polarizability since it is strongly polarized at any frequency. The materials and the size of the patch were chosen such that the polarizability of the patch and the particle are of similar magnitude and produce induced dipoles of similar strength. We finally end up with polystyrene particles with two induced dipole moments, one pointing into the external field direction, originating from the dielectric part, and one pointing opposite to the field which is induced in the gold patch. These particles are solved in Milli-Q ultrapure water between two glass plates and the resulting system is quasi two-dimensional. The assembly of these particles can be studied by optical microscopy.

Another important fact is that during the synthesizing process a certain degree of imperfection is involved. Some of the polystyrene particles are coated with no or with a significant lower amount of gold. It can be estimated that only 80 – 90% of the particles actually have a gold patch. After applying the field it takes 2-5 s for the particles to assemble. COMSOL, (Burlington, MA) multiphysics modeling package, was used to perform electrostatic simulations to estimate the potential energy of different configurations of two such single-patch particles. At a temperature of 300 K the potential energy difference of two single-patch particles aligned perpendicular to the field, the most favorable configuration, and parallel to the field is $\Delta U \approx 6 k_B T$. In our theoretical investigation we choose a value close to the experimental ones. The concentration of particles with gold patch in the real experiment is however significantly higher. The reason is that in our simulations a large amount of particles with two induced dipoles requires much longer simulation times while not providing significant additional insights.

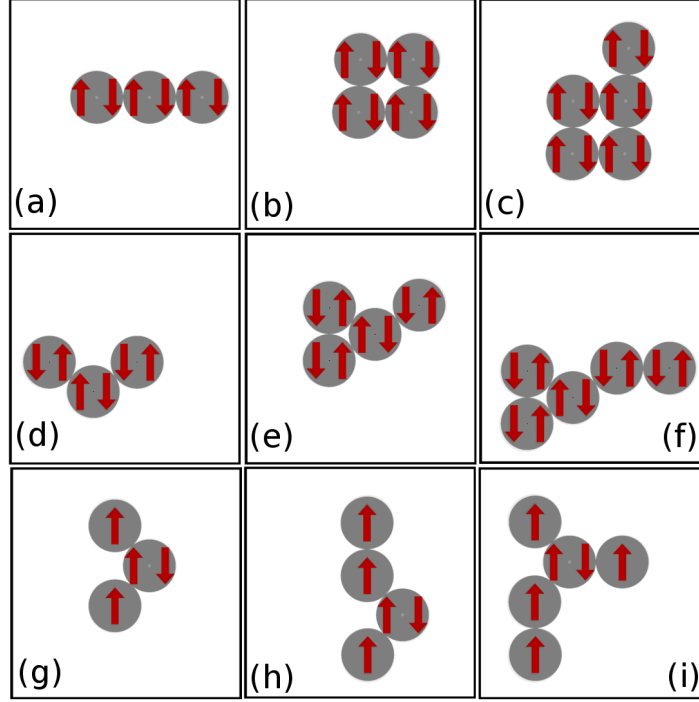


Figure 42: In (a)-(c) we show results from ground-state calculations from 2-5 DID pointing into the same direction at a temperature close to zero. In (d)-(f) we show ground-state structures of one DID together with 2-4 DID pointing into the opposite direction. (d)-(f) show the ground-state structure of one DID together with 2-4 ID.

5.1.2 Model

To model such particles in computer simulations we choose hard-spheres of diameter σ with embedded and induced dipole moments confined to two dimensions. The dipole moments are fixed in the external field direction. We assume that due to the imperfections it is certainly realistic to study a mixture of two different types of particles, the first containing only one dipole moment placed in the particle center and pointing into the field direction, the second type contains two dipole moments, where the first (second) is placed with a offset of $+\delta/2$ ($-\delta/2$) from the particle center. Throughout this study we set $\delta = 0.5\sigma$. One induced dipole is pointing into the field direction, whereas the other is pointing opposite to it and we decide randomly if the left (right) dipole is pointing into (opposed to) the field direction. The dipoles interact via the regular dipole-dipole interaction (Equation 2.2) and we handle the long range interactions via the Ewald summation technique (see Section 2.4.7.1 for further details). We employ Monte-Carlo simulations in the canonical ensemble, with 256,576,900 particles and $T^* = 1/(\mu^*)^2$, $(\mu^*)^2 = \mu^2/k_B T \sigma^3$. We set $\mu^* = 1$ and vary the temperature T^* to control the coupling strength between the dipoles.

To illustrate the interaction between the different particle types we plot the potential between two DID in Figure 41(a) and between one ID and one DID in Figure 41(b). Two DID display a strong attraction perpendicular to the field but also a weak attraction parallel to it. The character of the potential between two DID can be influenced by our parameter δ which separates both dipoles within the HS. After choosing the value $\delta = 0.5$, for which we obtained structures similar to the experimental snapshots we did not further investigate the influence of this parameter systematically. The interaction between ID and DID show a triangular character with three attractive spots, one emerging from the side-to-side configuration and the other two emerging from a shifted chain configuration. We see from these plots that the interaction of DID is almost three times stronger than between ID (which is $U_{ij} = 2$ in units of $k_B T$) and the interaction between DID and ID is of similar strength compared to ID-ID. Since the orientation of the DID with respect to the field is random, in the experiment as well as in our simulation, there is a third possibility of interactions. One DID interacts with another DID that has the induced dipoles pointing into the opposite direction. The resulting potential is exactly the same as for two DID pointing into the same direction, see Figure 41, but with opposite sign. We thus obtain the same potential as in Figure 41(a) but with attraction and repulsion exchanged. We can read from Figure 41(a) that the difference between the configuration of two DID parallel and perpendicular to the field is $\Delta U \approx 4 - 5 k_B T$, which corresponds closely to the value computed for the experimental particles ($\Delta U \approx 6 k_B T$). In Figure 44(a)-(c) and (d)-(f) we show results of ground-state calculations of our model system. We used simulated annealing (similar to the strategy in [89]) to obtain the structures of 3-5 particles at temperatures approximately zero. The simulated annealing is based on a standard Metropolis scheme where, however, T is lowered to zero step by step. By successively decreasing the temperature we reach finally the ground-state structure. To check if we really found the ground-state we run several independent simulations to control if the final structures were identical.

In Figure 42 we see that three DID assemble perpendicular to the field (a), four DID in a square-ordered structure (b) and the fifth particles connects to the cluster in the field direction (c). The behavior reveals a complex assembly of the DID, where a competition between chaining (3 particles) and packed structures (4 and 5 particles) is obvious. In Figure 42(d)-(f) we show the case of different orientations of one DID with 2-3 DID pointing into the opposite direction. We obtain a shifted chain-like behavior perpendicular to the field. In Figure 42(g)-(i) we illustrate the assembly of one DID and 2-4 ID to reveal the structure of mixing these particles. Two ID connect to the DID diagonally to the external field, which becomes clear by considering the potential plot in Figure 41(b). The chaining into

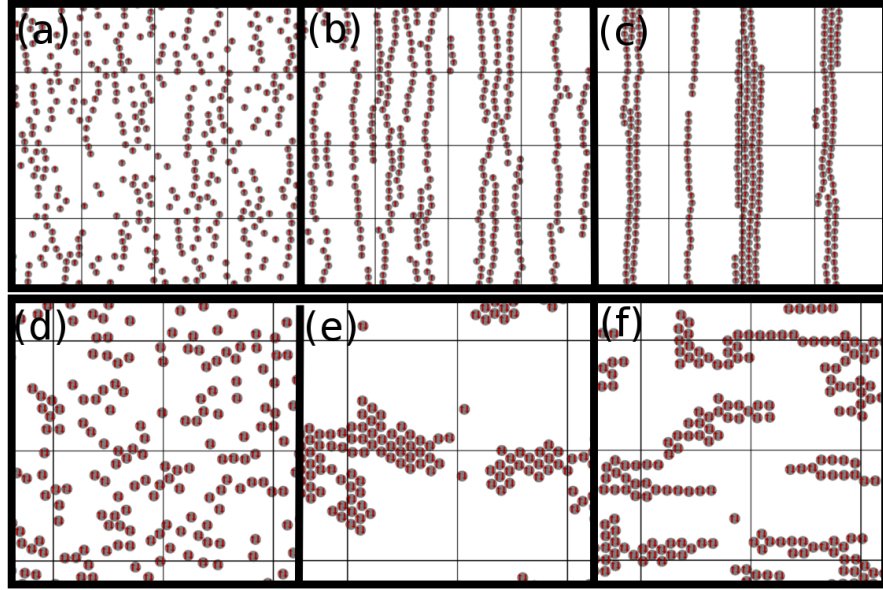


Figure 43: (a)-(c) we show snapshots of an one-component system of ID at temperatures $T^* = 0.75, 0.25, 0.1$ from left to right, respectively. The lower snapshots show a system of DID at $T^* = 1.5, 0.75, 0.5$ from (d) to (f).

the field is more favorable for 3 ID, whereas the fourth ID connects perpendicular to the field to the DID, forming a Y-connection between the ID. For the system containing only ID we show no results since the ground-states reveal the expected chaining behavior at very low temperatures.

5.2 ONE-COMPONENT SYSTEM

In Figure 43(a)-(c) we show snapshots of a one-component ID system. At finite temperatures we find for the one-component systems strong chain formation into the field direction of a system of only ID which was observed in experiments [173]. In our simulations we observe chains longer than half the length of the simulation box at $T^* \leq 0.5$. Lowering the temperature leads to bundle formation, what was also found recently in experiments with magnetic dipoles [68]. The DID start to form structures at higher temperatures ($T^* \leq 0.75$) since the displaced dipoles can come closer than in ID at the side-to-side configurations, see Figure 43(d)-(f). The clusters have a preferential orientation perpendicular to the field, however, the structures are much more packed than in the ID case. The effect of randomly choosing the orientation of the DID can also be observed. We find shifted chains and Y-connections perpendicular to the field, emerging from neighbouring DID with opposite orientation. This behavior is expected from our ground-state calculations in Figure 42(a)-(c). Only short chains are present and already a few particles build a compact cluster. Packed

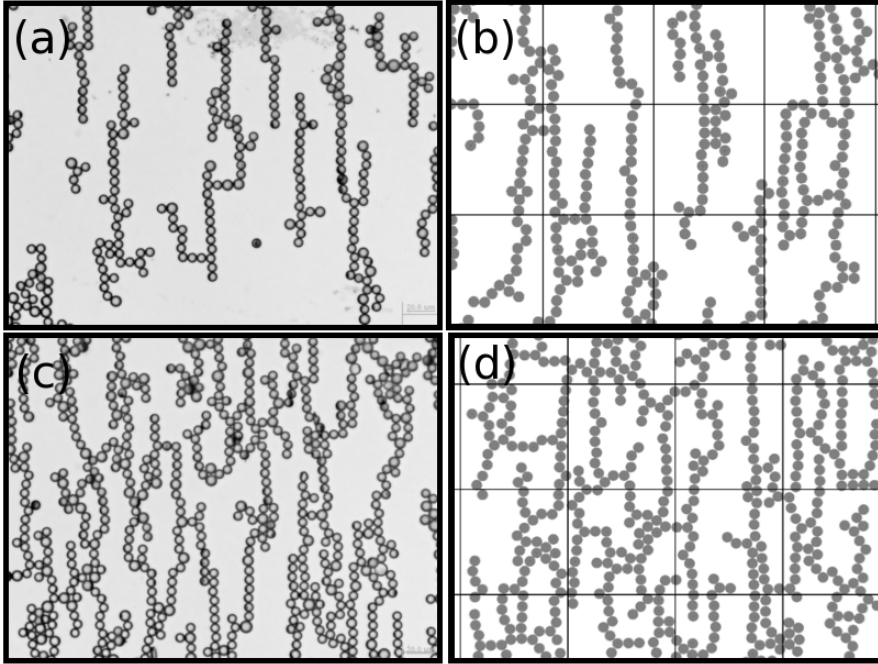


Figure 44: Pictures (a) and (c) show experimental snapshots according to the setup and particle interactions described in the text. We compare them to simulation snapshots at $T^* = 0.15$ and at $c_{\text{DID}} = 0.25, \rho^* = 0.25$ in (b) and at $c_{\text{BL}} = 0.30, \rho^* = 0.4$ in (d).

structures are also found for true quadrupolar particles [172]. The equilibration problem due to the strong dipolar interaction of the DID becomes clear by comparing Figure 43(e) and (f). Although in the latter snapshot the temperature is lower ($T^* = 0.50$) than in Figure 43(e) ($T^* = 0.75$) the clusters are less compact. This is a consequence of sampling difficulties of the one-component DID system at low temperatures. However, we are focusing on mixtures of ID and DID where these sampling difficulties are less pronounced and we detected no problems in equilibrating mixed systems.

5.3 MIXTURES OF DID AND ID

Of greater interest is the situation of mixtures of ID and DID. This setting is realistic due to the already mentioned imperfections during the synthesizing process and can also be realized by adding ID to a solution of DID. In our simulations this is achieved by randomly switching the desired amount of ID into DID and also by randomly choosing their orientation with respect to the field ($\uparrow\downarrow$ or $\downarrow\uparrow$ where the field is \uparrow). In Figure 44 we compare experimental snapshots with our model as described above.

In the simulation snapshot of Figure 44(b) the concentration of DID is at $c_{\text{DID}} = 0.25$ and the total density at $\rho^* = 0.25$. The experimental structures are approximately reproduced, including long chains into

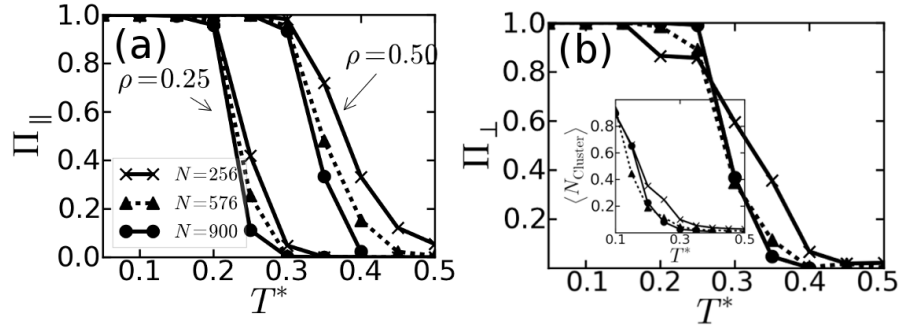


Figure 45: Percolation parallel to the field, $\Pi_{||}$, shown in (a) at $\rho^* = 0.25$ and $\rho^* = 0.5$. In (b) we plot the percolation perpendicular to the field, Π_{\perp} which occurs only at $\rho^* = 0.5$. Both plots are made at three different system sizes. The inset shows the normalized average cluster size, respectively.

the field direction (mainly build of ID) and shorter ones perpendicular to the field (only build of DID), as well as T-connections (originating from DID-DID interactions) and Y-connections (originating from DID-ID interaction) as depicted from our ground state considerations. At higher densities in Figure 44(d) ($\rho^* = 0.4$) we increased the amount of DID to $c_{\text{DID}} = 0.30$ and obtain also similar structures compared to the experiment. A closer inspection of the snapshots in Figure 44 and in the work [48] reveals that the ratio of T- to Y-connections is 2-3 times lower in our simulations, that display more Y-connections. The experimental patterns look overall more rigid than our simulation snapshots. We conclude that the reasons for these deviations are that the interaction strength is higher in the experiments and the amount of DID in our simulations is lower than in the experiments. Indeed, by increasing the amount of DID and decreasing the temperatures we obtain more similar structures. However, the simulations take considerably longer to equilibrate and we observe the effects of interest already at our setup.

5.3.1 Percolation

To investigate the possible networks and their properties we keep the concentration of DID constant at $c_{\text{DID}} = 0.25$ and we study the dependence on different dipole couplings at two representative densities, $\rho^* = 0.25$ and 0.5 . We aim at revealing the networks formed in these systems first from a stational point of view. For this purpose we study the percolation probability into the field direction ($\Pi_{||}$) and perpendicular to it (Π_{\perp}). The two types of particles give raise to patterns that assemble in both directions. This value is determined by the ensemble average of finding a cluster that reaches from one side of the simulation box to the opposite for each direction independently.

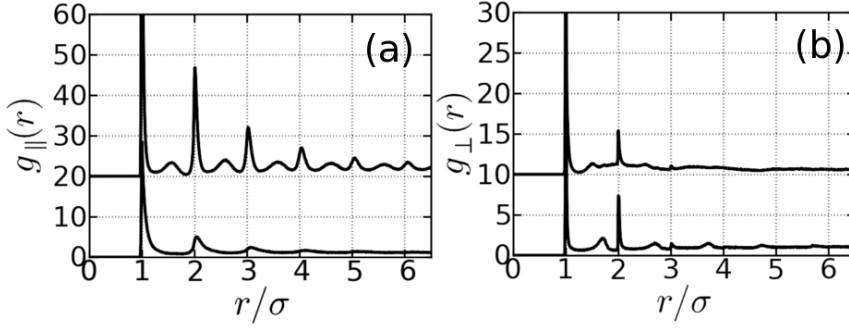


Figure 46: In (a) we show the pair correlation function parallel and in (b) perpendicular to the field at $T^* = 0.15$ (upper line) and at $T^* = 0.35$ (lower line).

In Figure 45(a) we show the percolation transition into the field direction which takes place at $\rho^* = 0.5$ at $T^* \approx 0.25$ and at $\rho^* = 0.25$ at $T^* \approx 0.25$. In Figure 45(b) we show the percolation transition perpendicular to the field which only takes place at $\rho^* = 0.5$. At $\rho^* = 0.25$ we find no clusters large enough perpendicular to the field. The concentration of DID is at $c_{\text{DID}} = 0.25$. Even by increasing significantly the c_{DID} the percolation perpendicular to the field does not take place. The total amount of particles is not large enough to induce this transition. We investigated the percolation probabilities at three different system sizes $N = 256, 576, 900$. The percolation probabilities at the considered system sizes intersect at approximately one temperature in all systems we studied. Thus, we assume that the percolation is not induced by the periodic boundary conditions or the limited system size. The inset of Figure 45(b) shows the average cluster size, $\langle N_{\text{Cluster}} \rangle$, also for three system sizes, normalized by the total particle number. There is a significant increase of the average cluster size after the percolation transition. Due to computational limits we were not able to study the cluster size distribution in more detail, in order to, e. g., reveal a power-law behavior.

The structural change before and after the percolation transition is illustrated in Figure 46 where we plot the pair correlation function at $\rho^* = 0.25$ and at the temperatures $T^* = 0.15$ and $T^* = 0.35$ parallel to the field, $g_{\parallel}(r)$, in (a) and perpendicular to the field, $g_{\perp}(r)$, in (b). In both plots the lower line corresponds to the pair correlation at $T^* = 0.35$ and the upper line, shifted by 10 (in (a)) and 20 (in (b)), respectively, corresponds to $T^* = 0.15$. We observe a very strong chaining into the field after the percolation transition indicated by pronounced peaks in the correlation function in Figure 46(a). There are weak correlations present between the main peaks. These peaks represent the triangular connections, where we find between two ID in the field direction one DID shifted to the right or left (compare Figure 42(f)). The correlation perpendicular to the field shows an inverse behavior. There are two pronounced peaks present at $T^* = 0.35$.

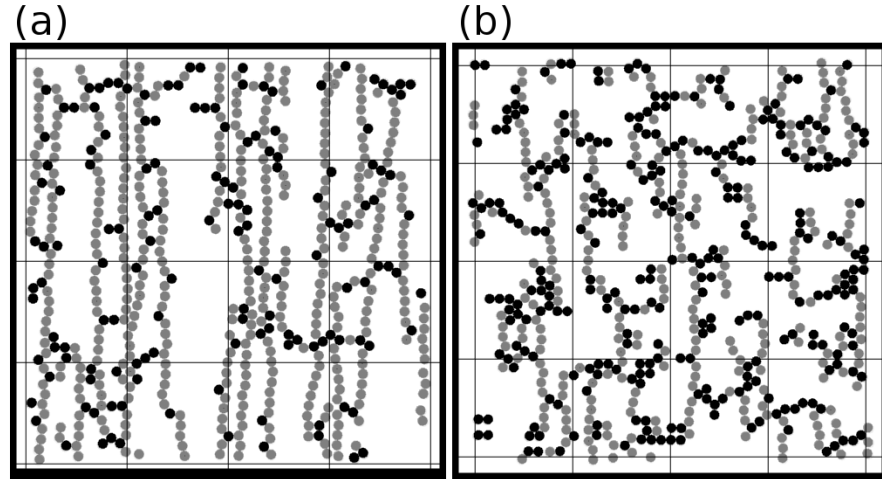


Figure 47: In (a) we show a snapshot of a mixture of ID and DID at $T^* = 0.15$, $\rho^* = 0.375$, $c_{\text{DID}} = 0.25$, and in (b) at $\rho^* = 0.35$ and $c_{\text{DID}} = 0.5$. The grey spheres indicate ID, whereas the black spheres are the DID.

These peaks become less pronounced at $T^* = 0.15$. The reason for this is that at higher temperatures the DID already build larger clusters due to their stronger interaction as compared to ID. By decreasing the temperature the ID start to form strong chains, preventing the DID to assemble into compact clusters. They form short connections between the long chains built by the ID (see snapshot in Figure 44(b) and (d)) resulting in a less pronounced pair correlation perpendicular to the field. Again, the triangular connections are the origin of the weak correlations between the main peaks.

In Figure 47 we show two snapshots of a mixture of ID and DID at different densities and compositions. In (a) the parameters are $T^* = 0.15$, $\rho^* = 0.375$, and $c_{\text{DID}} = 0.25$. One clearly sees how the DID build connections perpendicular to the field direction between the chains. Due to the low concentration of DID in the mixture they are well separated and build only short chains of the size of a few particles. Increasing the DID concentration to $c_{\text{DID}} = 0.5$ and at a slightly lower density $\rho^* = 0.35$ we observe more pronounced cluster formation of the DID. They still display the preferential orientation perpendicular to the field, however, they assemble into compact clusters, making to overall structure less “loose”.

Further, we studied the influence of the total particle density and composition of the mixture and how the percolation is affected. In Figure 48 we show the percolation probabilities at $T^* = 0.15$ for different compositions $c_{\text{DID}} = 0.10, 0.25, 0.50$ as a function of the total particle density $\rho^* = 0.1 - 0.5$. Already a small amount of DID, $c_{\text{DID}} = 0.10$, induces a percolation perpendicular to the field at $\rho^* \approx 0.45$, whereas the percolation probability parallel to the field takes place at $\rho^* \approx 0.1$. A larger amount of DID, $c_{\text{DID}} = 0.25$, induces the percolation

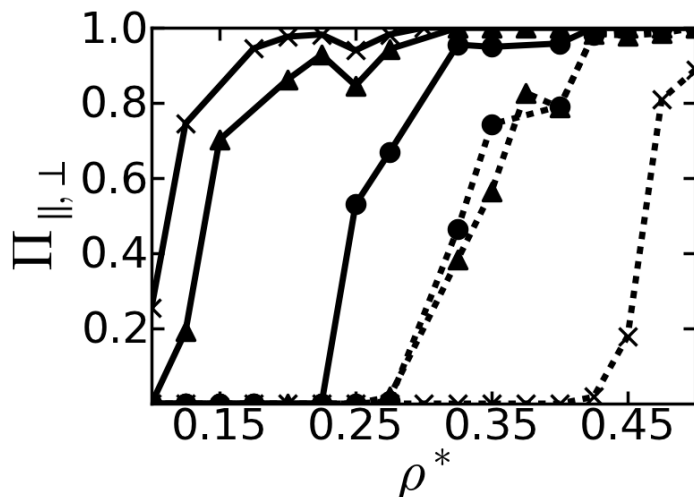


Figure 48: Percolation probability in field direction (solid lines) and perpendicular to it (dashed lines). The fraction of DID in the system is $c_{DID} = 0.5$ (circles), 0.25 (triangles) and 0.10 (crosses).

parallel to the field at $\rho^* \approx 0.15$ and perpendicular at $\rho^* \approx 0.30$. At the highest concentration considered $c_{DID} = 0.5$ we find the parallel percolation at $\rho^* \approx 0.25$ and perpendicular at $\rho^* \approx 0.2$. The DID are a strong disturbance that affects the chaining and bundle formation of one-component ID systems significantly.

5.3.2 Dynamics of the networks

We have determined the percolation transition and have shown that our model builds networks into two directions parallel and perpendicular to the external field. There is increasingly strong interest in gels of dipolar colloids without [111] and with external fields [73]. Percolation is a prerequisite of gelation but not sufficient. To elucidate this question we compute the MSD, defined in Section 2.6.1. We employ MD simulations with essentially the same model as in our MC simulations. We only substitute the HS potential by a very short ranged SS potential $U_{SS} \propto 1/r^{28}$, since regular MD can not handle step potentials. The MD simulations allow us to focus on the dynamics of the colloids. Details about the simulation method can be found in [46]. In Figure 49(a) and (b) we show the MSD at $\rho^* = 0.50$ (main plots) and at $\rho^* = 0.25$ (insets). The different lines correspond to different temperatures. Parallel and perpendicular to the field we obtain the expected ballistic behavior at small times and the diffusive regime at large times (indicated by the straight dashed lines). At $T^* = 0.15$ which is below the percolation transition, we observe a significant slowing down of the dynamics, which is clearly more pronounced in the direction perpendicular to the field. We find indeed a pronounced

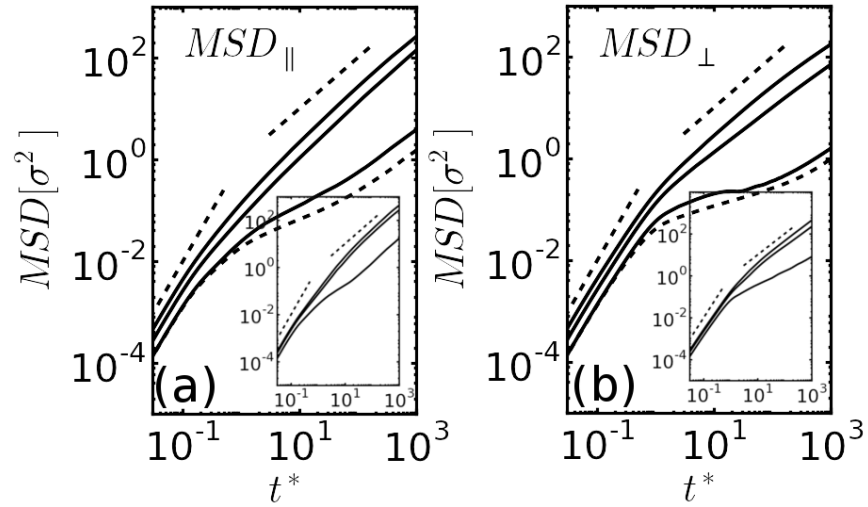


Figure 49: MSD at $\rho^* = 0.50$ parallel (a) and perpendicular (b) to the field. The three solid lines correspond to to $T^* = 0.5, 0.3, 0.15$, from top to bottom. The lowermost dashed line shows BD simulations at $T^* = 0.15$. The inset show the MSD at $\rho^* = 0.25$, respectively.

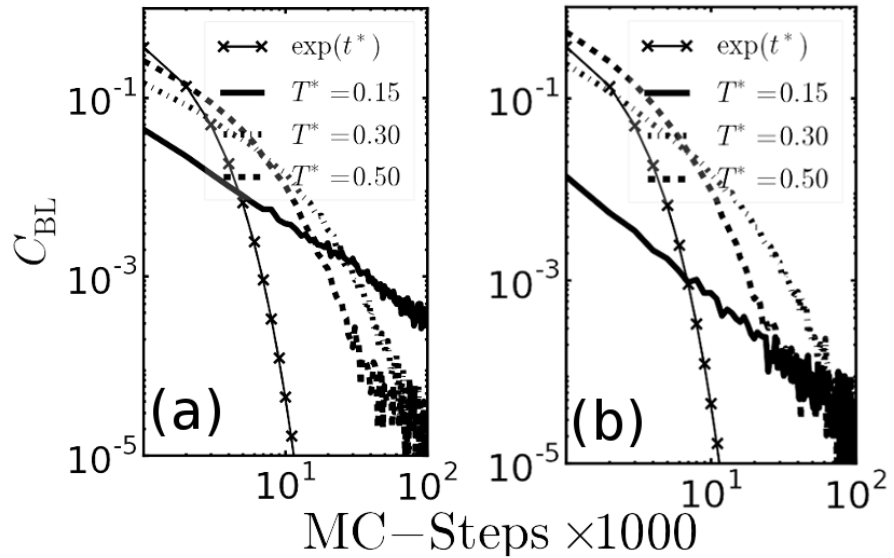


Figure 50: We show the two-particle bond-life time correlation c_{BL} at $\rho^* = 0.25$ (a) and at $\rho^* = 0.50$ (b) at three different temperatures together with an exponential function.

plateau at $T^* = 0.15$ at $\rho^* = 0.5$. This is due to the trapping of the DID between the long chains built by the ID and the resulting network formation. The trapping takes place at a length scale $\sim 0.1\sigma$ which is similar to gels in dipolar colloids in three dimensions and an external field [73] and one order of magnitude smaller than dipolar colloids without field [111]. At the lower density regime, $\rho^* = 0.25$ the slowing down is less pronounced and we cannot identify a pronounced plateau of the MSD parallel or perpendicular to the field. To study to which extent the solvent affects these results we employ non-overdamped BD simulations. Technical details of this simulation method including random forces and torques can be found in [115, 183, 79]. The basic idea is to employ MD simulations with additional friction emerging from the solvent. In Figure 49 the lowermost dashed lines of the main plots illustrate the BD results at $T^* = 0.15$ for a medium friction coefficient, corresponding to the continuous line directly above. The dynamical slowing down persists even for high friction coefficients (not shown) and we thus conclude that the dynamical arrest is emerging from strong network formation.

The simulations using the MD and BD simulation techniques were performed by Sebastian Jäger.

To further elucidate the dynamic behavior we also investigate the two-particle bond-life time correlation, c_{BL} , by computing the time correlation of two-particle bonds. For this purpose we use again MC simulations since we obtain far better statistics. A recent study showed that MC simulations can be quantitatively compared to overdamped Brownian Dynamics [142]. The step size in our MC simulations were chosen that way that the equilibrated systems have a constant acceptance rate and we can thus compare the MC step directly to a time step. We did not attempt to compare the MC and MD times quantitatively. In Figure 50 we show c_{BL} at $\rho^* = 0.25$ and $\rho^* = 0.50$, respectively. Above the percolation transition the correlation decays exponentially, $c_{BL} \sim \exp(-t^*)$, where t^* corresponds in this context to MC-steps. By decreasing the temperature the exponential behavior becomes more stretched. Such a change of the dynamics is also found in other gel-like system of dipolar colloids, where the bond correlation decays according to $\exp(-t/\tau)^\beta$, with $\beta < 1$ [73, 35]. After the percolation takes place the bond-life time decays in our system with a power law $c_{BL} \sim (t^*)^{-\alpha}$. We obtain for the exponent at $\rho^* = 0.25$ the value $\alpha = 1.09 \pm 0.04$ and at $\rho^* = 0.5$ the value $\alpha = 1.36 \pm 0.04$. This behavior is somehow different to dipolar colloids in three dimensions where a qualitative change of the bond-correlation function from exponential to stretched exponential decay due to gelation was found [73, 35]. But from our data as seen in Figure 50 it is difficult to decide whether we obtain a power-law or stretched exponential decay due to the bad statistics for the long living bonds.

5.4 SUMMARY

To summarize, we employed different simulation techniques, namely MC and MD simulation to study the network formation and the related dynamics of a mixture of particles comprised of induced dipole moments. One sort contains one induced dipole whereas the other one possesses two induced dipoles of opposite direction. Further, we studied the influence of the solvent by using non-overdamped BD simulations. The results reveal a two-dimensional network formation of mixtures of ID and DID. Our approach is inspired by recent experiments where similar particles are synthesized in the lab [48] and are thus a promising approach in the design of materials with tunable electrical, thermal or mechanical properties [131, 157]. In particular, the percolation and the network formation is a key quantity in this context. We have shown that our theoretical model reproduces the experimentally observed structures and can be used to investigate these systems systematically. However, our simulation show deviations in terms of the amount of T- and Y-connections and the overall rigidity of the found structures. The exact composition of DID and ID in the experiment due to the imperfections is not clear. Moreover, the interaction between the particles seems to be stronger than estimated by the COMSOL simulations [48]. Although, we have been able to study the fascinating effect of percolation into two dimensions close to the experimental situation.

The dipole-dipole coupling has a significant influence on the percolation (see Figure 45) which takes place parallel to the external field and perpendicular to it. The particle density, however, needs to be above a certain threshold to induce the percolation perpendicular to the field ($\rho^* \geq 0.25$). This is significantly larger than the minimum density to obtain percolation parallel to the field ($\rho^* \leq 0.1$) as seen in Figure 48. Further we showed that the total particle density and the amount of DID has a strong influence on the percolation and consequently on the networks. The transition can be influenced by these parameters where higher density and c_{DID} increases the probability to find percolation perpendicular to the field. Figure 48 reveals that a particular composition can lead the percolation parallel and perpendicular to the field to take place at the same density. We showed by combining MD, MC and BD simulations that the network structures show a gel-like behavior. The dynamics are slowed down by the trapping caused by the network formation, which is demonstrated by the MSD in Figure 49 and c_{BF} in Figure 50. We find a pronounced plateau of the MSD at medium densities perpendicular to the field and also a qualitative change of the decay of the bond correlation times. Our results are relevant not only for induced dipole systems but also for similar systems consisting of colloidal particles in nematic crystals [116, 122] or patchy particles [159].

CONCLUSION AND OUTLOOK

In this work we have used computer simulations to study various systems of particles with anisotropic interactions, namely particles with dipole and dipole-like potentials. Due to current experimental realizations we have focused our research on two-dimensional systems representing realistic situations on a thin film or a surface [19, 47, 125]. We have mainly employed MC and DMD simulations to study the phase behavior, the self-assembly and the dynamic anomalous behavior of different setups comprised of particles with permanent or induced dipole moments.

In the first part of this thesis we have investigated the vapor-liquid phase separation of quasi two-dimensional SM particles. The choice of an additional van-der-Waals interaction is due to the fact that the existence of a liquid-vapor phase separation in pure dipolar systems is still an unresolved issue [138, 82], whereas a particle model with additional attraction displays a clear phase separation [70, 78, 51]. We have used two state-of-the-art MC techniques, WL [181] and SU sampling [176], to determine the critical behavior. Both techniques overcome the free-energy barrier separating the two phases by computing a weight-function on the fly during a GC simulation. In the zero field case we have shown that both techniques lead to very similar results that agree well with other simulation studies of such systems [51, 127]. Further, we have clarified the question if such a quasi two-dimensional system is part of the 2D Ising universality class. To this end, we have studied the fourth-order Binder cumulant for three different system sizes and we were able to show that our system does indeed fit well in this universality class. The performance of both advanced MC techniques was investigated by employing them to a weak, medium, and strong dipole coupling. We could show that SU sampling is in general faster but is plagued by strong statistical errors in systems with a strong coupling due to the pronounced assembly of particles into chains and rings. WL sampling, however, is a self-adapting algorithm and could overcome the free-energy barrier even of the strongly coupled system and sample both phases with sufficient accuracy at the expense of larger simulation times.

By applying an external field perpendicular to the plane we obtain a different situation. Most dipoles align themselves perpendicular to

the plane and we end up with an effective weakening of the attraction of the LJ interaction. We were able to determine a phase separation for weakly coupled dipoles and medium field strength, in which not all dipoles are perfectly aligned to the field. The sampling took considerably longer due to the orientational bias introduced by the field and SU sampling was not able to reveal the phase separation. We were able to determine the phase separation by WL sampling and showed that the critical temperature decreases around 20% compared to the zero field case due to an increase in the repulsion of dipoles aligned perpendicularly to the plane.

The case of an external field parallel to the field favors the head-to-tail configuration of dipoles. Again, SU sampling was not able to identify the phase separation, whereas WL sampling was very well suited. The critical temperature of the medium coupled dipoles and an additional external field increases about 40% as compared to the case without field.

We also investigated the case of dipoles exposed to a rotating external field. If the dipoles are completely synchronized with the external field we obtain an effective interaction that is attractive. By employing WL sampling to particles with such an effective potential we were able to reveal a phase separation, that explains experimental observations of strong clustering in such systems.

Starting from our results, there are many interesting questions that could be studied following our work. An interesting technical point is the acceleration of simulations with dipole-dipole interactions. Due to the long-range character we employed the Ewald summation technique which is computationally very expensive. In order to study interesting phenomena, large systems are often required, e. g., such as the question if long-range orientational order exists in two-dimensional dipolar systems [190]. An interesting approach is the implementation of the Ewald summation on a Graphic Processing Unit (GPU). This improvement in simulation speed is a highly active field of research, since GPUs are a cheap and very efficient alternative to conventional computing clusters using CPUs [67]. However, many works focus on Molecular Dynamics Simulations [81, 10] and an effective implementation of a MC simulation is still lacking.

The effect of the external potential on the phase behavior of a quasi two-dimensional system of dipolar particles is another interesting questions that could be studied in broader detail. Recent works deal with the so-called shoulder potentials that approximate dipolar particles on a plane under the influence of a strong field perpendicular to the plane. A very rich phase behavior is found, reaching from network structures to several ordered phases [27]. Also the dynamics of such systems reveal interesting dynamic properties including single-particle and collective motions [28]. Advanced MC techniques such as WL and SU sampling, used in this work, can be used to further

investigate the phase behavior and to determine the character of the transitions, first-order or continuous. These results could be compared to corresponding three-dimensional results [119, 45]. Recent simulation studies report the appearance of chains and bundles of chains when dipoles [85] or dipolar dumbbells [73] are exposed to a uniform external field. As a result of the chaining anomalous dynamic behavior is found. The dynamic properties of our quasi two-dimensional dipolar system under the influence of an external field parallel to the plane is still an open question. To which extent the reduced dimensions effect the dynamic behavior of the two-dimensional system is a very interesting issue.

Binary mixtures of dipoles of different strength or dipolar particles mixed with particles of a different type a certainly more realistic. The three-dimensional case of a binary mixture of DHS has already been studied. Many interesting phases are found [57] and the effect of different dipole strengths on the phase diagram was investigated [158]. The demixing of DHS mixed with HS is an interesting approach to elucidate the open question of a vapor-liquid phase separation in DHS [7]. Two-dimensional dipoles exposed to a field in plane display a combined condensation-demixing transition [105]. Starting from these results the effect of different dipolar strengths in the quasi two-dimensional case and a possible demixing transition is interesting and important with regard to the fabrication process of advanced materials.

To expand the picture of the system of dipoles on a plane we have investigated the phase diagram of a colloidal system with dipole-like interactions. The particles possess an anisotropic interaction that resembles locally the regular dipole interaction. However, no long-range interactions were taken into account [57]. The model is comprised of a Hard-Sphere with two embedded charges, positive and negative, that are modeled by a three-step square-well and square shoulder potential. This model was already employed to explore the three-dimensional phase diagram. Again, we focus on the two-dimensional case. This model allows us to use DMD simulations, a fast alternative to standard MD simulations.

We were able to identify several phases, reaching from an isotropic fluid at high temperatures, over a polymer fluid, to a percolated gel-like phase. We investigated the dynamic properties of the percolated system in further detail by determining the MSD. This quantity displayed a small plateau between the ballistic and the diffusive regime, indicating a dynamical slowing down. Similar behavior is found in systems of dipolar dumbbells [24], dipolar systems exposed to an external field [85], and patchy particles [140]. The self-part of the van Hove function confirmed the gel-like behavior. Due to very long equilibration times at higher densities we were not able to study the possible formation of a glass or glass-like phase at higher densities.

At high densities we found a transition into a hexagonal ordered phase with long-range orientational order. This behavior is in marked contrast to real dipoles, where no long-range orientational order is found, only domains of local order [190]. Even by increasing the system size significantly the orientational order persisted. This transition was accompanied by large fluctuations, that is pronounced peaks of the specific heat and the susceptibility of the orientational order parameter, pointing into a continuous phase transition.

Based on our findings, there are several interesting questions to investigate in future studies. First, we did not attempt to determine free-energies of the different phases in order to rigorously study the character of the transitions. Using advanced MC techniques, such as WL or SU sampling, could be a promising approach to identify the phase boundaries and the character of the fluid-fluid transitions. We have employed these techniques successfully in the case of the vapor-liquid phase separation but it has already been used for fluid-fluid transitions [49]. A further subject of future investigations is to deepen the understanding of the gel-like behavior. Determining the intermediate scattering function F defined by [179]

$$F(\vec{q}, t) = \frac{1}{N} \langle \delta\rho^*(\vec{q}, t), \delta\rho(\vec{q}, t) \rangle, \quad \rho(\vec{q}, t) = \sum_{i=1}^N \exp[i\vec{q} \cdot \vec{r}_i(t)], \quad (6.1)$$

could be used to further elucidate the gel-like and even a possible glass-like state of the system. A prediction of Mode Coupling Theory (MCT) [55] is the existence of a critical temperature, T_c , at which the self diffusion constant vanishes according to a power law [179]

$$D \propto (T - T_c)^\gamma. \quad (6.2)$$

This quantity can be computed in computer simulations and allows us to compare the results to the MCT and to determine the glass or gel-like state of the system. The DMD simulation technique we employed is fast compared to traditional MD or MC. Therefore, we are able to study large systems and can thus investigate the melting transition in more detail. It is still an unresolved question if the melting occurs in two-dimensional systems from an isotropic fluid, over an intermediate hexatic phase to a crystal phase. Even in hard discs it is still not clear [18]. According to the Kosterlitz-Thouless-Halperin-Nelson-Young (KTHNY) theory a hexatic phase emerges between a solid and a liquid phase. The hexatic phase is characterized by a short-range positional and a quasi-long-range orientational (sixfold) order [94]. Recent works of dipolar systems in two dimensions support the KTHNY theory [100] but a full understanding is still lacking. Our model combined with the DMD method could be used to illuminate this question by using large scale simulations and by computing time correlation functions, where in the hexatic phase an algebraic decay is expected.

In the next part of this work we have been focusing on systems comprised of induced dipoles in two dimensions. Inspired by recent progress in synthesizing particles with complex multipole interactions we modeled similar systems and employed computer simulations to study the phenomenon of two-dimensional percolation. Polystyrene particles that are coated with a gold patch on 11% of their surface possess two oppositely aligned induced dipoles, one emerging from the dielectric polystyrene particle, the other one is induced in the gold patch [48]. The resulting particles possess an interaction similar to quadrupoles and assemble in structures perpendicular to the external field. By mixing them with regular induced dipoles two-dimensional networks can be observed. Percolation plays an important role in controlling, e. g., the electric conductivity [157] as well as the thermal conductivity [131].

Using simulated annealing to investigate the ground state structures we were able to reveal that particles with two induced dipoles (DID) assemble into short chains perpendicular to the field, whereas a larger amount of DID tends to build compact clusters similar to true quadrupoles [172]. DID that possess different orientations (i. e., (parallel | anti-parallel) and (anti-parallel | parallel) with respect to the external field) build staggered chains perpendicular to the field. Mixing regular induced dipoles (ID) and DID leads to triangular connections between the ID and DID. We employed MC simulations in the canonical ensemble to study the phase transition associated with the percolation parallel and perpendicular to the field. A certain minimum amount of the total packing fraction and amount of DID in the mixture is necessary to induce a two-dimensional percolation. We showed that these parameters can be used to tune the percolation transition in both directions. In a further step we focused on the dynamic properties of the percolated networks. To this end, we applied MD simulations to investigate the MSD. We found a pronounced plateau of the MSD perpendicular to the field and a less pronounced one parallel to the field. Also, the bond correlation time showed a qualitative change from exponential decay to a power-law decay after the percolation transition. Similar behavior was found in three-dimensional dipolar systems [35, 73], where, however, a change from exponential to stretched exponential is reported. The influence of the solvent was also controlled by simulating the system with non-overdamped Brownian Dynamics simulations. No significant influence was found and we thus conclude that the percolated structures build a persistent gel phase.

There are several interesting questions arising from our investigations. First, it is necessary to gain a deeper understanding of the gel phase in the system. By simulating different system sizes we could show that the percolation is not a finite-size effect. The MSD and the bond correlation time point to a gel-like phase but in order to really reveal the character of the phase one should compute the interme-

diate scattering function according to Equation 6.1, the power-law behavior of the diffusion constant according to Equation 6.2, and time correlation functions.

Beside the low and medium density properties we have already studied, the high density structures are of great interest with regard to applications. Important examples are two-dimensional photonic crystals. If the periodicity is comparable to the wavelength of light such crystals can be used to manipulate light on the microscale [103]. Also, electronic properties of thin-film crystals can be influenced by the crystal structure [182]. More complicated structures are needed to produce so-called lab-on-the-chip devices. These devices, produced by self-assembly of particles on the nano- or microscale, are used for bioassays, separation technologies and chemical synthesis techniques [36]. Recent experimental works have shown how to produce different crystal structures by induced dipoles [174, 102]. From a theoretical point of view it is interesting to explore possible structures of particles with complex interactions. The DID and a mixture of DID and ID may be a promising approach to generate new crystal structures.

Even more structures are possible by particles with more complex interactions [53, 201]. Starting from our model the combination of three induced dipoles gives rise to new self-assembled structures, which was already partly discovered in experiments [48]. A further possibility is the combination of electric and magnetic dipoles, induced or permanent. To influence the assembly in different directions independently is a fascinating new way in the fabrication of advanced materials. Computer simulations are able to discover the possibilities and limitations of these approaches.

BIBLIOGRAPHY

- [1] David J. Adams, Eveline M. Adams, and Graham J. Hills. The computer simulation of polar liquids. *Molecular Physics*, 38(2):387–400, 1979.
- [2] Amnon Aharony and Michael E. Fisher. Critical behavior of magnets with dipolar interactions. i. renormalization group near four dimensions. *Phys. Rev. B*, 8:3323–3341, Oct 1973.
- [3] B J Alder and E L Pollock. Simulation of polar and polarizable fluids. *Annual Review of Physical Chemistry*, 32(1):311–329, 1981.
- [4] B. J. Alder and T. E. Wainwright. Phase transition for a hard sphere system. *The Journal of Chemical Physics*, 27(5):1208–1209, 1957.
- [5] B. J. Alder and T. E. Wainwright. Studies in molecular dynamics. i. general method. *The Journal of Chemical Physics*, 31(2):459–466, 1959.
- [6] M. P. Allen and D. J. Tildesley. *Computer Simulation of Liquids*. Oxford science publications. Oxford University Press, USA, 1989.
- [7] N. G. Almarza, E. Lomba, C. Martin, and A. Gallardo. Demixing in binary mixtures of apolar and dipolar hard spheres. *The Journal of Chemical Physics*, 129(23):234504, 2008.
- [8] Carlos Alvarez, Martial Mazars, and Jean-Jacques Weis. Structure and thermodynamics of a ferrofluid bilayer. *Phys. Rev. E*, 77(5):051501, May 2008.
- [9] Hans C. Andersen. Molecular dynamics simulations at constant pressure and/or temperature. *The Journal of Chemical Physics*, 72(4):2384–2393, 1980.
- [10] Joshua A. Anderson, Chris D. Lorenz, and A. Travesset. General purpose molecular dynamics simulations fully implemented on graphics processing units. *Journal of Computational Physics*, 227(10):5342 – 5359, 2008.
- [11] Andrew J. Archer and Nigel B. Wilding. Phase behavior of a fluid with competing attractive and repulsive interactions. *Phys. Rev. E*, 76:031501, Sep 2007.
- [12] J.A. Barker and R.O. Watts. Monte carlo studies of the dielectric properties of water-like models. *Molecular Physics*, 26(3):789–792, 1973.

- [13] J Baschnagel, C Bennemann, W Paul, and K Binder. Dynamics of a supercooled polymer melt above the mode-coupling critical temperature: cage versus polymer-specific effects. *Journal of Physics: Condensed Matter*, 12(29):6365, 2000.
- [14] A. Bellemans, J. Orban, and D. Van Belle. Molecular dynamics of rigid and non-rigid necklaces of hard discs. *Molecular Physics*, 39(3):781–782, 1980.
- [15] Jason J. Benkoski, Ryan M. Deacon, H. Bruce Land, Lance M. Baird, Jennifer L. Breidenich, Rengaswamy Srinivasan, Guy V. Clatterbaugh, Pei Yuin Keng, and Jeffrey Pyun. Dipolar assembly of ferromagnetic nanoparticles into magnetically driven artificial cilia. *Soft Matter*, 6:602–609, 2010.
- [16] Bernd A. Berg and Thomas Neuhaus. Multicanonical algorithms for first order phase transitions. *Physics Letters B*, 267(2):249 – 253, 1991.
- [17] Bernd A. Berg and Thomas Neuhaus. Multicanonical ensemble: A new approach to simulate first-order phase transitions. *Phys. Rev. Lett.*, 68:9–12, Jan 1992.
- [18] Etienne P. Bernard and Werner Krauth. Two-step melting in two dimensions: First-order liquid-hexatic transition. *Phys. Rev. Lett.*, 107:155704, Oct 2011.
- [19] Ketan H. Bhatt and Orlin D. Velev. Control and modeling of the dielectrophoretic assembly of on-chip nanoparticle wires. *Langmuir*, 20(2):467–476, 2004. PMID: 15743092.
- [20] Emanuela Bianchi, Julio Largo, Piero Tartaglia, Emanuela Zaccarelli, and Francesco Sciortino. Phase diagram of patchy colloids: Towards empty liquids. *Phys. Rev. Lett.*, 97(16):168301, Oct 2006.
- [21] Emanuela Bianchi, Piero Tartaglia, Emanuela Zaccarelli, and Francesco Sciortino. Theoretical and numerical study of the phase diagram of patchy colloids: Ordered and disordered patch arrangements. *J. Chem. Phys*, 128(14):144504, 2008.
- [22] Kurt Binder. Finite size scaling analysis of ising model block distribution functions. *Z. Phys. B - Condensed Matter*, 43:119–140, 1981.
- [23] Kurt Binder and Walter Kob. *Glassy Materials and Disordered Solids*. World Scientific Publishing Co. Pte. Ltd., 1st edition, 2005.
- [24] R. Blaak, M. A. Miller, and J.-P. Hansen. Reversible gelation and dynamical arrest of dipolar colloids. *EPL (Europhysics Letters)*, 78(2):26002, 2007.

- [25] Dezso Boda, Jochen Winkelmann, Janos Liszi, and Istvan Szalai. Vapour-liquid equilibrium of Stockmayer fluids in applied field. *Molecular Physics*, 87(3):601–624, 1996.
- [26] Jean-Michel Caillol. Search of the gas–liquid transition of dipolar hard spheres. *The Journal of Chemical Physics*, 98(12):9835–9849, 1993.
- [27] Philip J. Camp. Structure and phase behavior of a two-dimensional system with core-softened and long-range repulsive interactions. *Phys. Rev. E*, 68:061506, Dec 2003.
- [28] Philip J. Camp. Dynamics in a two-dimensional core-softened fluid. *Phys. Rev. E*, 71:031507, Mar 2005.
- [29] Philip J. Camp, J. C. Shelley, and G. N. Patey. Isotropic fluid phases of dipolar hard spheres. *Phys. Rev. Lett.*, 84:115–118, Jan 2000.
- [30] X Campi, H Krivine, and N Sator. Percolation line of self-bound clusters in supercritical fluids. *Physica A: Statistical Mechanics and its Applications*, 296(1-2):24–30, 2001.
- [31] Qian Chen, Jonathan K. Whitmer, Shan Jiang, Sung Chul Bae, Erik Luijten, and Steve Granick. Supracolloidal reaction kinetics of janus spheres. *Science*, 331(6014):199–202, 2011.
- [32] Levesque D and Weis J J. Orientational and structural order in strongly interacting dipolar hard spheres. *Phys. Rev. E*, 49:5131, 1994.
- [33] S. Sarkar Das, A. Ploplis Andrews, and S. C. Greer. Living poly(α -methylstyrene) near the polymerization line. iv. extent of polymerization as a function of temperature. *The Journal of Chemical Physics*, 102(7):2951–2959, 1995.
- [34] S. W. de Leeuw, J. W. Perram, and E. R. Smith. Simulation of electrostatic systems in periodic boundary conditions. i. lattice sums and dielectric constants. *Proceedings of the Royal Society of London. A. Mathematical and Physical Sciences*, 373(1752):27–56, 1980.
- [35] Emanuela Del Gado and Walter Kob. A microscopic model for colloidal gels with directional effective interactions: network induced glassy dynamics. *Soft Matter*, 6:1547–1558, 2010.
- [36] Dittrich Petra S. and Manz Andreas. Lab-on-a-chip: microfluidics in drug discovery. *Nat Rev Drug Discov*, 5(3):210–218, mar 2006. 10.1038/nrd1985.

- [37] Günther Doppelbauer, Emanuela Bianchi, and Gerhard Kahl. Self-assembly scenarios of patchy colloidal particles in two dimensions. *Journal of Physics: Condensed Matter*, 22(10):104105, 2010.
- [38] N. Elsner, C. P. Royall, B. Vincent, and D. R. E. Snoswell. Simple models for two-dimensional tunable colloidal crystals in rotating ac electric fields. *J. Chem. Phys.*, 130:154901, 2009.
- [39] Donald L. Ermak and J. A. McCammon. Brownian dynamics with hydrodynamic interactions. *The Journal of Chemical Physics*, 69(4):1352–1360, 1978.
- [40] Jeffrey R. Errington, Pablo G. Debenedetti, and Salvatore Torquato. Quantification of order in the lennard-jones system. *J. Chem. Phys*, 118(5):2256–2263, 2003.
- [41] W.-X. Fang, Z.-H. He, X.-Q. Xu, Z.-Q. Mao, and H. Shen. Magnetic-field-induced chain-like assembly structures of Fe₃O₄ nanoparticles. *EPL (Europhysics Letters)*, 77(6):68004, 2007.
- [42] Alan M. Ferrenberg and Robert H. Swendsen. New monte carlo technique for studying phase transitions. *Phys. Rev. Lett.*, 61:2635–2638, Dec 1988.
- [43] Alan M. Ferrenberg and Robert H. Swendsen. Optimized monte carlo data analysis. *Phys. Rev. Lett.*, 63:1195–1198, Sep 1989.
- [44] M. Fitzgerald, R. R. Picard, and R. N. Silver. Canonical transition probabilities for adaptive Metropolis simulation. *EPL (Europhysics Letters)*, 46(3):282, 1999.
- [45] Yu. D. Fomin, N. V. Gribova, V. N. Ryzhov, S. M. Stishov, and Daan Frenkel. Quasibinary amorphous phase in a three-dimensional system of particles with repulsive-shoulder interactions. *The Journal of Chemical Physics*, 129(6):064512, 2008.
- [46] Daan Frenkel and Berend Smit. *Understanding Molecular Simulations*. Academic Press, 1996.
- [47] Sumit Gangwal, Olivier J. Cayre, and Orlin D. Velev. Dielectrophoretic Assembly of Metallodielectric Janus Particles in AC Electric Fields. *Langmuir*, 24(23):13312–13320, 2008.
- [48] Sumit Gangwal, Amar Pawar, Ilona Kretzschmar, and Orlin D. Velev. Programmed assembly of metallodielectric patchy particles in external ac electric fields. *Soft Matter*, 6:1413–1418, 2010.
- [49] Georg Ganzenmüller and Philip J. Camp. Applications of wang-landau sampling to determine phase equilibria in complex fluids. *The Journal of Chemical Physics*, 127(15):154504, 2007.

- [50] Georg Ganzenmüller and Philip J. Camp. Vapor-liquid coexistence in fluids of charged hard dumbbells. *The Journal of Chemical Physics*, 126(19):191104, 2007.
- [51] G. T. Gao, X. C. Zeng, and Wenchuan Wang. Vapor-liquid coexistence of quasi-two-dimensional stockmayer fluids. *The Journal of Chemical Physics*, 106(8):3311–3317, 1997.
- [52] V Giner, M Sancho, R S Lee, G Martinez, and R Pethig. Transverse dipolar chaining in binary suspensions induced by rf fields. *Journal of Physics D: Applied Physics*, 32(10):1182, 1999.
- [53] S. C. Glotzer and Solomon. Anisotropy of building blocks and their assembly into complex structures. *Nature Materials*, 6:557–562, 2007.
- [54] Sharon C. Glotzer. Spatially heterogeneous dynamics in liquids: insights from simulation. *Journal of Non-Crystalline Solids*, 274(1-3):342 – 355, 2000. *Physics of Non-Crystalline Solids* 9.
- [55] W. Götze and L. Sjögren. The mode coupling theory of structural relaxations. *Transport Theory and Statistical Physics*, 24(6-8):801–853, 1995.
- [56] Amit Goyal, Carol K. Hall, and Orlin D. Velev. Phase diagram for stimulus-responsive materials containing dipolar colloidal particles. *Phys. Rev. E*, 77(3):031401, Mar 2008.
- [57] Amit Goyal, Carol K. Hall, and Orlin D. Velev. Self-assembly in binary mixtures of dipolar colloids: Molecular dynamics simulations. *J. Chem. Phys*, 133(6):064511, 2010.
- [58] C. G. Gray and K. E. Gubbins. *Theory of Molecular Fluids*. Oxford University Press, 1984.
- [59] C. G. Gray and K. E. Gubbins. *Theory of Molecular Fluids Fundamentals*. Oxford University Press, 1st edition, 1984.
- [60] J. L. Griffin and C. D. Ferris. Pearl chain formation across radio frequency fields. *Nature*, 226:152, 1970.
- [61] Robert B. Griffiths. Dependence of critical indices on a parameter. *Phys. Rev. Lett.*, 24:1479–1482, Jun 1970.
- [62] B. Groh and S. Dietrich. Crystal structures and freezing of dipolar fluids. *Phys. Rev. E.*, 63:021203, 2001.
- [63] J. Gubernatis and N. Hatano. The multicanonical monte carlo method. *Computing in Science Engineering*, 2(2):95 –102, march-april 2000.

- [64] Harpreet S. Gulati and Carol K. Hall. Fluids and fluid mixtures containing square-well diatomics: Equations of state and canonical molecular dynamics simulation. *J. Chem. Phys.*, 107(10):3930–3946, 1997.
- [65] M. H. J. Hagen and D. Frenkel. Determination of phase diagrams for the hard-core attractive yukawa system. *The Journal of Chemical Physics*, 101(5):4093–4097, 1994.
- [66] Jean-Pierre Hansen and Ian Ranald McDonald. *Theory of Simple Liquids*. Academic Press, 3rd edition, 2006.
- [67] M. J. Harvey and G. De Fabritiis. An Implementation of the Smooth Particle Mesh Ewald Method on GPU Hardware. *Journal of Chemical Theory and Computation*, 5(9):2371–2377, 2009.
- [68] D. Heinrich, A. R. Goñi, A. Smessaert, S. H. L. Klapp, L. M. C. Cerioni, T. M. Osán, D. J. Pusiol, and C. Thomsen. Dynamics of the field-induced formation of hexagonal zipped-chain superstructures in magnetic colloids. *Phys. Rev. Lett.*, 106(20):208301, May 2011.
- [69] D. Heinrich, A. R. Goni, and C. Thomsen. Dynamics of magnetic-field-induced clustering in ionic ferrofluids from raman scattering. *The Journal of Chemical Physics*, 126(12):124701, 2007.
- [70] Reinhard Hentschke, Jörg Bartke, and Florian Pesth. Equilibrium polymerization and gas-liquid critical behavior in the stockmayer fluid. *Phys. Rev. E*, 75:011506, Jan 2007.
- [71] C. Holm and J.-J. Weis. The structure of ferrofluids: A status report. *Current Opinion in Colloid and Interface Science*, 10(3-4):133–140, 2005.
- [72] Antti-Pekka Hynninen and Marjolein Dijkstra. Phase diagram of dipolar hard and soft spheres: Manipulation of colloidal crystal structures by an external field. *Phys. Rev. Lett.*, 94:138303, Apr 2005.
- [73] Patrick Ilg and Emanuela Del Gado. Non-linear response of dipolar colloidal gels to external fields. *Soft Matter*, 7:163–171, 2011.
- [74] Ilg, P. Importance of depletion interactions for structure and dynamics of ferrofluids. *Eur. Phys. J. E*, 26:169–176, 2008.
- [75] A. Imperio and L. Reatto. Microphase separation in two-dimensional systems with competing interactions. *The Journal of Chemical Physics*, 124(16):164712, 2006.

- [76] A. Imperio and L. Reatto. Microphase separation in two-dimensional systems with competing interactions. *The Journal of Chemical Physics*, 124(16):164712, 2006.
- [77] L. Yu. Iskakova, G. A. Smelchakova, and A. Yu. Zubarev. Condensation phase transitions in ferrofluids. *Phys. Rev. E*, 79:011401, Jan 2009.
- [78] A. O. Ivanov, S. S. Kantorovich, and Philip J. Camp. Comment on “equilibrium polymerization and gas-liquid critical behavior in the stockmayer fluid”. *Phys. Rev. E*, 77:013501, Jan 2008.
- [79] Sebastian Jäger and Sabine H. L. Klapp. Pattern formation of dipolar colloids in rotating fields: layering and synchronization. *Soft Matter*, 7:6606–6616, 2011.
- [80] A. Jaster. Computer simulations of the two-dimensional melting transition using hard disks. *Phys. Rev. E*, 59(3):2594–2602, Mar 1999.
- [81] Prateek K. Jha, Rastko Sknepnek, Guillermo Ivan Guerrero-Garcia, and Monica Olvera de la Cruz. A Graphics Processing Unit Implementation of Coulomb Interaction in Molecular Dynamics. *Journal of Chemical Theory and Computation*, 6(10):3058–3065, 2010.
- [82] Ran Jia, Heiko Braun, and Reinhard Hentschke. Gas-liquid coexistence in a system of dipolar soft spheres. *Phys. Rev. E*, 82:062501, Dec 2010.
- [83] G. P. Johari, E. Tombari, S. Presto, and G. Salvetti. Experimental evidence for the heat capacity maximum during a melt’s polymerization. *J. Chem. Phys.*, 117(10):5086–5091, 2002.
- [84] T. B. Jones. *Electromechanics of Particle*. Cambridge University Press, 1st edition, 1995.
- [85] Jelena Jordanovic, Sebastian Jäger, and Sabine H. L. Klapp. Crossover from normal to anomalous diffusion in systems of field-aligned dipolar particles. *Phys. Rev. Lett.*, 106(3):038301, Jan 2011.
- [86] Jelena Jordanovic and Sabine H. L. Klapp. Field-induced layer formation in dipolar nanofilms. *Phys. Rev. Lett.*, 101:038302, Jul 2008.
- [87] Jaime J. Juárez and Michael A. Bevan. Interactions and microstructures in electric field mediated colloidal assembly. *J. Chem. Phys.*, 131(13):134704, 2009.

- [88] Yu. V. Kalyuzhnyi, I. A. Protsykevych, G. Ganzenmüller, and P. J. Camp. Liquid-vapour coexistence in the dipolar yukawa hard-sphere fluid. *EPL (Europhysics Letters)*, 84(2):26001, 2008.
- [89] Sofia Kantorovich, Rudolf Weeber, Juan J. Cerda, and Christian Holm. Ferrofluids with shifted dipoles: ground state structures. *Soft Matter*, 7:5217–5227, 2011.
- [90] Pei Yui Keng, Inbo Shim, Bryan D. Korth, Jack F. Douglas, and Jeffrey Pyun. Synthesis and self-assembly of polymer-coated ferromagnetic nanoparticles. *ACS Nano*, 1(4):279–292, 2007.
- [91] Sabine Klapp and Frank Forstmann. Phase transitions in dipolar fluids: An integral equation study. *The Journal of Chemical Physics*, 106(23):9742–9761, 1997.
- [92] Sabine H.L. Klapp. Monte-Carlo simulations of strongly interacting dipolar fluids between two conducting walls. *Molecular Simulation*, 32(08):609–621, 2006.
- [93] Mark Klokkenburg, Ben H. Ern , Johannes D. Meeldijk, Albrecht Wiedenmann, Andrei V. Petukhov, Roel P. A. Dullens, and Albert P. Philipse. *In Situ* imaging of field-induced hexagonal columns in magnetite ferrofluids. *Phys. Rev. Lett.*, 97:185702, Nov 2006.
- [94] J M Kosterlitz and D J Thouless. Ordering, metastability and phase transitions in two-dimensional systems. *Journal of Physics C: Solid State Physics*, 6(7):1181, 1973.
- [95] Ilona Kretzschmar and Jung Hun (Kevin) Song. Surface-anisotropic spherical colloids in geometric and field confinement. *Current Opinion in Colloid and Interface Science*, 16(2):84–95, 2011.
- [96] C. H. Kua, Yee Cheong Lam, C. Yang, and Kamal Youcef-Toumi. Review of bio-particle manipulation using dielectrophoresis, 2005.
- [97] Sanat K. Kumar and Jack F. Douglas. Gelation in physically associating polymer solutions. *Phys. Rev. Lett.*, 87:188301, Oct 2001.
- [98] David P. Landau and Kurt Binder. *A Guide to Monte Carlo Simulations in Statistical Physics*. Cambridge University Press, 2nd edition, 2002.
- [99] Philip J. Lenart and Athanassios Z. Panagiotopoulos. Phase Behavior of Binary Stockmayer and Polarizable Lennard-Jones Fluid Mixtures Using Adiabatic Nuclear and Electronic Sampling. *Industrial & Engineering Chemistry Research*, 45(21):6929–6938, 2006.

- [100] S. Z. Lin, B. Zheng, and S. Trimper. Computer simulations of two-dimensional melting with dipole-dipole interactions. *Phys. Rev. E*, 73:066106, Jun 2006.
- [101] E. Lomba, F. Lado, and J. J. Weis. Structure and thermodynamics of a ferrofluid monolayer. *Phys. Rev. E*, 61(4):3838–3849, Apr 2000.
- [102] Simon O. Lumsdon, Eric W. Kaler, and Orlin D. Velev. Two-dimensional crystallization of microspheres by a coplanar ac electric field. *Langmuir*, 20(6):2108–2116, 2004. PMID: 15835659.
- [103] Simon O. Lumsdon, Eric W. Kaler, Jacob P. Williams, and Orlin D. Velev. Dielectrophoretic assembly of oriented and switchable two-dimensional photonic crystals. *Applied Physics Letters*, 82(6):949–951, feb 2003.
- [104] Liang Luo and Sabine H. L. Klapp. Fluctuations in a ferrofluid monolayer: An integral equation study. *The Journal of Chemical Physics*, 131(3):034709, 2009.
- [105] Liang Luo, Sabine H. L. Klapp, and Xiaosong Chen. String formation and demixing in monolayers of dipolar colloidal mixtures. *The Journal of Chemical Physics*, 135(13):134701, 2011.
- [106] Katie A. Maerzke and J. Ilja Siepmann. Effects of an Applied Electric Field on the Vapor-Liquid Equilibria of Water, Methanol, and Dimethyl Ether. *The Journal of Physical Chemistry B*, 114(12):4261–4270, 2010. PMID: 20201507.
- [107] Johnny N Martins, Tais Bassani, Guilherme MO Barra, and Ricardo VB Oliveira. Electrical and rheological percolation in poly(vinylidene fluoride)/multi-walled carbon nanotube nanocomposites. *Polymer International*, 60(3):430–435, 2011.
- [108] Christian Mayer, Francesco Sciortino, Piero Tartaglia, and Emanuela Zaccarelli. A spherical model with directional interactions: II. dynamics and landscape properties. *Journal of Physics: Condensed Matter*, 22(10):104110, 2010.
- [109] N. D. Mermin and H. Wagner. Absence of ferromagnetism or antiferromagnetism in one- or two-dimensional isotropic heisenberg models. *Phys. Rev. Lett.*, 17:1133–1136, Nov 1966.
- [110] Alenka Mertelj, Luka Cmok, and Martin Čopič. Anomalous diffusion in ferrofluids. *Phys. Rev. E*, 79:041402, Apr 2009.
- [111] Mark A. Miller, Ronald Blaak, Craig N. Lumb, and Jean-Pierre Hansen. Dynamical arrest in low density dipolar colloidal gels. *J. Chem. Phys.*, 130(11):114507, 2009.

- [112] Millman Jeffrey R., Bhatt Ketan H., Prevo Brian G., and Velez Orlin D. Anisotropic particle synthesis in dielectrophoretically controlled microdroplet reactors. *Nat Mater*, 4(1):98–102, jan 2005. 10.1038/nmat1270.
- [113] Min Younjin, Akbulut Mustafa, Kristiansen Kai, Golan Yuval, and Israelachvili Jacob. The role of interparticle and external forces in nanoparticle assembly. *Nat Mater*, 7(7):527–538, jul 2008. 10.1038/nmat2206.
- [114] <http://www.mcs.anl.gov/research/projects/mpi/>.
- [115] Vladimir V. Murashov and G. N. Patey. Structure formation in dipolar fluids driven by rotating fields. *The Journal of Chemical Physics*, 112(22):9828–9833, 2000.
- [116] I. Mušević, M. Škarabot, U. Tkalec, M. Ravnik, and S. Žumer. Two-dimensional nematic colloidal crystals self-assembled by topological defects. *Science*, 313(5789):954–958, 2006.
- [117] Martin Neumann. Dipole moment fluctuation formulas in computer simulations of polar systems. *Molecular Physics*, 50(4):841–858, 1983.
- [118] M. E. J. Newman and G. T. Barkema. *Monte Carlo Methods in Statistical Physics*. Oxford University Press, 1st edition, 1999.
- [119] Jr. Ney M. Barraza, Evy Salcedo, and Marcia C. Barbosa. Thermodynamic, dynamic, and structural anomalies for shoulderlike potentials. *The Journal of Chemical Physics*, 131(9):094504, 2009.
- [120] Nie Zhihong, Petukhova Alla, and Kumacheva Eugenia. Properties and emerging applications of self-assembled structures made from inorganic nanoparticles. *Nat Nano*, 5(1):15–25, jan 2010. 10.1038/nnano.2009.453.
- [121] G. E. Norman and V. S. Filinov. Investigation of a phase-transition by a monte-carlo method. *High Temperature*, 7:216–222, 1969.
- [122] U. Ognysta, A. Nych, V. Nazarenko, M. Škarabot, and Mušević I. Design of 2D Binary Colloidal Crystals in a Nematic Liquid Crystal. *Langmuir*, 25(20):12092–12100, 2009. PMID: 19757827.
- [123] <http://openmp.org/wp/>.
- [124] G. Orkoulas. Acceleration of monte carlo simulations through spatial updating in the grand canonical ensemble. *The Journal of Chemical Physics*, 127(8):084106, 2007.

- [125] N. Osterman, D. Babič, I. Poberaj, J. Dobnikar, and P. Ziherl. Observation of condensed phases of quasiplanar core-softened colloids. *Phys. Rev. Lett.*, 99(24):248301, Dec 2007.
- [126] Wei Ou-Yang, Martin Weis, Xiangyu Chen, Takaaki Manaka, and Mitsumasa Iwamoto. Study of phase transition of two-dimensional ferroelectric copolymer p(vdf-trfe) langmuir monolayer by maxwell displacement current and brewster angle microscopy. *The Journal of Chemical Physics*, 131(10):104702, 2009.
- [127] Wen-Ze Ouyang, Sheng-Hua Xu, and Zhi-Wei Sun. Gas-liquid phase coexistence in quasi-two-dimensional stockmayer fluids: A molecular dynamics study. *The Journal of Chemical Physics*, 134(1):014901, 2011.
- [128] Priyadarshi Panda, Ki Wan Bong, T. Alan Hatton, and Patrick S. Doyle. Branched Networks by Directed Assembly of Shape Anisotropic Magnetic Particles. *Langmuir*, 27(22):13428–13435, 2011.
- [129] Mukund Parthasarathy and Daniel J. Klingenberg. Electrorheology: Mechanisms and models. *Materials Science and Engineering: R: Reports*, 17(2):57 – 103, 1996.
- [130] Adeline Perro, Stephane Reculosa, Serge Ravaine, Elodie Bourgeat-Lami, and Etienne Duguet. Design and synthesis of janus micro- and nanoparticles. *J. Mater. Chem.*, 15:3745–3760, 2005.
- [131] John Philip, P. D. Shima, and Baldev Raj. Enhancement of thermal conductivity in magnetite based nanofluid due to chainlike structures. *Applied Physics Letters*, 91(20):203108, 2007.
- [132] Antonio M. Puertas, Matthias Fuchs, and Michael E. Cates. Dynamical heterogeneities close to a colloidal gel. *J. Chem. Phys.*, 121(6):2813–2822, 2004.
- [133] D. C. Rapaport. Molecular dynamics study of a polymer chain in solution. *J. Chem. Phys.*, 71(8):3299–3303, 1979.
- [134] D. C. Rapaport. *The Art of Molecular Dynamics Simulation*. Cambridge University Press, The Edinburgh Building, Cambridge, UK, 2nd edition, 2004.
- [135] J. Richardi, M. P. Pileni, and J.-J. Weis. Self-organization of magnetic nanoparticles: A monte carlo study. *Phys. Rev. E*, 77:061510, Jun 2008.
- [136] Flavio Romano, Piero Tartaglia, and Francesco Sciortino. Gas-liquid phase coexistence in a tetrahedral patchy particle model. *Journal of Physics: Condensed Matter*, 19(32):322101, 2007.

- [137] M Rovere, D W Heermann, and K Binder. The gas-liquid transition of the two-dimensional Lennard-Jones fluid. *Journal of Physics: Condensed Matter*, 2(33):7009, 1990.
- [138] Lorenzo Rovigatti, John Russo, and Francesco Sciortino. No evidence of gas-liquid coexistence in dipolar hard spheres. *Phys. Rev. Lett.*, 107:237801, Nov 2011.
- [139] V. Russier. Calculated magnetic properties of two-dimensional arrays of nanoparticles at vanishing temperature. *Journal of Applied Physics*, 89(2):1287–1294, 2001.
- [140] John Russo, Piero Tartaglia, and Francesco Sciortino. Reversible gels of patchy particles: Role of the valence. *J. Chem. Phys.*, 131(1):014504, 2009.
- [141] Miguel Sancho, Genoveva Martinez, Sagrario Munoz, Jose L. Sebastian, and Ronald Pethig. Interaction between cells in dielectrophoresis and electrorotation experiments. *Biomicrofluidics*, 4(2):022802, 2010.
- [142] E. Sanz and D. Marenduzzo. Dynamic monte carlo versus brownian dynamics: A comparison for self-diffusion and crystallization in colloidal fluids. *The Journal of Chemical Physics*, 132(19):194102, 2010.
- [143] Heiko Schmidle and Sabine H. L. Klapp. Phase transitions of two-dimensional dipolar fluids in external fields. *The Journal of Chemical Physics*, 134(11):114903, 2011.
- [144] Martin Schoen and Sabine H. L. Klapp. *Reviews in Computational Chemistry, Volume 24*. John Wiley and Sons, 1st edition, 2007.
- [145] A. J. Schultz, C. K. Hall, and J. Genzer. Box length search algorithm for molecular simulation of systems containing periodic structures. *J. Chem. Phys.*, 120(4):2049–2055, 2004.
- [146] Franz Schwabl. *Statistische Mechanik*. Springer, 1st edition, 2000.
- [147] Francesco Sciortino, Achille Giacometti, and Giorgio Pastore. Phase diagram of janus particles. *Phys. Rev. Lett.*, 103:237801, Nov 2009.
- [148] P. N. Segrè, V. Prasad, A. B. Schofield, and D. A. Weitz. Glasslike kinetic arrest at the colloidal-gelation transition. *Phys. Rev. Lett.*, 86:6042–6045, Jun 2001.
- [149] M. Scott Shell, Pablo G. Debenedetti, and Athanassios Z. Panagiotopoulos. Generalization of the wang-landau method for off-lattice simulations. *Phys. Rev. E*, 66:056703, Nov 2002.

- [150] F. Smallenburg and M. Dijkstra. Phase diagram of colloidal spheres in a biaxial electric or magnetic field. *J. Chem. Phys.*, 132:204508, 2010.
- [151] Steven W. Smith, Carol K. Hall, and Benny D. Freeman. Molecular dynamics for polymeric fluids using discontinuous potentials. *Journal of Computational Physics*, 134(1):16 – 30, 1997.
- [152] D. R. E. Snoswell, C. L. Bower, P. Ivanov, M. J. Cryan, J. G. Rarity, and B. Vincent. Dynamic control of lattice spacing within colloidal crystals. *New Journal of Physics*, 8(11):267, 2006.
- [153] Justin Stambaugh, Kevin Van Workum, Jack F. Douglas, and Wolfgang Losert. Polymerization transitions in two-dimensional systems of dipolar spheres. *Phys. Rev. E*, 72:031301, Sep 2005.
- [154] D. Stauffer and A. Aharony. *Introduction to Percolation Theory*. Taylor and Francis, 2nd edition, 2003.
- [155] Mark J. Stevens and Gary S. Grest. Phase coexistence of a stockmayer fluid in an applied field. *Phys. Rev. E*, 51:5976–5984, Jun 1995.
- [156] W. H. Stockmayer. Second virial coefficients of polar gas mixtures. *The Journal of Chemical Physics*, 9(12):863–870, 1941.
- [157] Gang Sun, Kunquan Lu, and Ferenc Kun. Percolation-induced conductor-insulator transition in a system of metal spheres in a dielectric fluid. *Phys. Rev. E*, 83:041405, Apr 2011.
- [158] I. Szalai and S. Dietrich. Global phase diagrams of binary dipolar fluid mixtures. *Molecular Physics*, 103(21-23):2873–2895, 2005.
- [159] Piero Tartaglia and Francesco Sciortino. Association of limited valence patchy particles in two dimensions. *Journal of Physics: Condensed Matter*, 22(10):104108, 2010.
- [160] J. M. Tavares, J. J. Weis, and M. M. Telo da Gama. Quasi-two-dimensional dipolar fluid at low densities: Monte carlo simulations and theory. *Phys. Rev. E*, 65:061201, Jun 2002.
- [161] J. M. Tavares, J. J. Weis, and M. M. Telo da Gama. Phase transition in two-dimensional dipolar fluids at low densities. *Phys. Rev. E*, 73(4):041507, Apr 2006.
- [162] P I C Teixeira, J M Tavares, and M M Telo da Gama. The effect of dipolar forces on the structure and thermodynamics of classical fluids. *Journal of Physics: Condensed Matter*, 12(33):R411, 2000.
- [163] <http://code.google.com/p/thrust/>.

- [164] T. Tlusty and S. A. Safran. Defect-induced phase separation in dipolar fluids. *Science*, 290(5495):1328–1331, 2000.
- [165] Glenn M. Torrie and John P. Valleau. Monte carlo free energy estimates using non-boltzmann sampling: Application to the sub-critical lennard-jones fluid. *Chemical Physics Letters*, 28(4):578 – 581, 1974.
- [166] G.M. Torrie and J.P. Valleau. Nonphysical sampling distributions in monte carlo free-energy estimation: Umbrella sampling. *Journal of Computational Physics*, 23(2):187 – 199, 1977.
- [167] R. A. Trasca and S. H. L. Klapp. Structure formation in layered ferrofluid nanofilms. *J. Chem. Phys.*, 129(8):084702, 2008.
- [168] Dimo I. Uzunov. *Introduction to the theory of critical phenomena*. World Scientific Publishsing, 2nd edition, 2010.
- [169] Alfons van Blaaderen. Materials science: Colloids get complex. *Nature*, 439:545–546, 2006.
- [170] M. E. van Leeuwen and B. Smit. What makes a polar liquid a liquid? *Phys. Rev. Lett.*, 71:3991, 1993.
- [171] M. E. van Leeuwen, B. Smit, and E. M. Hendriks. Vapour-liquid equilibria of stockmayer fluids. *Molecular Physics*, 78:271, 1993.
- [172] Kevin Van Workum and Jack F. Douglas. Symmetry, equivalence, and molecular self-assembly. *Phys. Rev. E*, 73:031502, Mar 2006.
- [173] Orlin D. Velev and Ketan H. Bhatt. On-chip micromanipulation and assembly of colloidal particles by electric fields. *Soft Matter*, 2:738–750, 2006.
- [174] Orlin D. Velev and Shalini Gupta. Materials fabricated by micro- and nanoparticle assembly. the challenging path from science to engineering. *Advanced Materials*, 21(19):1897–1905, 2009.
- [175] Loup Verlet and Jean-Jacques Weis. Perturbation theories for polar fluids. *Molecular Physics*, 28(3):665–682, 1974.
- [176] Peter Virnau and Marcus Müller. Calculation of free energy through successive umbrella sampling. *The Journal of Chemical Physics*, 120(23):10925–10930, 2004.
- [177] Peter Virnau, Marcus Müller, L. G. MacDowell, and K. Binder. Phase behavior of n-alkanes in supercritical solution: A monte carlo study. *The Journal of Chemical Physics*, 121(5):2169–2179, 2004.
- [178] Jiří Škvor and Ivo Nezbeda. Percolation threshold parameters of fluids. *Phys. Rev. E*, 79:041141, Apr 2009.

- [179] Kob Walter. *The Mode-Coupling Theory of the Glass Transition*, chapter 4, pages 28–44. American Chemical Society, 1997.
- [180] Andreas Walther and Axel H. E. Müller. Janus particles. *Soft Matter*, 4:663–668, 2008.
- [181] Fugao Wang and D. P. Landau. Efficient, multiple-range random walk algorithm to calculate the density of states. *Phys. Rev. Lett.*, 86:2050–2053, Mar 2001.
- [182] Lingyan Wang, Xiajing Shi, Nancy N. Kariuki, Mark Schadt, Guannan Roger Wang, Qiang Rendeng, Jeongku Choi, Jin Luo, Susan Lu, and Chuan-Jian Zhong. Array of Molecularly Mediated Thin Film Assemblies of Nanoparticles: Correlation of Vapor Sensing with Interparticle Spatial Properties. *Journal of the American Chemical Society*, 129(7):2161–2170, 2007. PMID: 17253690.
- [183] Zuwei Wang, Christian Holm, and Hanns Walter Müller. Molecular dynamics study on the equilibrium magnetization properties and structure of ferrofluids. *Phys. Rev. E*, 66:021405, Aug 2002.
- [184] A. Weddemann, F. Wittbracht, B. Eickenberg, and A. Hütten. Magnetic Field Induced Assembly of Highly Ordered Two-Dimensional Particle Arrays. *Langmuir*, 26:19225, 2010.
- [185] Dongqing Wei and G. N. Patey. Orientational order in simple dipolar liquids: Computer simulation of a ferroelectric nematic phase. *Phys. Rev. Lett.*, 68(13):2043–2045, Mar 1992.
- [186] J. J. Weis. Orientational structure in a monolayer of dipolar hard spheres. *Molecular Physics*, 100(5):579, 2002.
- [187] J. J. Weis. Simulation of quasi-two-dimensional dipolar systems. *Journal of Physics: Condensed Matter*, 15(15):S1471, 2003.
- [188] J. J. Weis and D. Levesque. Chain formation in low density dipolar hard spheres: A monte carlo study. *Phys. Rev. Lett.*, 71(17):2729–2732, Oct 1993.
- [189] J. J. Weis and D. Levesque. Ferroelectric phases of dipolar hard spheres. *Phys. Rev. E*, 48(5):3728–3740, Nov 1993.
- [190] J J Weis, J M Tavares, and M M Telo da Gama. Structural and conformational properties of a quasi-two-dimensional dipolar fluid. *Journal of Physics: Condensed Matter*, 14(40):9171, 2002.
- [191] M S Wertheim. Equilibrium statistical mechanics of polar fluids. *Annual Review of Physical Chemistry*, 30(1):471–501, 1979.

- [192] B. Widom. Some topics in the theory of fluids. *J. Chem. Phys.*, 39:2808–2813, 1963.
- [193] A. Wiedenmann, A. Hoell, M. Kammel, and P. Boesecke. Field-induced pseudocrystalline ordering in concentrated ferrofluids. *Phys. Rev. E*, 68:031203, Sep 2003.
- [194] Nigel B. Wilding. Computer simulation of fluid phase transitions. *American Journal of Physics*, 69(11):1147–1155, 2001.
- [195] F. Wittbracht, B. Eickenberg, A. Weddemann, and A. Hütten. Rotating magnetic field assisted formation of highly ordered two-dimensional magnetic bead arrays. In *ICQNM 2011, The Fifth International Conference on Quantum, Nano and Micro Technologies*, page 99, 2011.
- [196] Qiliang Yan and Juan J. de Pablo. Fast calculation of the density of states of a fluid by monte carlo simulations. *Phys. Rev. Lett.*, 90:035701, Jan 2003.
- [197] Qiliang Yan, Roland Faller, and Juan J. de Pablo. Density-of-states monte carlo method for simulation of fluids. *The Journal of Chemical Physics*, 116(20):8745–8749, 2002.
- [198] Anand Yethiraj, Alan Wouterse, Benito Groh, and Alfons van Blaaderen. Nature of an electric-field-induced colloidal martensitic transition. *Phys. Rev. Lett.*, 92:058301, Feb 2004.
- [199] Yokoyama Takashi, Yokoyama Shiyoshi, Kamikado Toshiya, Okuno Yoshishige, and Mashiko Shinro. Selective assembly on a surface of supramolecular aggregates with controlled size and shape. *Nature*, 413(6856):619–621, oct 2001. 10.1038/35098059.
- [200] Emanuela Zaccarelli. Colloidal gels: equilibrium and non-equilibrium routes. *Journal of Physics: Condensed Matter*, 19(32):323101, 2007.
- [201] Zhang and Sharon C. Glotzer. Self-assembly of patchy particles. *Nano Letters*, 4(8):1407–1413, 2004.
- [202] Cheng Zhang and Jianpeng Ma. Simulation via direct computation of partition functions. *Phys. Rev. E*, 76:036708, Sep 2007.